Carbon Photodetectors: The Versatility of Carbon Allotropes

Moses Richter, Thomas Heumüller, Gebhard J. Matt, Wolfgang Heiss, and Christoph J. Brabec**

We dedicate this review to Prof. Dr. Nazario Martín on the occasion of his 60th birthday.

Carbon-based organic electronics are a technology, with the potential of complementing and substituting opto-electronic devices based on inorganic semiconductors and metals. In the group of organic semiconductors, carbon allotropes come with outstanding opto-electric properties and are remarkable candidates for novel applications like printed electronics via solution-processing on mechanically flexible, robust and light weight substrates, while reducing the environmental impact. Carbon allotropes like fullerenes, graphene quantum dots (GQD), carbon nanotubes (CNT), graphene and also diamond are especially interesting for photodetectors due to their tunable bandgap, high absorption coefficients and high charge carrier mobilites. These unique opto-electric properties of the allotropes, which strongly depend on their molecular dimensionality (0D, 1D, 2D and 3D), allow each allotrope to be used in a preferential range. Hence, relying on the intrinsic properties of carbon allotropes or by hybridization, carbon-based photodetectors are built for a spectral bandwidth, reaching from gamma-rays to THz radiation. This review highlights the recent advances in photodetectors based on fullerenes, GQDs, CNTs, graphene and diamond, with the focus on room temperature-operated devices. The versatility of multi-dimensional carbon allotropes is outstanding, and promising results outline the maturing of all carbon-based photodetection across the technologically relevant wavelengths.

1. Introduction

The conversion of light, which is electromagnetic radiation that carries energy and can be defined by a wavelength or frequency, became essential to the technological age. In modern societies, it is impossible not to encounter at least one photodetecting device or component on a daily basis. Currently, the photovoltaic technology is making a big impact by reallocating the electric power, which mankind consumes in the 21st century, to a more sustainable and environmental friendly technology. For solar cells, the power conversion efficiency of sun light is of importance and benefits from a broad optical absorption and a high photocurrent and photovoltage.[1] On the other hand, photodetectors are employed with the primary goal of delivering a precise electrical signal, photocurrent or photovoltage, most representative for the detected illumination event. Thereby, they serve as interface between optical information and electronic circuitries. Hence, photodetectors find nowadays application in consumer electronics (digital imaging, contactless thermometers, self-driving cars) medical care, environmental monitoring, industrial automation, digital communication, quality control, security and astronomy.

For an optimal performance, the spectral sensitivity and response speed of photodetectors are chosen to meet the demands and can be tailored over several orders of magnitude by adopting the material and device architecture. Two detector types can be distinguished. i) Photonic detectors (e.g., photoconductors, photodiodes, phototransistors) rely on the direct conversion of absorbed photons to charge carriers, whereas ii) thermal detectors rather exploit electrical changes upon a temperature change in the absorber material. Ultimately, the light matter interaction inside the detector must lead to the generation of an electric signal and depends on the photon energy E_{ph} and wavelength λ, respectively. For high energy photons, gamma rays ($E_{ph} > 100$ keV, $\lambda < 12$ pm) and X-rays ($E_{ph} > 1$ keV, $\lambda < 1$ nm), effects like the photoelectric effect, Compton scattering or pair production determine the electric response and increase with the atomic weight of the photoactive material utilized in the detector. Commonly used for direct X-ray detectors are photoconductors like amorphous selenium (a-Se) or cadmium telluride (CdTe).[2,3] For photodetection of longer wavelength and smaller photon energies, semiconductors are suitable, as the photoresponse is rather based on electron-hole pair generation by optical excitation across the bandgap. Preferred detector materials for ultraviolet (UV) light, which is defined

M. Richter, Dr. T. Heumüller, Dr. G. J. Matt, Prof. Dr. C. J. Brabec
Friedrich-Alexander-University Erlangen-Nürnberg (i-MEET)
Martensstrasse 7, 91058 Erlangen, Germany
E-mail: moses.richter@fau.de; christoph.brabec@fau.de
Prof. Dr. W. Heiss
Energy Campus Nürnberg (EnCN)
Fürther Strasse 250, 90429 Nürnberg, Germany
Prof. Dr. Christoph J. Brabec
Bavarian Center for Applied Energy Research (ZAE Bayern)
Haberstrasse 2a, Erlangen 91058, Germany

DOI: 10.1002/aenm.201601574

 © 2016 WILEY-VCH Verlag GmbH & Co. KGaA, Weinheim

from extreme UV to the UV-A band (124 eV ≥ E_{ph} ≥ 3.1 eV, 10 nm ≤ λ ≤ 400 nm), are wide-bandgap semiconductors such as GaN, AlN or ZnO.[4] Furthermore, nano-scale transition metal oxides and alloys are gaining significant attention for their potential use in novel printable and flexible ultra-compact and self-powered photoelectrochemical UV photodetectors.[5,6] With increasing wavelength across the visible range (VIS) of the spectrum from 380 nm to 780 nm the required bandgap has to decrease in order to shift the absorption onset to 1.6 eV (≈780 nm). Here, silicon (Si) is the common semiconductor found in respective photodetectors. Entering the near infrared (NIR) spectrum (1.24 eV ≥ E_{ph} ≥ 0.41 eV, 1 µm ≤ λ ≤ 3 µm), photodetection in Si is limited by its absorption edge at 1.1 µm, hence material combinations like Si/Ge heterojunctions[7] or III–V (e.g., indium gallium arsenide, InGaAs) semiconductor alloys, with even smaller bandgaps, have to be used. For instance, InGaAs photodetectors can be used up to a wavelength of 2.6 µm at room temperature, and the integration of Ge photodetectors on Si helps to enable on-chip optical communication around 1.5 µm.[7,8]

For the detection of mid infrared (MIR) light (0.41 eV ≥ E_{ph} ≥ 25 meV, 3 µm < λ ≤ 50 µm), one material that stands out is the ternary II–VI alloy mercury cadmium telluride (HgCdTe). Depending on the composition, the bandgap can be tailored for light absorption from 1 µm up to 12 µm.[8] However, it must be noted here, that the photon energy approaches the thermal energy at room temperature of k_BT = 25 meV, where k_B is the Boltzmann constant and T the temperature in Kelvin. Hence, at room temperature for MIR detection >3 µm, the detectors are often cooled below 300 K to improve the detectivity and reduce the thermal noise.

With the transition from the MIR spectrum to the far infrared (FIR) spectrum (25 meV ≥ E_{ph} ≥ 1.2 meV, 50 µm < λ ≤ 1 mm) the detection mechanism changes more and more from a photonic to thermal nature. Additionally, the wavelength selective detection is not as critical anymore to applications, so that thermistor-based bolometers (e.g., with vanadium oxide) and thermopiles are used for photodetection. In between the MIR and FIR spectrum the THz technology has manifested the nomenclature of the THz spectrum which is widely accepted to be within the wavelengths of 30 µm to 3 mm, corresponding to a frequency range of 0.1–10 THz. Due to the partial overlap with the MIR and FIR spectrum, the definitions are often used interchangeably.

One common analogy shared by all commercially available photodetectors, covering the electromagnetic spectrum as introduced above, is that the utilized photoactive materials are inorganic. The manufacturing process of all these semiconductors and complex alloy systems require at some point a high temperature (several hundred°C), high energy consuming step.[9,10] The growth processes are facilitated in elaborate processes like metalorganic chemical vapor deposition (MOCVD) and various other epitaxial growth methods, which are complex, sensitive to process fluctuations (e.g., material purity, atmosphere) and have in general a high technological demand.[11] Owing to the processing methods, the maximal size of detector arrays and imagers is limited by the substrate size, which in many cases are Si wafer with currently 12 inch (300 mm) in diameter. Moreover, the processes and the photoactive material itself often contain hazardous elements like Pb, Hg, Cd,

Moses Richter obtained his BSc in Nanotechnology from the University of Applied Sciences South Westphalia Germany and his MSc (honor) degree in Material Science from the Friedrich-Alexander-University Erlangen-Nürnberg. During his Master thesis he worked on printed, transparent composite electrodes for organic electronics and on organic photodiodes. As a member of the research training group GRK 1896, supported by the German Research Foundation DFG, he is currently pursuing his PhD study under the supervision of Prof. Christoph J. Brabec. His current research interests are on charge transport in hybrid photodetectors and nanoparticular systems.

Wolfgang Heiss received his MSc degree at the University of Innsbruck and finished his PhD at the Vienna University of Technology, both in Austria. He was a staff member at the Johannes Kepler University of Linz before he joint the FAU Erlangen-Nürnberg/Germany in 2014. His research areas cover solution processed semiconductor materials, preferentially in the form of inorganic and organic colloidal nanocrystals. Some highlight results include various solution processed photo-detecting devices operating in spectral regions between the mid-infrared and soft X-rays.

Christoph J. Brabec is holding the chair "Materials for Electronics and Energy Technology (i-MEET)" at the materials science department of the FAU Erlangen-Nürnberg. Further, he is the scientific director of the Erlangen division of the Bavarian Research Institute for Renewable Energy (ZAE Bayern, Erlangen), board member of the ZAE Bavaria, and board member of the Energy Campus Nürnberg. He received his PhD (1995) in physical chemistry from Linz University, joined the group of Prof. Alan Heeger at UCSB for a sabbatical, and continued to work on all aspects of organic semiconductor spectroscopy as assistant professor at Linz University with Prof. Serdar Sariciftci. He joined the Siemens research labs as a project leader for organic semiconductor devices in 2001, finished his habilitation in physical chemistry in 2003 at Linz university and joined Konarka in 2004, where he was holding the position of CTO before joining FAU Erlangen-Nürnberg. His research interests are organic photovoltaics, all aspects of solution processed semiconductors and technologies for renewable energy scenarios.

© 2016 WILEY-VCH Verlag GmbH & Co. KGaA, Weinheim

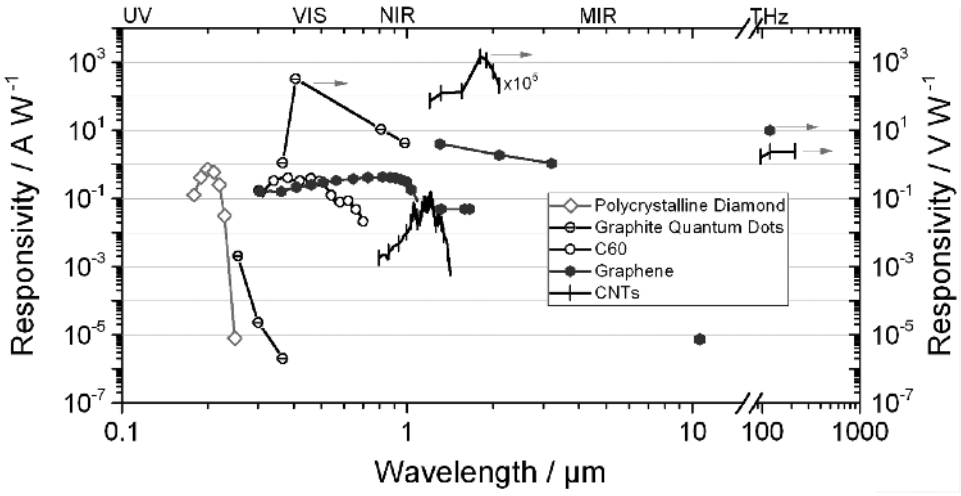

Figure 1. Reported, spectrally resolved responsivites for carbon allotrope based photodetectors are summarized. Data is extracted from literature and is introduced within the scope of this review.[20,21,36–46] The broad coverage of the electromagnetic spectrum by photoactive carbon is remarkable.

and As. Nevertheless, the advantageous properties prevail, and inorganic semiconductors for photodetectors have been developed for many years with great advances on miniaturization, increased response speed and responsivity, a large dynamic range, and low noise operation. They are often motivated by compatibility with industrial complementary metal oxide semiconductor (CMOS) standards.[12–14]

Anyhow, since the 1960s, the emerging field of organic electronics has developed tremendously in pursuit of the inorganic semiconductor technology and nowadays offers alternatives to many opto-electric applications, so far dominated by inorganic semiconductors or metals, like transparent electrodes,[15] thin film transistors,[16] solar cells[17,18] and also photodetectors.[19] The development is driven by several advantages over inorganic counterparts and gains more momentum with increasing scientific and industrial advances. The processing methods for organic components are in general milder than for inorganic ones, and reach from thermal evaporation to high throughput roll-to-roll printing on flexible substrates. The strong light interaction of organic semiconductors, especially in the NIR, attributed to absorption coefficients of $>10^5$ cm^{-1}, requires only film thicknesses of some hundred nanometers for sufficient light absorption. These make organic, opto-electric materials very attractive for large area device fabrication, with very little material consumption. Eventually, inexpensive, printed electronics are anticipated for applications where a reduced weight and flexibility are inevitable, and already show the potential of complementing or even replacing some of the existing inorganic semiconductor technologies.[20–25]

Besides the variety of available semiconducting, conjugated polymers and small molecules,[26] over the last two decades three new carbon allotropes where discovered, namely fullerenes, carbon nanotubes (CNTs) and graphene. Fullerenes, the smallest allotrope, can be considered a quasi zero-dimensional (0D) spherical molecule due to its diameter of less than one nanometer.[27] CNTs on the other hand have a tremendous aspect ratios of $>10^3$ and therefore can be viewed as one-dimensional (1D) structures. By covering macroscopic areas, despite being atomically thin, graphene represents a two-dimensional (2D) structure of carbon. Stacking several graphene layers results in graphite, as one of the three-dimensional (3D) carbon allotropes. The second one, diamond, consists of tetrahedrally bond sp^3-hybridized carbon atoms. Despite sharing one and the same element, the allotropes' structures and dimensionalities determine quite diverse opto-electric and thermo-electric properties. Great advances in research demonstrate how these allotropes can be in fact used in their pristine or chemically modified configuration to harvest a photocurrent,[18,28] generate a thermal- or photovoltage,[21,29] emit light,[30,31] respond to a field effect[32,33] and efficiently conduct high currents.[15,34,35] All of these properties give rise to future, environmental friendly, highly functional all carbon electronics.

Highlighting the unique, structure related, opto- and thermo-electric properties, we summarize various works on photodetectors within this review paper, incorporating 0D, 1D, 2D, and 3D carbon allotropes. We emphasize the latest achievements from literature, in which the opto-electric properties of the carbon component are responsible for the core functionality of the photodetector device. That means, the light absorption as well as the electric signal generation is enabled by the carbon allotrope within the photoactive layer. As long as this prerequisite holds and they lead to performance enhancing effects we briefly introduce organic/organic and organic/inorganic hybrid structures as well. It is evident from the spectral responsivity of various carbon-based photodetectors, summarized in **Figure 1**, that carbon allotropes are more than suitable to facilitate room-temperature photodetection across an amazingly broad electromagnetic spectrum, reaching from gamma rays to THz radiation.

2. Photodetector Figures of Merit

In this review, a broad variety of photodetectors with different working principles will be introduced. Therefore, this section provides a brief explanation of the key parameters, which define the photodetector performance in the respective cases.

The most fundamental performance metric is the responsivity R of a detector. It relates the photocurrent I_{ph} or

 © 2016 WILEY-VCH Verlag GmbH & Co. KGaA, Weinheim

photovoltage V_{ph}, generated upon irradiation, with respect to the incident illumination power P_0 according to

$$R_I = \frac{I_{ph}}{P_0} \text{ or } R_V = \frac{V_{ph}}{P_0} \quad (1)$$

with units of A W^{-1} and V W^{-1}.

Whenever the photoresponse of the detector is about the photogeneration of free charge carriers which will be collected as photocurrent, the internal (*IQE*) and external quantum efficiency (*EQE*) can be additionally used to quantify it. The *IQE* is defined by the number of collected charge carriers per absorbed photons at a specific wavelength λ and does not exceed unity. The *EQE* on the other hand is defined by the number of collected charge carriers per total incident photons. Hence the *EQE* is usually found to be smaller than the *IQE* due to transmission and reflection losses and/or due to a small absorption cross section of the photoactive device. Because the *EQE* is a function of the wavelength it is also related to the photon energy E_{ph} and the illumination power, respectively. Therefore, it can be converted to R_I according to

$$R_I = EQE\ \frac{\lambda q}{hc} = EQE\ \frac{q}{E_{ph}} = \frac{I_{ph}}{P_0} \quad (2)$$

where q is the elementary charge, h Planck's constant and c the speed of light.[47] However, exceeding unity *EQE* is possible for photoconductors. That means, per photo-generated electron-hole pair several more carriers are detected, which is feasible if one carrier type is being trapped after generation, allowing the other carrier type to transit the photodetector for several times before recombination.[48–50] The mechanism is described as photoconductive gain and typically seen in systems with unbalanced electron-hole mobilities. Photoconductive gain manifests as a factor G on the photocurrent and is defined as the ratio of the charge carrier life time τ and their transit time τ_{tr}:

$$G = \frac{\tau}{\tau_{tr}} \quad (3)$$

Since the photodetector's temporal response is proportional to the transit time, it is always a trade-off between a higher gain and a faster operation speed. The bandwidth limitation f_{tr} due to the transit time follows

$$f_{tr} = \frac{1}{2\pi}\ \frac{\mu V}{d^2} = \frac{1}{2\pi}\ \frac{1}{\tau_{tr}} \quad (4)$$

and shows that by either decreasing the device thickness d or increasing the carrier mobility μ it is possible to optimize the detector bandwidth.[47] Eventually a transit time and *RC* time component limit the overall photodetector bandwidth, which is expressed in form of the cut-off frequency determined per definition to be the upper bandwidth limit, where the signal amplitude dropped by 3 dB (≈70%) with respect to its maximum. Alternatively, the detector response to a light pulse can be recorded. The time it takes the signal to rise (fall) from 10% to 90% (90% to 10%) is determined as rise time t_r (fall time t_f). A high response speed is desired, e.g., for communication purposes within the GHz bandwidth.[51]

Next to the quantum efficiency and speed it is equally important for photodetectors to detect low light intensities and to maximize the signal-to-noise ratio (*SNR*). The noise equivalent power (*NEP*) defines the smallest detectable signal which gives a *SNR* = 1 at one Hertz output bandwidth B. It therefore defines the smallest detectable signal according to

$$NEP = \frac{\sqrt{\langle I_n^2 \rangle / B}}{R_{I,V}} \quad (5)$$

where $\sqrt{\langle I_n^2 \rangle}$ is the root-mean-suqare of the noise current I_n. Unit-wise, the *NEP* is expressed in W $Hz^{-1/2}$. The noise current of a detector is composed of frequency independent noise sources such as white thermal noise and frequency dependent sources like the shot noise and the *1/f* noise. Shot-noise I_{sh} occurs due to fluctuations in the current density by the nature of the charge transport and is proportional to the DC current I_{DC}. It is given by:

$$\langle I_{sh}^2 \rangle = 2qBI_{DC} \quad (6)$$

The low frequency *1/f* noise often has the major contribution. Nevertheless, it is often easier to reduce the electronic noise by annihilating the high dark current, which flows in absence of illumination, by e.g., operating the photodetector in the photovoltaic (PV) mode. The disadvantage is that in the PV mode the gain is per definition smaller than unity and detector-technologies with good photovoltaic properties often feature a high, speed limiting capacitance.

Normalizing the *NEP* to the device area yields the so-called specific detectivity *D** (hereafter referred to as detectivity if not stated otherwise) in the units of cm $Hz^{1/2}$ W^{-1} or Jones respectively. The detectivity of a photodetector describes the *SNR* for a photoactive area A of 1 cm^2 under an optical illumination power of 1 W at a bandwidth of 1 Hz. Thus it can be used to quantitatively compare different devices. Nevertheless, it should be noted here, that the noise current is occasionally estimated by the shot noise and thermal noise only, without relying on the actual frequency range of the measurements. This generally leads to an over estimation of the detectivity and complicates direct device comparison nonetheless.[52]

*D** is defined according to

$$D^* = \frac{\sqrt{A}}{NEP} \quad (7)$$

Slightly different key parameters are defined for thermoelectric detectors. In case of contactless temperature sensing the change of electrical resistance within an absorber material, hence referred to as thermistor, is detected upon a temperature change, recognized as the bolometric effect. To evaluate the performance of a thermistor the temperature coefficient of resistance (*TCR*) is defined as

$$TCR = \frac{1}{Z}\ \frac{dZ}{dT} \quad (8)$$

where Z is the electrical resistance and dZ/dT the change in resistance with temperature. The *TCR* is given in units of % K^{-1}. Similar to the *NEP*, for thermal sensors the noise

© 2016 WILEY-VCH Verlag GmbH & Co. KGaA, Weinheim

Table 1. A list of photonic detectors based on various carbon allotropes as active material.

Active Material	Detector Type	Wavelength [nm]	Responsivity		*EQE* [%]	Gain	Specific Detectivity [cm $Hz^{1/2}$ W^{-1}]	t_{rise} [ms]	t_{fall} [ms]	Year/Ref.
			[A/W]	[V/W]						
C60	photodiode	340–470	0.37[a)]		–		3.2×10^{11}[a)] @ 35 Hz	0.031	0.037	2013[36]
C60	phototransistor	470	1047		–	2762	–	–	–	2014[54]
C60-ribbon	photoconductor	350–360	90.4		–	316	–	500	500	2013[55]
		450–750	75.3		–	161	–			
GQDs	photodiode	254	0.0021		<5.9	–	9.59×10^{11} @ 1.5 kHz	64	43	2015[38]
GQDs/Graphene	phototransistor	325	4×10^7		~26	3.75×10^9	–	5	13	2013[49]
GQDs	photoconductor	405		325	–	–	–			2014[37]
		980		4.79	–	–	–	50000	–	
GQDs/Graphene	photoconductor	400–800	0.2–0.43		71[a)]	–	9.5×10^{11}[a)] @ 10 kHz	$\approx 10^{-6}$	0.080	2014[56]
SWCNTs/Graphene	phototransistor	650	120		≤34	~10^5	–	~0.1	~0.1	2015[57]
SWCNTs/C60	phototransistor	1000–1400	220		–	$3–4 \times 10^4$	1.2×10^9 @ 1 kHz	2-4	2-4	2015[58]
MWCNTs/Graphene	photoconductor	1000–1300		3065[b)]	–	–	1.5×10^7 @100 Hz	1.5	1.5	2013[59]
SWCNTs	photodiode	1800		1.5×10^8	–	–	1.25×10^{11} @ 1 Hz	20	20	2016[39]
Graphene pn-junction	photodiode	600–1000	0.55[a)]		85[a)]	–	9.7×10^{11}[a)]	$\approx 11.7 \times 10^{-3}$[b)]		2014[43]
Graphene	phototransistor	1550	0.006		–	–	–	$\approx 2 \times 10^{-8}$[b)]		2010[20]
Graphene/SiO_2/Graphene	phototransistor	1300	4		–	–	–			2014[44]
		3200	1.1		–	–	–			
Polycrystalline diamond	photoconductor	157		≈0.077	–	–	–	12.3×10^{-6}[b)]		2001 [46]
Polycrystalline diamond	photoconductor	200	–	–	–	1×10^6	–	1000[b)]	8800[b)]	1998[60]
Single crystal diamond	photoconductor	220	0.2		–	–	–	0.02	1	2015[61]
		340	0.048		–	–	–	–	–	

[a)]This value is an averaged of the spectral data provided within the original publication; [b)]Value was not specifically named by the authors, however could be extracted from their data. Not available data is marked by a dash sign -.

equivalent temperature difference (*NETD*) is used to describe the smallest detectable temperature difference. The *NETD* is also susceptible to frequency dependent and independent electronic and thermal noise.

The second type of thermal detectors, exploiting the photothermoelectric (*PTE*) effect as detection mechanism, and rquires another figure of merit, *ZT*.[53] The *ZT* factor, is determined according to

$$ZT = \frac{S^2 \sigma T}{\kappa} \tag{9}$$

where S is the Seebeck coefficient, σ the electric conductivity and κ the thermal conductivity of the active material. Minimizing *ZT* is important as it correlates inversely to the *NEP* of thermo-electric detectors according to

$$NEP = \frac{2\sqrt{k_B T^2 WL}\sqrt{H}}{\sqrt{ZT}} \tag{10}$$

with W being the active layer width, L the thermal length over which the temperature decays within the active film and H the heat transfer coefficient to the substrate. Equation (10) applies if the device is limited by thermal Johnson noise only.

A summary of the so far highest reported device performances, with regard to the spectral sensitivity, can be found in **Table 1** for photonic and in **Table 2** for thermoelectric carbon allotrope-based detectors. The particular devices and underlying working principles will be discussed in more detail.

3. Zero-Dimensional Carbon Allotropes for Photodetection

Particles or molecules, that are made up of only a few atoms, have a spatial extent of not more than a nanometer. Therefore, they are considered as materials with zero dimensionality. The most famous carbon allotrope of the 0D class is the fullerene. It is a sphere like cage of pentagonal and hexagonal rings of sp^2-hybridized carbon atoms, resembling the pattern of a football. The fullerenes or buckyballs were first discovered in 1985 by R. Curl, H. Kroto and R. Smalley, and rewarded by the Nobel prize in chemistry in 1996.[65] The molecules have been heavily researched ever since for a variety of properties such as high electron affinity, high charge transport and high degree of surface sensitivity.[66] Besides in photodetecting devices, which will be introduced in more detail below, they additionally found application for these molecules in electronic devices

© 2016 WILEY-VCH Verlag GmbH & Co. KGaA, Weinheim

Table 2. A list of thermoelectric detectors based on various carbon allotropes as active material.

Active Material	Detector Type	Wavelength [μm]	Responsivity [V/W]	*TCR* @ 300K [%/K]	*NETD* [K]	t_{rise} [ms]	Year/Ref.
SWCNTs	bolometer	0.3–3	48	10	–	83	2013[62]
MWCNTs + antennae	bolometer	10.6	800	0.3	–	25	2013[63]
MWCNTs	bolometer	6–14	138	–2.1	1.1 NEP [W Hz$^{-1/2}$]	–	2013[64]
SWCNTs	thermocouple	0.66–3.3	1		–	600	2013[40]
SWCNTs	thermocouple	96.5	2.5		20×10^9	–	2014[21]
		119	2.4		–	–	
		215	1.7		–	–	
Graphene	thermocouple	119	10		16×10^{12}	110×10^{-9}	2014[42]

like photovoltaics[67] and organic field-effect transistors,[33,68,69] which demonstrate the versatility of the material class. However, their most prominent application today is as an electron accepting semiconductor in heterojunction organic solar cells.

Carbon nanoparticles are a rather young discovery of the year 2004 and can be considered, next to fullerenes, another 0D form of carbon.[70] Although the morphology of the particles can vary quite a lot, they were assigned to the class of carbon allotropes, since their main constituent is fragmented graphene. Due to the variety in morphologies, there are different terminologies used interchangeably in literature. Within the scope of this review, we will address carbon nanoparticles independent of their structure and chemical modifications as graphene quantum dots (GQD). The individual graphene layers can be nicely visualized under TEM, as exemplarily depicted in **Figure 2**.

Over the last decade carbon nanoparticles gained a lot attention by researchers across different communities, because of their various exciting properties such as remarkable photoluminescence, low photobleaching, chemical stability, low toxicity, bio compatibility, dispersability in water, and last but not least carbon as abundant low cost core element. Hence, GQDs are readily used in a huge variety of opto-electronic applications like photodetectors, solar cells, organic light-emitting diodes but also lithium-ion batteries, supercapacitors, catalysts, chemical sensor (ion detection) and fluorescent biomarkers.[72] Recent advances in material design, device architecture and processing methods have demonstrated both 0D materials as suitable alternative, perhaps even replacements, for some inorganic photodetector technologies in the UV-NIR spectrum.

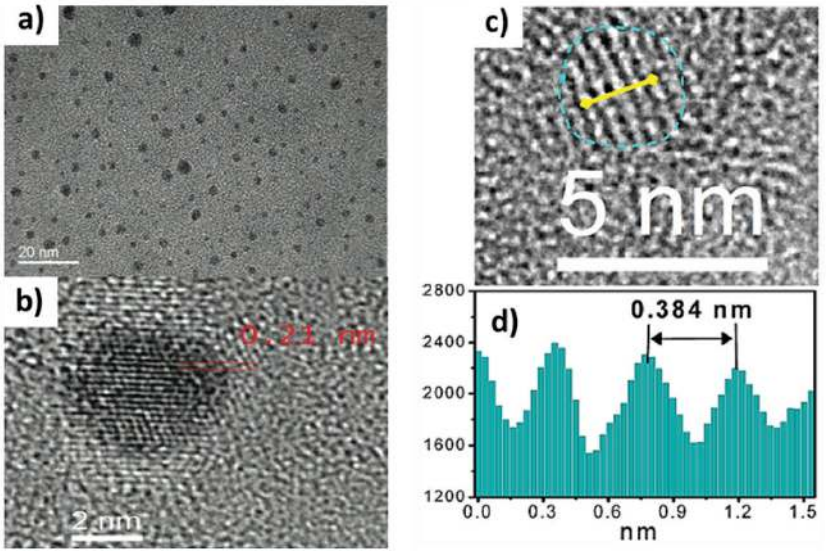

Figure 2. a) and b) TEM and HRTEM images of PANI-GQDs, respectively. b) The atomic planes exhibit a spacing of 0.21 nm, corresponding to a lattice spacing typical for graphite. Reproduced with permission.[71] Copyright 2015, The Royal Society of Chemistry. c) and d) HRTEM of a single nitrogen-doped GQD with a lattice plane spacing of 0.38 nm. The functional groups induced increased lattice constant. Reproduced with permission.[37] Copyright 2014, American Chemical Society.

3.1. Fullerene-Based Photodetectors

Fullerenes, and some derivatives thereof, show a dominant absorption below 400 nm. Hence, using them as the sole photoactive material in a UV detector system is a straight forward approach. The absorption spectra of pristine C_{60} molecule and derivatives, such as e.g., $PC_{61}BM$, ICBA or $PC_{71}BM$, are fairly similar. Since $PC_{71}BM$ incorporates a larger C_{70} fullerene cage with greater electron delocalization, the absorption is slightly extended to visible light. Unlike pristine C_{60} molecules which need to be thermally evaporated onto the substrate of choice due to their high crystallinity, fullerene derivatives aim basically for enhanced solubility in organic solvents through covalently attached functional groups to enable solution processing/printing. Despite the more elaborate process, C_{60} molecules are preferred for manufacturing homojunction photodetectors, mostly due to their superior electrical properties in comparison with the derivatives.

© 2016 WILEY-VCH Verlag GmbH & Co. KGaA, Weinheim

Ma et al. could demonstrate the electronic potential of C_{60} in electronic devices, by creating a C_{60}-diode of rather simple architecture.[35] C_{60} was sandwiched between an ohmic Cu (cathode) and an Al (anode) contact, creating a diode sustaining an extremely high current density of 363 A cm^{-2}. The electric response speed of this diode to an AC voltage signal reached 1 MHz, which is very high for an organic diode. The bandwidth was thought to be increased further by decreasing the device capacitance and area respectively.[35] Hence, it is strongly presented that C_{60} alone fulfills the required opto-electric properties to build a potentially high performance UV detector.

Sufficient bandgap irradiation generates excitons, i.e., a bound form of an electron-hole pair, which need to be separated via an external electrical field. The intrinsic n-type nature of C_{60} implies the use of rectifying contacts in order to prevent undesired charge recombination and injection at the electrodes. With rectifying contacts, it is possible to reduce the dark or leakage current and minimize the noise equivalent power and improve the detectivity. Often aluminum is used as cathode since its work function of –4.2 eV forms a good contact to the lowest unoccupied molecular orbital (LUMO) of C60 at $LUMO_{C60}$ = –4.5 eV. On the other hand, the anode is often a combination of indium-doped tin oxide and a hole transport layer (e.g., poly(3,4-ethylenedioxythiophene) polystyrene sulfonate – PEDOT:PSS) due to the need for transparency, which at the end forms a selective contact to the highest occupied molecular orbital (HOMO) of C60 at $HOMO_{C60}$ = –6.1 eV.[35]

Within this concept, the importance of the quality of selective contact formation was demonstrated by the work of Guo and coworkers.[36] In order to reduce the dark current, a cross-linkable 4,4′-bis[(p-trichlorosilylpropylphenyl)-phenylamino]-biphenyl (c-TPD) layer was introduced as an additional hole transport layer with better electron blocking properties on top of PEDOT:PSS (**Figure 3**a). Since c-TPD introduced a large electron injection barrier at the anode side, as illustrated in the energy diagram in Figure 3b, the dark current was reduced to the order of magnitude of the shot noise limit, enabling a NEP of only 0.55 pW, which resulted in a remarkable linear dynamic range of 90 dB of the detector. Nevertheless, a drawback of the more effective hole blocking layer was the reduction in EQE down to 40%, averaged over the spectral range from 340 nm to 470 nm. However, within the same spectral range, the mean specific detectivity of 2.5×10^{11} Jones was reached, as plotted in Figure 3c. The on and off current transient had a rise (fall) time of 31 µs (37 µs) and was actually limited by the measurement equipment. Hence, the operation bandwidth of the detector was determined approximately 20 kHz but was expected to be even faster.[36]

Similar interface modifications presented in C_{60} photodetectors have been further investigated in phototransistor devices. R. Ahmed et al. presented that the evaporation of parylene on C_{60} (top-gated) introduces free radicals at the interface.[54] These radicals acted as hole-traps, whereby the light-induced threshold voltage shift became strongly influenced by the wavelength and the incident light intensity. Operated as photodetector, the device showed a photoresponse at 470 nm of 1000, a remarkable responsivity of 1047 A W^{-1} and a photoconductive gain of more than 2700. Starting from the absorption edge of C_{60} at 550 nm, the spectral response of the device increased further for smaller wavelengths in agreement with the absorption coefficient.[54]

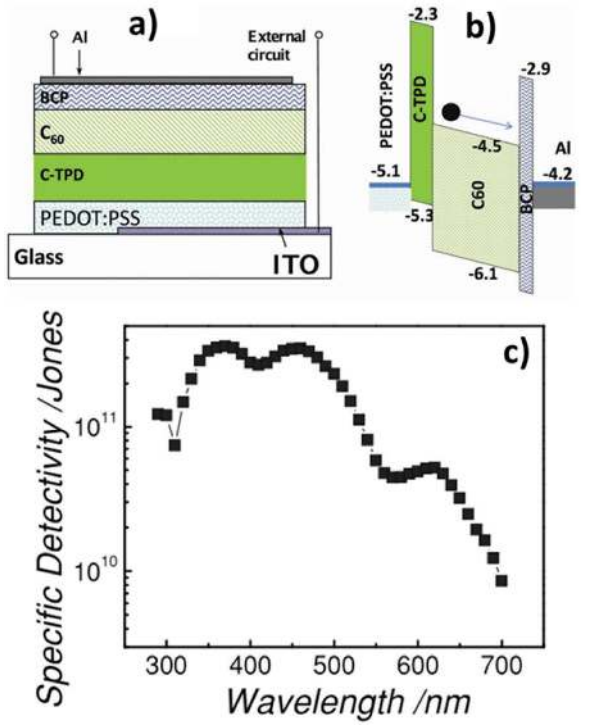

Figure 3. a) Layer stack of a C_{60} photodiode. The PEDOT:PSS hole transport layer was supported by an additional electron blocking layer of c-TPD, which dramatically reduced the dark current of the diode. The electron injection barrier through c-TPD becomes clear in the energy diagram b). c) Shows the spectral detectivity of the C_{60} photodiode. Reproduced with permission.[6] Copyright 2013, Wiley.

Another phototransistor device was reported by Luo et al., where a very thin layer of polyvinyl alcohol (PVA) and octadecyltrichlorosilane (OTS) was used to modify the interface between C_{60} and the SiO_2 dielectric.[73] This interfacial modification was claimed to reduce interface trap states, which led to an increased responsivity of 234 A W^{-1} under a weak (2 nW) 405 nm light pulse for a gate voltage of 50 V and a source-drain field of 10^4 V cm^{-1}. Hence, the detectivity reached 8.1×10^{12} Jones, and the *EQE* was exceeding 70000%. The response time was reported as 210 µs (140 µs) rise (fall) time, which is faster than the response time observed for the detectors based on inorganic compound semiconductors in belt or ribbon configuration.[73]

As an alternative to the thermal evaporation of C_{60} molecules, L. Wei et al. have developed a way to control the self-assembly of C_{60} molecules from solution into π–π stacked 1D C_{60} chains which further aggregate into single-crystalline ultra-thin 2D microribbons.[55] For this process, C_{60} was dissolved in CS_2 under the presence of a poor solvent like iso-propanol (IPA). This allowed the stabilization of the crystallizing microribbon structure by the CS_2. Subsequently, the obtained solvated monoclinic microribbons of C_{60}•$3CS_2$ were converted into pure, densely packed fcc C_{60} microribbons via sublimation of CS_2 at 120 °C as illustrated in **Figure 4**a. A TEM image of some C_{60} microribbons in the fcc form is depicted in Figure 4b.

© 2016 WILEY-VCH Verlag GmbH & Co. KGaA, Weinheim

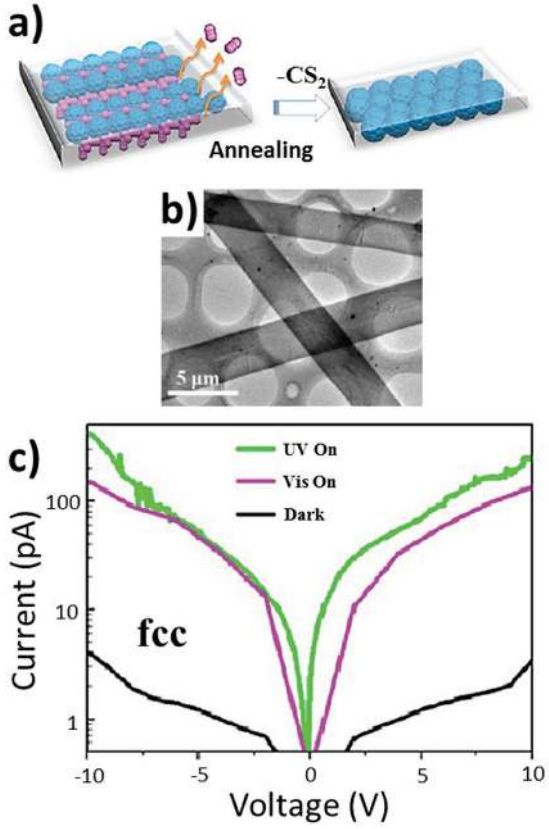

Figure 4. a) After precipitating C60 molecules from a CS2 solution, monoclinic solvated microribbons are obtained. Upon heating, microribbons transform into fcc structure due to CS2 sublimation. b) TEM image of C60 microribbons on a lacey carbon grid. c) Contacted by two Au electrodes, rather symmetric IV curves indicate an on/off ratio of more than one order of magnitude for UV and VIS illumination. Reproduced with permission.[55] Copyright 2013, American Chemical Society.

Both microribbon structures exhibit a high photoconductivity, demonstrated by a simple device of one ribbon contacted by symmetric gold electrodes. The performance was evaluated under UV (350–360 nm) and VIS (450–750 nm). For the monoclinic (fcc) microribbon the on/off ratio under UV illumination was 250 (69) and thereby slightly higher than the on/off ratio under VIS light with 200 (40), as seen by the corresponding IV curve, plotted in Figure 4c. Mainly due to an elevated dark current caused by the heat-induced defects, the on/off ratio decreased with the fcc transformation. Nonetheless, since the fcc transformation increased the light current as well, the responsivity improved from 25 to 90 A W^{-1} under broadband UV illumination and from 24 to 75 A W^{-1} in broadband VIS illumination.[55]

As mentioned above, C_{60} can be made soluble in organic solvents by functionalization. The increased solubility additionally enabled the direct mixture of fullerene derivatives like PCBM with semiconducting absorber polymers and small molecules: a concept which was first introduced in 1995 and named bulk-heterojunction.[74] The intermixing of both components tremendously increases the contact surface between the electron accepting PCBM and the hole conducting (electron donating) organic semiconductor phase. Devices comprising such a bulk-heterojunction typically establish a build-in electrical field, due to the high electron affinity of fullerenes. Thus, the dissociation of photogenerated excitons is facilitated much more efficiently reaching internal quantum efficiencies of about 100% without external bias.[75] Therefore, the bulk-heterojunction active layer blends led organic solar cells to become a competing technology with recently certified record efficiencies of 11.5%.[76] It should be noted that in the bulk-heterojunction concept the main light absorption is determined by the donor material rather than the fullerene. A more detailed comparison of absorber polymers and small molecules can be found summarized in detail elsewhere.[77,78]

3.2. Fullerene Hybrid Photodetectors

As the fullerene component in a bulk-heterojunction layer plays a crucial role on the functionality, and the operating voltage itself can determine the difference between a solar cell and a detector, the application of fullerene-based bulk-heterojunction blends has additionally established the field of organic photodiodes. The spectral response of a bulk-heterojunction blend is usually tailored by the bandgap of the selected donor material. While a broad absorption is appreciated for solar cells (i.e., small bandgap between 1.4 eV and 3 eV), a narrow absorption can be desired for organic photodiodes, especially for color detection and imaging.[52,79,80] With respect to the spectral sensitivity, we want to introduce a few successful hybrid devices which expand the detection limits beyond VIS-NIR region and still take the advantage of a fullerene-based organic bulk-heterojunction host matrix.

Lead sulfide (PbS) for instance is an IR absorber which is successfully synthesized as quantum dots and can be processed from solution similar to fullerene derivatives. Moreover, the absorption edge of PbS quantum dots can be tuned over particle size-induced quantum confinement effects from 850 to 3500 nm, which makes these quantum dots very promising as direct converter or sensitizer.[81–83] During the synthesis, ligands are required to facilitate the particle growth and prevent particle agglomeration.[84] These rather insulating ligands (usually long oleic acid molecules) remain inside the layer after PbS quantum dot solution is coated on a substrate, thus preventing sufficient electrical transport and good detector performance. One way to recover device performance is to exchange long ligands like oleic acid with shorter molecules, which might diminish device lifetime due to particle degradation.[84] Instead, Rauch et al. embedded PbS quantum dots, with ligands still attached, into a poly(3-hexylthiophene-2,5-diyl) (P3HT) and [6,6]-phenyl-C_{61}-butyric acid methyl ester (PCBM) bulk-heterojunction matrix.[85,86] Upon IR irradiation free electrons and holes would be generated in the PbS quantum dots and extracted over the organic matrix. Electrons were preferably transferred from the lowest unoccupied state of the PbS nanocrystal to the LUMO of PCBM at ≈4.3 eV.[48] P3HT, on the other hand, with its HOMO level at ≈5.2 eV underwent an energy alignment with the highest occupied state of the PbS nanocrystals. Hence electrons were transferred and extracted along the connected PCBM pathways, whereas holes traveled within the P3HT phase. It should be noted that the quality of

© 2016 WILEY-VCH Verlag GmbH & Co. KGaA, Weinheim

the energy alignment between PbS and the organic matrix is usually quantum dot size dependent.[87] The best performance was achieved with 4.5 nm PbS quantum dots. At 1200 nm illumination, the detectors showed an *EQE* of 16% and responsivity of 0.16 A W^{-1}. The detectivity was determined as 2.3×10^9 Jones. By increasing the quantum dot size to 5.2 nm, the device sensitivity could be even extended to 1850 nm, far beyond the silicon edge of 1100 nm.[85]

In a related approach of hybridization, Büchele et al. achieved the sensitization of a bulk-heterojunction matrix to the complete opposite side of the electromagnetic spectrum, namely X-rays.[88] They dispersed µm-sized terbium-doped gadolinium oxysulfide particles within the photoactive P3HT:PCBM. Under X-ray excitation the gadolinium oxysulfide particles would emit green light at 545 nm, close to the absorption maximum of P3HT. Once the emitted light was absorbed by the P3HT:PCBM matrix, the exciton dissociation was facilitated at the interface between both organic components and extracted by an external electrical field. The specific X-ray sensitivity of the detectors reached 5.76 µC mGy^{-1} cm^{-3}, which reads as generated charge per absorbed X-ray dose and detector volume. The value is not as high as the well-established commercial detectors made from amorphous selenium (up to 17 µC mGy^{-1} cm^{-3}),[89] however the advantages of solution processing, low-cost fabrication and the possibility of a curved and high enduring X-ray detector were maintained.

Essentially, fullerenes themselves can potentially serve as the photoactive material in UV and deep UV photodetectors, and recent works have proven that by further optimization of device architectures highly sensitive photodetectors can be achieved. Nonetheless, fullerene derivatives which can be intermixed with other organic, solution-processed semiconductors and act as electron acceptor demonstrate a broader potential of this zero- dimensional class of carbon allotropes. Eventually organic photodetectors were achieved with a sensitivity from X-rays to IR by utilizing C_{60} molecules.

3.3. Graphene Quantum Dot-Based Photodetectors

A planar infinite graphene sheet has, due to its linear energy-momentum relationship, a zero bandgap. As absorption and emission are very little, which strongly limit the range of possible optical applications, the bandgap engineering is very much desired and can in fact be achieved by introducing defects in the graphene sheet or confining it in size. Both of which are employed in the course of making graphene quantum dots. The formation of the optical band is heavily influenced by surface and edge modifications, heteroatom doping, quantum confinement, shape and conjugation of the single and stacked graphene layers.[90] In this manner, bandgap tuning and tailoring has been explored and is considered as a major advantage over plane graphene in opto-electronic applications.

All GQDs show a major absorption in the UV region. Two strong and frequently observed contributions have been assigned to the π–π^* transition of C=C bonds and the δ-π^* transition of C=O bonds at around 230 nm and 280 nm, respectively. Due to the chemical origin of these absorption bands, they are particle size independent.[37] Since the absorption spectrum of the photo-active material is decisive for the area of application, it is crucial to determine and understand the origin of all possible absorption bands in GQDs. Most knowledge on this matter originates from the elaborate investigations of the excitation wavelength-dependent photoluminescence of GQDs.[91] It should be noted that within each batch of GQDs, the structure and morphology of particles are statistically distributed. Hence, the optical properties of GQDs are often a combination of many overlapping effects. Although this hampers the investigation of the origin of the optical transitions, it can be deliberately used to extend the absorption range of the active material. For graphene flakes or graphene oxide, it is well accepted that localized sp^2 clusters inside a sp^3 carbon matrix are subjected to quantum confinement.[91] This clarifies that they hold a bandgap which gets smaller with increasing cluster size and vice versa. Eventually the size distribution of sp^2 clusters leads to PL emissions at 480–650 nm, which are weak optical transitions, contributing to the absorption spectrum as well.[92]

Equally important are the electrical properties in GQD films with respect to an efficient charge extraction from the opto-electric device. Nevertheless, conclusive property relations of electrical transport with the heterogeneous GQD morphologies need to be established in future investigations. First incorporation of GQDs in e.g., FET devices demonstrate an intrinsic p-type character of GQDs with a hole channel mobility of 0.01 cm^2 V^{-1} s^{-1}.[93]

Recently, Zhang et al. reported a high performance, GQD based, solar blind, deep UV photodetector taking advantage of the UV absorption bands.[38] The GQDs were synthesized via a hydrothermal route with an average particle size of around 4 nm, consisting of 1 to 4 graphene layers. Quantum confinement effects opened a wide band gap of 3.8 eV in the GQDs (absorption spectra is shown in **Figure 5**b), leading to an absorption edge around 320 nm for particles with an average diameter of 4.5 nm. The GQDs were coated across a gap between an Ag and Au electrode (Figure 5a), resulting in an effective device area of 0.1 cm^2. The difference in work function of the two metal electrodes created a build-in field which turned out to be the major driving force for the efficient photocurrent extraction. Maximizing the built-in field improved the detectivity of almost 3 orders of magnitude. Under air, however, the detector device was found to exhibit almost no photo-response upon UV irradiation. This effect has been reported in literature before and was attributed to the photogenerated holes under irradiation which caused the reduction and subsequent desorption of oxygen and water molecules from the GQDs surface.[94] Owing to strong electronegativity of the adsorbants, GQDs are deplete of free electrons, hence they became slightly p-conductive due to the accumulated holes.[38] Consequently photo-electrons recombine with holes, eventually canceling out the net photo-current.

In order to observe the impact of device degradation under air, the devices were measured intentionally under vacuum, resulting in a photodiode-like IV curve, as depicted in Figure 5c. Upon desorbing most of adsorbant molecules, the dark current reduced dramatically by almost 5 orders of magnitude. In the same course, the on/off photo-response improved to a factor of 2000 under 254 nm irradiation with 8 µW cm^{-2} and 5900 for high light intensity of 42 µW cm^{-2}. The photo-current response

© 2016 WILEY-VCH Verlag GmbH & Co. KGaA, Weinheim

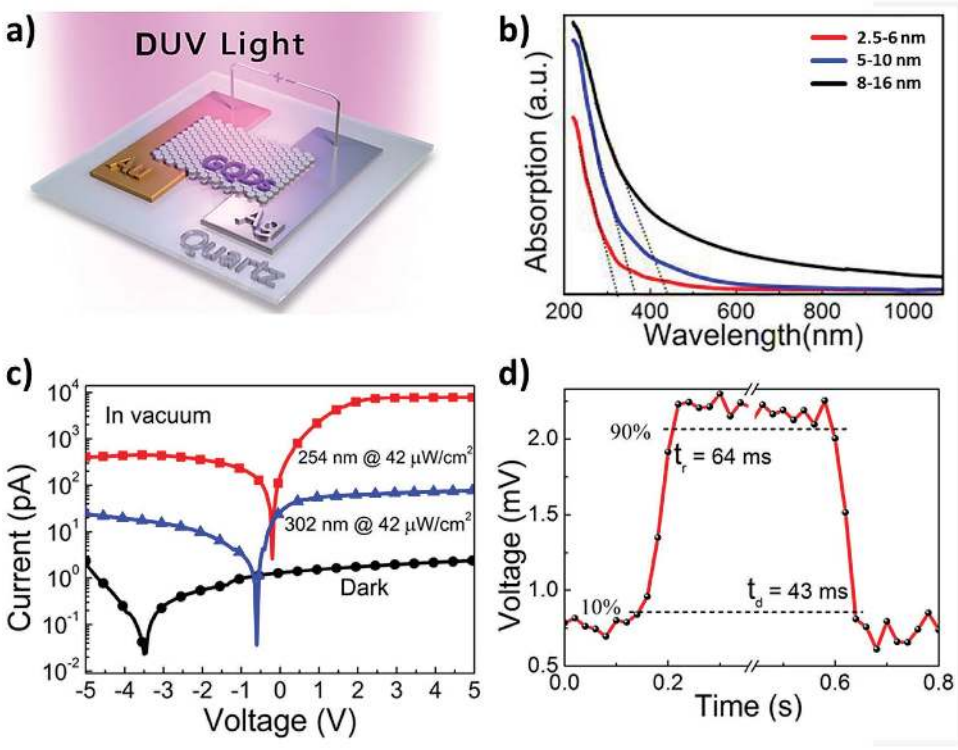

Figure 5. a) Illustration of a photodiode structure based on GQDs. b) The absorption behavior of GQDs can be tailored by the particle size. c) IV curve of the Au/GQDs/Ag diode. With decreasing wavelength, the photocurrent increased as well as the rectification behavior. d) In response to a light pulse at 254 nm, the photo voltage had a rise- (fall-) time of 64 ms (43 ms). Reproduced with permission.[38] Copyright 2015, American Chemical Society.

was linear for the mentioned intensity range. Suppressing the dark current in this photodiode-like detector, the responsivity was improved to 2.1 mA W^{-1} at +5 V and the detectivity to 9.59×10^{11} Jones. The increase in the performance was mostly attributed to the very low dark noise of 2 pA $Hz^{-1/2}$ which is comparable to silicon diodes.[95] On the other hand, the photovoltage rise and fall time under 254 nm (42 μW cm^{-2}) was determined as fast as 64 ms and 43 ms, respectively (Figure 4d). One performance limiting factor of the utilized GQDs of the deep UV photodetector is the *IQE* of only 6%. It was shown that the GQD absorption can be increased by increasing the particle size. However, that would also lead to a more prominent graphene characteristic which means stronger carrier recombination due to shorter carrier lifetimes.[38,96,97]

Tang et al. introduced a microwave-assisted synthesis route for n-doped GQDs (N-GQD).[37] The N-GQDs showed remarkably broad absorption ranging from 300 nm to >1000 nm (**Figure 6**g), covering the UV, VIS and NIR range. The UV absorption was similar to what has been observed previously and was attributed to the transitions in C=C, C=N and C=O bonds. Extended partial conjugated π-electrons in the single graphene layers are responsible for the VIS absorption, and a more extensive π-electron delocalization due to the layered structure is the source of the NIR absorption. The optical transitions are illustrated in detail in Figure 6a-f in correspondence to their structural origin. To demonstrate the photosensitivity of the material, Tang and coworkers prepared a photoconductive detector device by drop casting the N-GQDs on an interdigitated gold finger substrate. Interestingly, the observed photocurrent was negative under illumination, similar to what was later observed as well by Lai et al.[71] The authors suggested a transport mechanism in which the photoinduced trap-states dominate. These states manifest due to the surface passivation of the GQDs, preventing a barrier free transport between individual QDs. As a consequence, the charge carriers transported across the GQDs were heavily restricted, thus it was necessary to increase the required bias voltage in order to maintain a constant current. In this case, the photovoltage was taken as a measure, and the responsivity was determined as 4.79 V W^{-1} (at 980 nm), 10.91 V W^{-1} (at 808 nm), 325.00 V W^{-1} (at 405 nm), and 1.14 V W^{-1} (at 365 nm) for the different excitation wavelengths. The response times for all wavelengths were on a seconds time scale, and the photocurrent did not saturate.[37]

The presented devices show that GQDs can be precisely tailored in their absorption behavior and harvest photons all the way into the NIR. Nevertheless, due to various defects and surface passivation, the energetic landscape of the particles is rather complex, and the relation to electrical transport still needs to be established. In order to make up for the yet impaired charge transport properties in GQDs but still benefiting from their broadband absorption hybrid structures are a viable alternative.

Cheng and coworkers for instance could demonstrate how graphene can be used for a successful exciton separation in GQDs.[49] They manufactured an all carbon phototransistor of graphene quantum dots (average diameter of 6 nm, consisting of 10–15 graphene sheets) dispersed on a single graphene layer, supported by a Si/SiO_2 substrate. The drain and source contacts

© 2016 WILEY-VCH Verlag GmbH & Co. KGaA, Weinheim

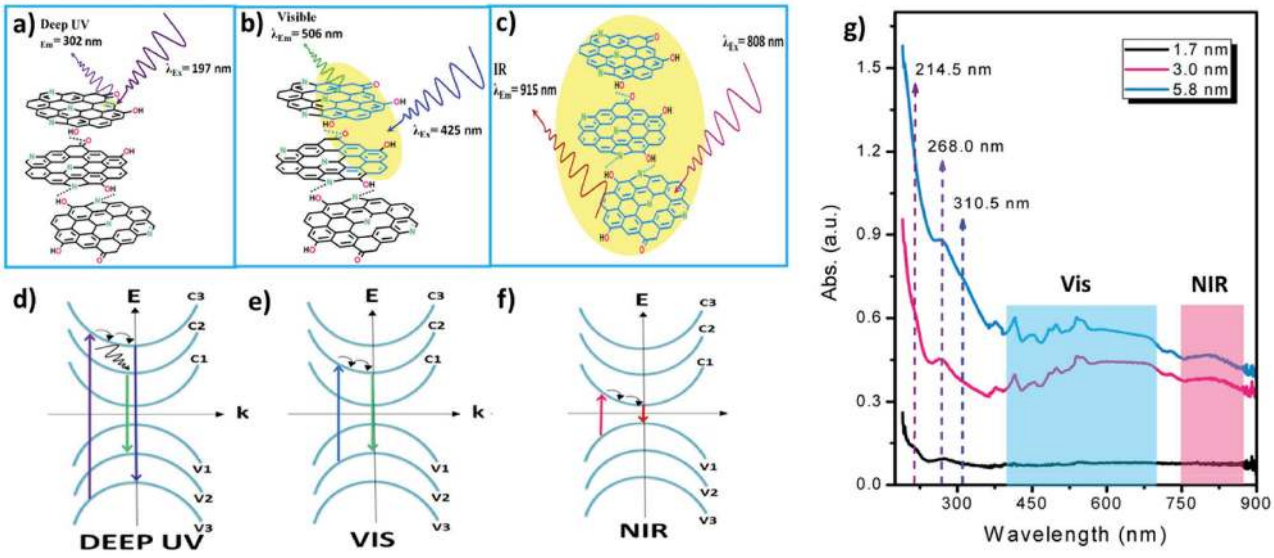

Figure 6. a)–f) Illustrations of the broadband absorption and emission in N-GQDs: a) deep UV absorption by carbon based double bonds. b) VIS absorption by partially conjugated sp^2-carbons in the layered N-GQD structure. c) NIR absorption by a more global, hence larger, delocalized π-electron system across the N-GQDs. c) Possible vibrational relaxation and interband transitions, being responsible for the also broadband photoluminescence of N-GQDs. d)–f) Suggested transitions from the valence (v) to conduction band (c). In agreement with these suggested optical transitions, the absorption spectrum in g) increases in the VIS-NIR region with increasing particle size. Reproduced with permission.[37] Copyright 2014, American Chemical Society.

on the graphene were made from a carbon conducting paste, in a way that the channel dimensions resulted in a width and length of 8 µm and 100 µm, respectively. Without the GQDs dispersed on the graphene, the photocurrent was not observable. However, with the GQDs dispersed on graphene, the photocurrent and spectral responsivity followed the absorption spectrum with a dominating UV absorbance at 360 nm (bandgap E_g = 3.44 eV) and an additional peak at 470 nm. Evidently, the number of graphene layers inside the GQD lead here as well to a partially extended sp^2 conjugation, creating photoactive defect states within the bandgap. Nevertheless, photocurrent gain and responsivity were determined at 325 nm in the order of 10^9 and 4×10^7 A W^{-1}, respectively. Rapid PL quenching in GQDs was taken as an additional proof for a successful charge transfer to graphene. Increasing p-type doping of the graphene layer in contact with GQDs, even in the dark, indicated a hole transfer from the GQDs to the graphene. Under illumination, the transfer was further facilitated, and subsequently increased the hole accumulation in graphene. An explanation for this behavior could be that the GQDs have an estimated HOMO (LUMO) at –6.14 eV (–2.7 eV) and are intrinsically p-doped.[49] Hence, their Fermi energy must be above 6 eV but below the Dirac-point of graphene at –4.5 eV. This results in a band alignment, thus hole transfer from the GQDs to the graphene. It is suggested that this charge carrier transfer could account for the initial faster photoresponse with a time constant of 5 s when the light is on and 13 s when the light is off. Latter would correlate with a slower recombination rate of spatially separated electrons and holes.[49]

Alternatively, reduced graphene oxide (rGO) can be used for charge separation from GQDs as well. The photoconducting device presented by Tam et al. was based on a rGO sheet contacted by two gold electrodes.[98] The rGO was decorated with GQDs of 4.4 nm, consisting of 1–3 graphene layers exhibiting a bandgap of 3.1 eV. Under 325 nm (20 µW cm^{-2}) UV illumination, they achieved an optimal detector performance with a responsivity of 870 A W^{-1} and a detectivity of 7.7×10^{13} Jones. The signal scaled linear with the increasing intensity, and the lowest detectable intensity was determined at 0.4 µW cm^{-2}. Unlike Cheng and co-workers, the proclaimed mechanism behind the photo-response was attributed to a photo-electron transfer from the GQD to the rGO, instead of a hole transfer. To support their statement, they determined the LUMO (HOMO) of the GQDs at –3.76 eV (–6.85 eV), thus suspected an electron transfer from the LUMO to the rGO which has a workfunction at –4.5 eV. Interestingly, the response speed was much slower than the response speed measured for Cheng's device. The rise (fall) time at 1 µW cm^{-2} was 40 s (24 s) and increased with increasing light intensity.

Graphene does not only facilitate exciton separation in GQDs but can also be used as an ambipolar contact material for GQDs. Kim et al. presented another carbon-carbon hybrid photoconducting detector by sandwiching GQDs in between two graphene sheets (**Figure 7**a) and thereby realizing a broadband detector bridging the spectrum from UV (300 nm) to NIR (1000 nm).[56] The synthesized GQDs had an average diameter of 17 nm and were incorporated with a layer thickness of 45 nm in between two graphene sheets. A Si/SiO_2 wafer served as substrate, and two Ag electrodes were evaporated onto the bottom and top graphene for an improved connectivity. Despite the symmetric device architecture, an asymmetric IV behavior was observed, which was attributed to the doping or charging effects in the graphene layer at the bottom and in contact with the SiO_2. The potential barrier between the Fermi energy level of the bottom graphene/GQD contact and the LUMO of the GQDs was determined as 2.2 eV and 1.4 eV in between the Fermi

© 2016 WILEY-VCH Verlag GmbH & Co. KGaA, Weinheim

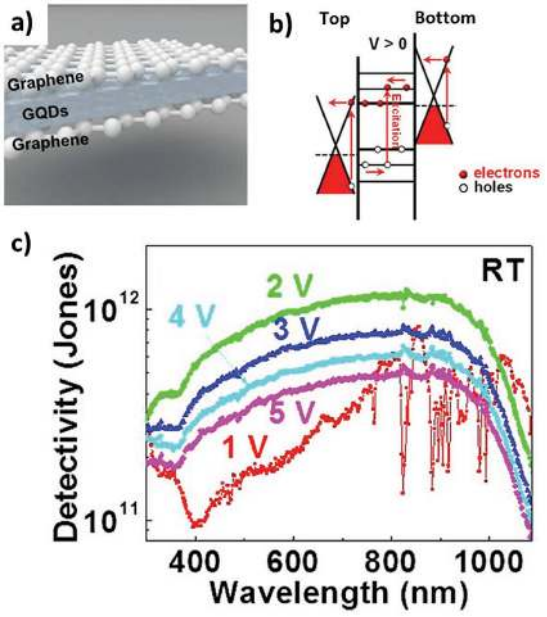

Figure 7. a) Illustration of GQDs sandwiched in between two graphene sheets. The contact interface of the bottom graphene with the SiO_2 substrate leads to a different contact barrier, as compared to the top graphene layer. When the device is positively biased, the energy level of GQDs and the graphene contacts align beneficially, and a photocurrent can be extracted. c) The absorption bandwidth of GQDs is exploited and results in a good detectivity, spanning from the UV to NIR, at room temperature. Reproduced with permission.[56] Copyright 2014, Macmillan Publishers Ltd.

energy of the top graphene and HOMO of the GQDs. This indicated that the photogenerated electrons and holes could only be extracted via a forward bias over the top and bottom graphene, respectively, when the extraction barrier was minimized (Figure 7b). This is usually observed if an external electric field exceeds the potential barrier height, and an additional thermionic emission process over the contacts starts to dominate the device current. Hence the photo-response measured was also bias dependent, showing an optimum only between 1.6 V–2.1 V with an on/off ratio of almost one order of magnitude. Consequently, the detectivity was measured the highest at 2 V bias, peaking at 900 nm with 2.4×10^{11} Jones and remained above 1×10^{11} Jones from 300–1100 nm. As the spectrally resolved detectivity at Figure 7c shows, an increasing bias is detrimental for the graphene-GQDs-graphene photodetector performance. The responsivity at 2 V bias peaked with 0.36 A W^{-1} at 800 nm and dropped below 0.2 A W^{-1} for wavelengths below 500 nm and above 1000 nm. Highest responsivity was achieved with 0.5 A W^{-1} at 800 nm and 5.5 V bias. The overall performance of the detector could be improved by cooling it below 200 K at which the thermionic emission cease, and the leakage current reduced to small tunneling currents. Nevertheless, the photo-response of the detector at room temperature was linear from 10 nW cm^{-2} to 1 mW cm^{-2} giving a linear dynamic range of 95dB. At higher intensities, the photo-response became bias dependent due to the charge carrier extraction across the bottom and top graphene layer, both having different barrier heights, leading to an accumulation of carriers and saturation of the photocurrent. The device response speed, investigated by ps-pulse experiments with a 532 nm laser, showed very fast turn-on transient with a time constant in ns regime. The fall time, on the other hand, showed two mechanisms, at which the slower was attributed to the carrier drift under the decreasing internal field with a time constant of 80 µs (at 2 V bias).

The overall progress in GQD-based photodetector devices has demonstrated that GQDs can serve as photoactive material for UV-VIS-NIR detection applications. A comparison with C60-photodetectors, as provided by Table 1, reveals that the device performance is already comparable. Moreover, for GQDs the optical properties of the particles can be tailored through synthesis, doping and surface modifications. That makes them a material class highly appealing for further research and development of solution-processed broadband detectors. Equally important, but little addressed so far, is the electrical transport and accessibility of GQDs in order to extract or separate photogenerated charge carriers to an external circuit. Fortunately, GQDs carry some of the electrical properties of their graphene or graphene oxide constituents. Nevertheless, the moderate reaction times observed in GQD devices are indicating a strong influence by e.g., reoccurring trapping and de-trapping events on the electrical transport. Since some energetic defects are also responsible for optical band transitions it remains a future task to understand and optimize these interconnected properties even further.

4. One-Dimensional CNTs for Photodetection

The first published observation of a carbon nanotube like structure dates back to 1960 by Roger Bacon.[99] He described a tubular structure of a scrolled-up sheet of graphene with some micrometers in diameter. Much later in 1991, Sumio Iijima published on nanometer-sized hollow carbon tubes, which are more accurately described by a rolled-up sheet of graphene.[100] Ever since the invention of CNTs, as they are used nowadays by many scientific communities, is credited to him. Since CNTs also are sp^2 hybridized carbon atoms, they were actually assigned to the class of fullerenes which were discovered six years earlier. Nevertheless, the name 'CNT' became the established name in literature, since their gigantic aspect ratio gives them a rather one-dimensional character, in contrast to 0D fullerenes. In the meantime, the chemical synthesis as well as the physical understanding of various CNT types advanced tremendously.[101,102] Especially after 2004 when the first preparation of a single graphene sheet succeeded, the investigation of some of its properties helped also to understand CNTs even better.[32] Unique for CNTs is the 1D quantization of the electron wave function around the single-walled carbon nanotube (SWCNT) circumference leads to the formation of an electronic band-structure, not inherent to graphene. Whether this band-structure provides the SWCNT with a metallic or semiconducting nature depends on the so-called chirality which is indicated by two indices, n and m. Each of which stands for a pre-factor of the unit vectors a_1 and a_2 of the hexagonal graphene lattice. On this basis, the chiral vector C_h can be determined according to $C_h = n\ a_1 + m\ a_2$ and unambiguously describes the chiral angle θ and the CNT's final structure. Since

© 2016 WILEY-VCH Verlag GmbH & Co. KGaA, Weinheim

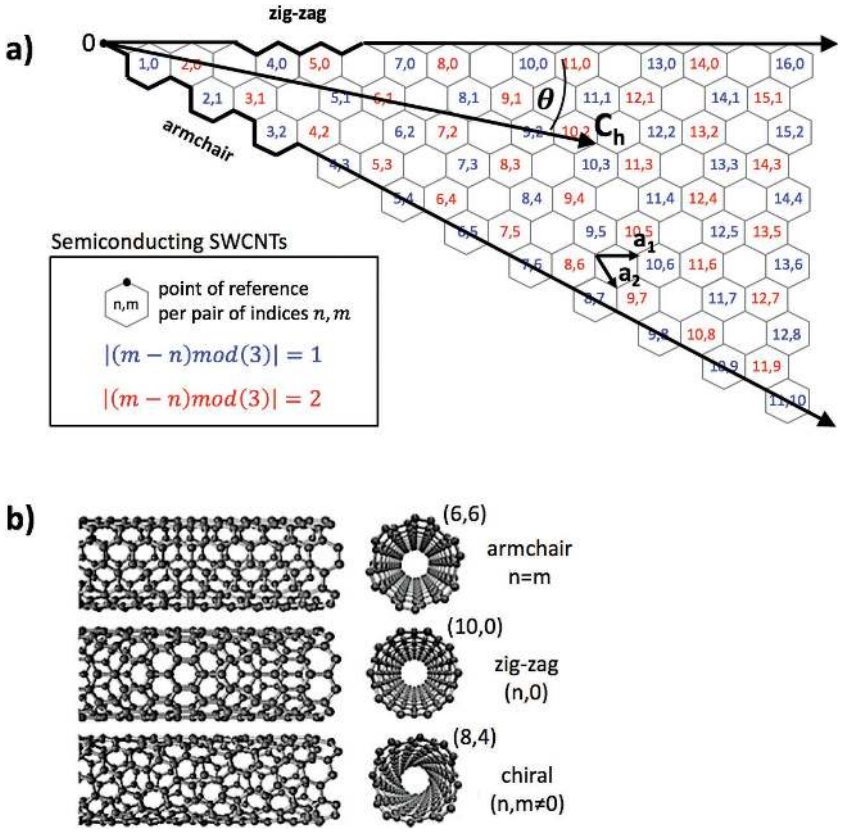

Figure 8. All given pairs of indices in a) indicate the possible chiral or roll-up vectors for semiconducting SWCNTs on a flat graphene segment. b) Tube structures of SWCNTs. Adapted with permission.[16], published under the CC-BY license.

the length of the chiral vector stands for the circumference of the SWCNT, the diameter is easily derived from it as well.

In **Figure 8**a, the unit vectors and several chiral vector points for semiconducting SWCNTs are indicated on a graphene segment. For $n = m$, the SWCNT exhibits an arm-chair like structure at both of its ends and is always metallic. The zig-zag structure emerges for all SWCNTs with $m = 0$ and can be metallic or semiconducting. SWCNTs with an arm-chair and zig-zag structures are considered achiral. Hence, chiral SWCNTs only exists when $n \neq m \neq 0$. In Figure 8b, one SWCNT is illustrated representative for each structural type. To distinguish the nature of the SWCNT, two mathematical rules can be applied. If $(m\text{-}n)\text{mod}(3) = 0$ holds the SWCNT is metallic, whereas for $(m\text{-}n)\text{mod}(3) = 1$ or 2 semiconducting properties can be ascribed to the SWCNT. Thereof, statistically 1/3 of all SWCNTs within one synthesis batch is metallic. Thus, in order to access the full potential of semiconducting SWCNTs ideally the metallic ones should be removed from the batch since they lead to shunts and increased charge recombination in opto-electronic devices.[103]

As previously mentioned, the 1D confinement in SWCNTs results in a quantization of the wave-vector perpendicular to the SWCNT axis. This leads to a characteristic distribution of density of states in k-space per energy level. The emerging sharp features in the distribution, so-called van Hove singularities (**Figure 9**a), represent the occupied (valence) and unoccupied (conduction) states between which interband transitions can be optically excited or charge recombination may lead to photoluminescence.[104] Hence, the transitions S_{11}, S_{22}, S_{33} and so on represent the bandgap E_g and sub-bandgaps, respectively, in semiconducting SWCNTs. The bandgap is defined as $E_g = 2h\nu_F/3\pi d$ and scales inversely with the tube diameter d; ν_F stands for the Fermi velocity. Most of the electronic transitions in CNTs with different chiralities can be identified by the means of spectroscopic methods. Plotting the transitions versus the tube diameter results in the Kataura plot (Figure 9b).[105,106] Basically, for semiconducting SWCNTs with diameters in the range of 0.7–2 nm, the transition S_{11} scales from 1.1 eV to 0.4 eV and the S_{22} transition from 2.2 eV to 0.7 eV, covering the VIS and NIR parts of the spectrum. All transitions can be clearly identified as sharp peaks in the absorption spectrum.[16,28] Furthermore, each sub-bandgap has a specific angular momentum, again attributed to the 1D confinement, which makes the electronic transitions in SWCNTs susceptible to polarized light. In case the direction of light polarization is parallel to the tube's c-axis, the extinction coefficient gets maximized and can approach to 10^5 cm^{-1}.[21,107–109]

Another effect of 1D confinement in SWCNTs is an enhanced Coulomb interaction between charge carriers. After optical excitation, electrons and holes remain in an excitonic state with high binding energies of about 0.4-0.5 eV, depending on the tube diameter.[110–115] Hence, charge separation into free carriers can be only achieved through an external bias or an internal electrical field via Schottky-barrier or pn-junction.[116–118] After charge separation, free charge carriers can have mobilities reaching from 10^2 to 10^5 cm^2 V^{-1} s^{-1} in semiconducting SWCNTs. The actual mobility strongly depends on the CNT batch quality, method of preparation and tube alignment.[119–121] Despite these extraordinary electrical properties, the optical absorption cross section of a single CNT is very small. In order to achieve photodetector sensitivities relevant to practical applications, CNT networks and films are more of interest. Therefore, our focus in the following section will include devices comprising CNT layers rather than single CNT devices.[122]

In a single semiconducting CNT, the exciton lifetime can be in the order of ns, hence the expected diffusion length along the CNT is, with respect to the high mobilities, up to hundreds of nanometers.[123] Within a CNT film, the electrical transport is strongly influenced by CNT-CNT junctions and defects. Moreover, with the presence of metallic CNTs, the non-radiative charge recombination time is drastically reduced to 1 ps and potentially restricting applicable device dimensions.[122,124] As part of the non-radiative nature of charge recombination of metallic CNTs or CNT defects (junctions), the exciton energy is transferred to the carbon lattice in the form of heat. Because

© 2016 WILEY-VCH Verlag GmbH & Co. KGaA, Weinheim

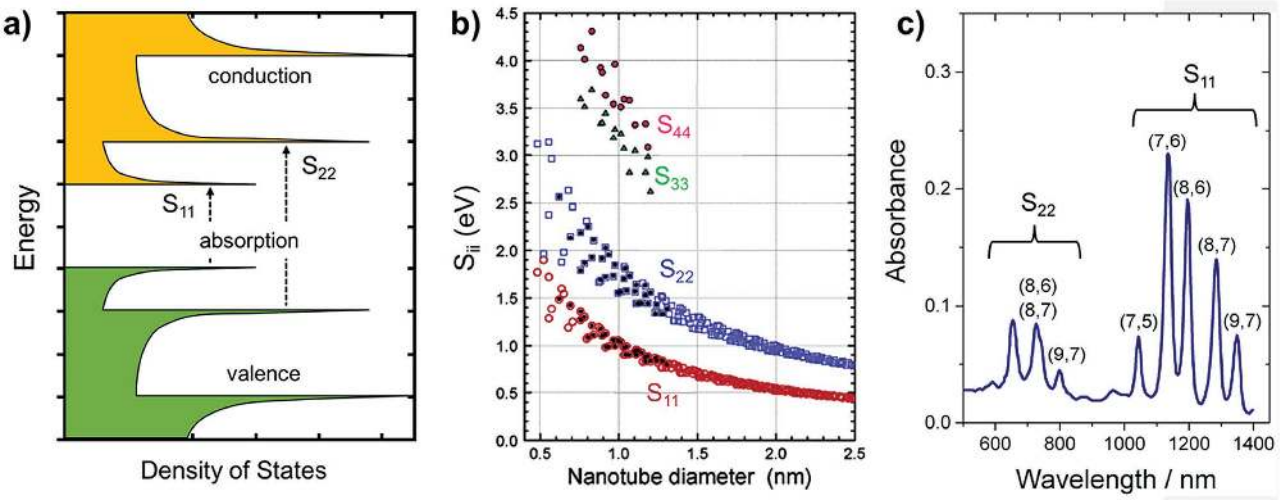

Figure 9. a) Schematic of a typical distribution of the density of states found in semiconducting SWCNTs. S_{11} and S_{22} indicate excitonic transitions between the bandgap and sub-bandgap, respectively. b) Kataura-plot shows the electronic transitions in semiconducting SWCNTs in dependence of the tube diameter. Solid symbols represent measured values, and open symbols are empirical extrapolations thereof.[106] Adapted with permission.[106] Copyright 2003, American Chemical Society. c) Absorption spectrum of a mixture of semiconducting SWCNTs of various chiralities, dispersed with poly(9,9-dioctylfluorene) in toluene. Adapted with permission.[16], published under the CC-BY license.

CNTs hold significant Seebeck coefficients of 40 μV K^{-1} and ≈200 μV K^{-1} for metallic and semiconducting SWCNT, respectively, they show a thermoelectric and bolometric effects as well.[29,53,125,126] Hence, a photocurrent, due to separated electrons and holes, is always accompanied by thermoelectric and bolometric effects, if not otherwise controlled. By blending different chiralities into a CNT film, one can tailor the superposition of many individual VIS and IR absorption features and even reinforce THz interaction by an increasing degree of alignment.

4.1. CNT Photodetectors

It was shown by several groups that a photocurrent can be generated in a single CNT, which is in contact with a metal electrode, when illuminated.[127] A Schottky barrier, established at the metal/CNT interface, provides a sufficient internal electrical field for charge separation. The work closest to showing photoconductivity in a pure CNT film was published by Rao.[128] They grew SWCNTs via CVD process on a Si/SiO2 substrate across a trench, etched into the SiO_2 layer. Approximately 8–20 SWCNTs bridged the trench and were symmetrically contacted by two aluminum electrodes. In order to exclude uncontrolled doping by adsorbed oxygen or thermal effects, the IR detection experiments were conducted under vacuum at 77 K. The electrical resistance decreased by 45 kOhm at 50 mV under IR irradiation (4 mW, spectrum not provided), providing a low frequency S/N ratio of 45 at best. Actual band to band excitation was held responsible due to different reasons: the high intrinsic thermal conductivity in single SWCNTs was not restricted by CNT-CNT junctions, and the photovoltage response was found to be only 500 μs. For bolometric effects, the time constants are usually much slower in the order of a few ms. On the other hand, the authors also reported a significant *TCR* of –1.23% K^{-1} for their detector which is underlining the difficulty of allocating the origin of a photoresponse.

An alternative approach to achieve charge separation in CNTs is to establish a pn-junction. Chemical doping and split-gate structures have been applied for that reason. Whereas the former can be detrimental to the CNT lattice, degrading the intrinsic properties of SWCNT, the latter is more suitable for conducting fundamental studies rather than building easy-to-process and miniaturized photodetectors. A third possibility is to apply asymmetric metal contacts to the CNTs. In this geometry, p- and n-regions are automatically formed in proximity to either of the contacts. In particular, the metals Sc and Pd have been demonstrated to establish perfectly ohmic contacts by promoting energy level alignment between the Pd (Sc) work function and the $HOMO_{CNT}$ ($LUMO_{CNT}$) of a SWCNTs. Accordingly, such devices are described as barrier-free-bipolar diode (BFBD) which can exhibit a photovoltage ultimately limited by the bandgap of the CNTs.[129] Building a BFBD type photodetector Liu and co-workers utilized highly purified semiconducting SWCNTs, which were deposited from liquid-phase on an n-Si/SiO_2 substrate, forming a homogeneous film (**Figure 10**a).[39] As described above the film was contacted by asymmetric, metal contacts of Sc and Pd. The IV curve of the device was modeled in good agreement with the standard diode equation, and the overall good diode performance was attributed to the reduced amount of defects in the SWCNTs due to the mild processing conditions. Looking into the definition of the open circuit voltage V_{oc} of a photodiode (Equation (11)), it can be deduced that even for undetectable short circuit currents I_{sc} a V_{oc} can be still generated, provided that the dark current or saturation current I_0 (at 0 V bias) is small enough. Liu et al. could further amplify the V_{oc} photoresponse by applying repeatedly virtual contacts of Sc/Pd across the SWCNT film (Figure 10b). The virtual contacts did not have any physical contact to the main electrodes, thus the photodetector behaved like several photodiodes connected in series, and the V_{oc} scaled linearly from 0.26 V for a single diode to 2.12 V for ten virtually connected diodes. The charge transport and the cascaded

© 2016 WILEY-VCH Verlag GmbH & Co. KGaA, Weinheim

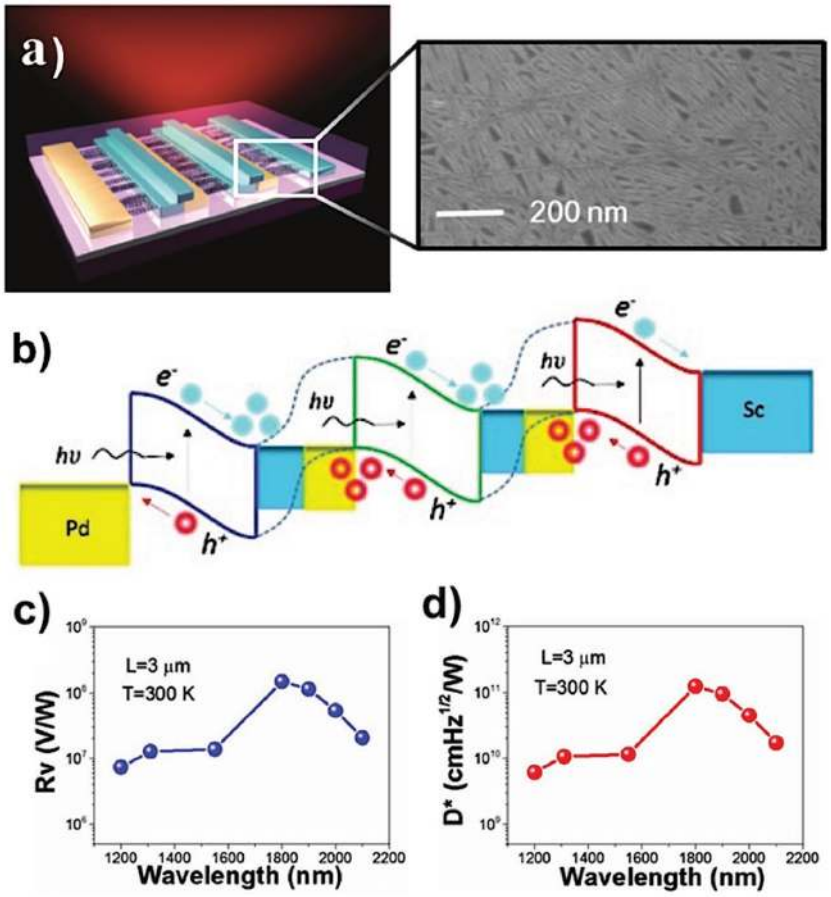

Figure 10. a) 3D rendering of the SWCNT cascade-detector with two virtual contacts. The inset shows the TEM Image of the morphology of SWCNT film as deposited from the liquid phase. b) Shows the energy band alignment of CNT BFBDs, in conjunction with the metal contacts. The total V_{oc} of the cascade detector increases linearly with the number of virtually series-connected photodiodes. The graphs c) and d) show the spectral responsivity and detectivity of a detector with ten virtually connected photodiodes, respectively. Reproduced with permission.[39] Copyright 2016, Wiley.

band diagram of such device are depicted in Figure 10c for N = 3 diodes.

$$V_{oc} = \frac{nkT}{q} ln\left(\frac{I_{sc}}{I_0} + 1\right) \tag{11}$$

Under open circuit conditions, the detector was Johnson or thermal noise limited. Whereas the S/N ratio scaled with the expected factor of √N, the voltage noise increased less than expected. Hence, for a ten-diode detector with a length of 3 μm, the peak responsivity under a light intensity of 670 mW cm^{-1} at 1800 nm reached to 1.5×10^8 V W^{-1} and stayed above 10^7 V W^{-1} for the wavelength range of 1200 nm–2100 nm. The spectral detectivity remained above 10^{10} Jones in the same spectral range with its maximum peak at 1800 nm with 1.25×10^{11} Jones (Figure 10d).[39] The highest sensitivity of the cascade detector at 1800 nm was ascribed to the average SWCNTs diameter inside the film, which was 1.5 nm. The signal response time of ≈20 ms, together with all other measurements were acquired at room temperature.

One disadvantage which comes with such cascade detector design, operated under open circuit conditions, is that V_{oc} scales logarithmically with light intensity. In fact, this effect was also observed here, as the detectivity dropped three order of magnitude for light intensities exceeding 3 W cm^{-2}. Nevertheless, the cascade detector showed remarkable temperature and high power illumination stability, exceeding those of InGaAs detectors. For several million switching cycles under 100 kW cm^{-2} illumination at 785 nm, no degradation of the photocurrent was observed. Thermal excitation of carriers as the origin of the IR response was excluded via low temperature experiments, at which the detector performed even better. Despite the cascade detector's outstanding performance, the possibility of broadening the good device detectivity seems to be limited by the metal contacts. Nevertheless, Liu et al. determined and maximized the generated photovoltage, without relying on even scarcer metals.[39] However, as soon as the band alignment with the SWCNTs cannot be established anymore by the metal contacts, the BFBD concept loses its effectiveness.

The transition from photonic detection to temperature sensing is seamless and can only be distinguished by the underlying physical effect leading to a signal generation, especially for broadband detectors. In case of contactless temperature sensing, bolometers are used where the change of electrical resistance within an absorber material is detected upon a temperature change, recognized as the bolometric effect. As introduced earlier, CNTs are ideal IR absorbers, and the bolometric effect is observed whenever photogenerated excitons lose their energy to lattice phonons, instead of being dissociated into free carriers. The heat dissipated in that process leads to a significant TCR in CNTs, even at room temperature. Thus, CNTs are especially interesting as absorber material for room temperature-operated bolometers and thermoelectric detectors and were extensively investigated by the scientific community. In this review, we only want to highlight some works and refer to others for a broader overview on that matter.[62–64,122,130]

Within the temperature detection approach, Narita et al. developed a plastic IR bolometer suitable to an all printed manufacturing process.[64] They embedded an MWCNT-based thermistor (500 × 500 μm) with asymmetric contacts of Au and Ti into an insulating matrix of parylene, sandwiched between an Al reflector and an additional CNT-based top absorber. A TCR of –2.1% K^{-1} was reported at 300 K. The responsivity reached to 138 V W^{-1} (at 2 V bias), and NETD was as low as 1.1 K. The response time was fast enough to realize an array sensor with a readout speed of 30 frames s^{-1}, enough to track the blackbody source which was used for irradiation.[64]

© 2016 WILEY-VCH Verlag GmbH & Co. KGaA, Weinheim

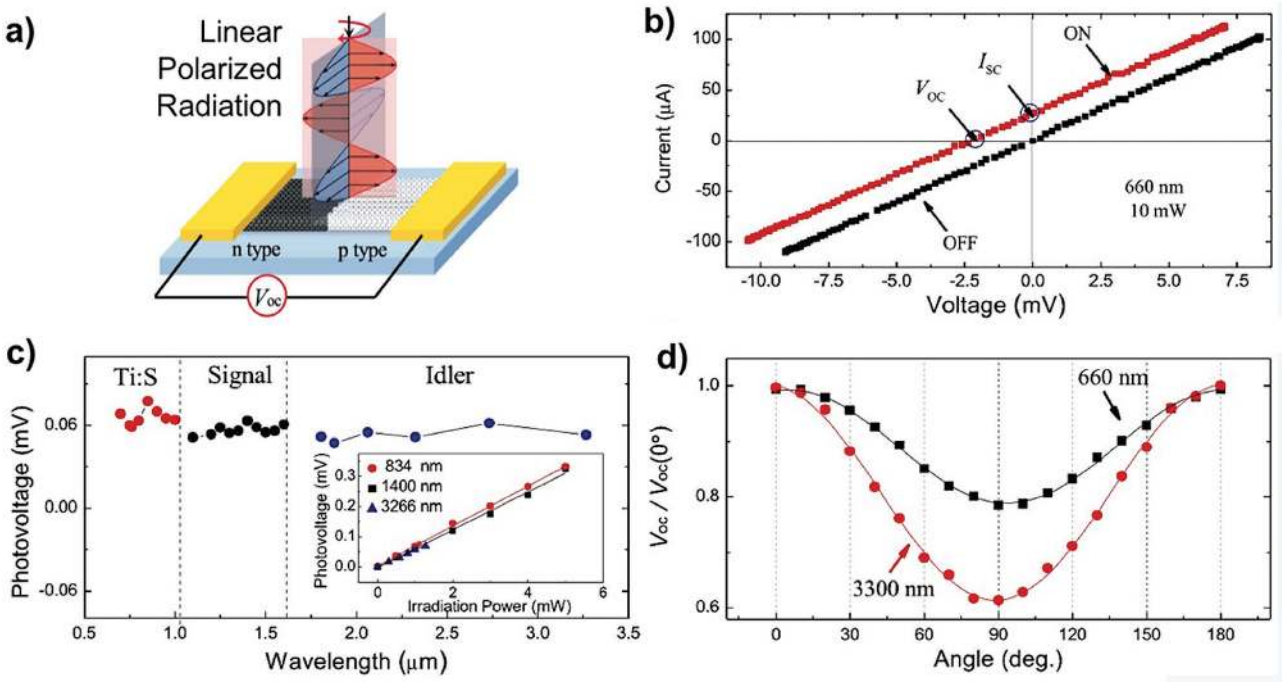

Figure 11. a) Schematic drawing of a thermoelectric photodetector based on two overlapping p- and n-doped highly aligned SWCNT films. b) The on and off IV curve of a p-n junction photodetector under 660 nm illumination. c) Broadband photovoltage response of the detector under an illumination power of 1 mW. Inset shows the linear power dependency of the photovoltage for three different wavelengths. d) The polarization sensitivity towards 660 nm and 3300 nm. Reproduced with permission.[40] Copyright 2013, American Chemical Society.

In order to enhance the bolometric response in single CNTs even further, plasmonic nanostructures were integrated into the devices. In the work of Mahjouri-Samani and co-workers small diamond-shaped nanometer-sized antennas were prepared on a Si/SiO_2 substrate.[63] MWCNTs were grown by a laser-assisted CVD process in between the antenna tips. The diamond shape lead to a strong heating effect at the tips of the antennas, due to a strong enhanced optical field. Despite a rather small *TCR* of 0.3% K^{-1}, they were able to record a photoresponse of 800 V W^{-1} under an illumination power of 10 mW mm^{-2} at 10.6 μm. The detectivity was determined as 1×10^7 Jones, and the response time was as fast as 25 ms. So far, this responsivity belongs to one of the highest reported for CNT-based bolometers, operated at room temperature.[63]

A higher detectivity of 1.22×10^8 Jones has been reported for SWCNTs in a polyvinylpyrrolidone matrix, though only within a narrower absorption bandwidth of 300 nm–3 μm.[130] The highest TCR reported so far is about 10% K^{-1} for SWCNTS in a matrix of poly(N-isopropylacrymide). This value was achieved by increasing the activation energy within the SWCNT film through an increased inter-tube distance, triggered by a volume phase transition of the polymer. However, the transition was irreversible depending on the temperature and humidity, which makes further improvement in the bolometer design necessary.[62]

Alternatively, accessing the thermo-electric properties of CNTs seems to be an equally viable approach for the extension of absorption towards long wavelength THz radiation. The group of J. Kono introduced such a photodetector made from CVD grown, mixed metallic and semiconducting SWCNTs (**Figure 11**a).[40] The vertically-grown SWCNTs were flattened into a macroscopic band of highly aligned SWCNTs. By overlapping two such SWCNT bands, one of which was kept intrinsically p-doped and the other n-doped through benzyl viologen addition during growth, a pn-junction was generated. The device was completed by two gold electrodes evaporated separately on each band, which was previously evaluated as the best choice.[131] Figure 11b shows how the linear IV curve of the device experienced a parallel shift under illumination, showing a minor photovoltaic response with $V_{oc} = 2$ mV and a $J_{sc} = 25$ μA for a wavelength of 660 nm and illumination power of 10 mW. Under an illumination power of 1 mW, the photovoltage response (Figure 11c) of the device was essentially constant at 60 μV, ranging from 700 nm to 3300 nm. Additionally, the polarization angle dependent photovoltage response in Figure 11d informed on a much higher sensitivity towards radiation, which is parallel polarized with respect to the CNT's c-axis. The longer the wavelength, the higher the sensitivity becomes. By performing scanning photovoltage microscopy, the photothermoelectric effect was found to be strongest at the edges of the n- and p-doped SWCNT-bands. Therefore, for a very narrow pn-junction, both voltage maxima V_n and V_p at the edges overlapped and generated the largest signal. This excluded a junction induced, photovoltaic-like effect and supported the PTE effect, which could be based on the difference in Seebeck coefficients S_n and S_p for differently doped SWCNTs.

$$\Delta V = V_p + V_n = T_{max}\left(S_p e^{\frac{|x_0 + L/2|}{\varphi}} - S_n e^{\frac{|x_0 - L/2|}{\varphi}}\right) \quad (12)$$

© 2016 WILEY-VCH Verlag GmbH & Co. KGaA, Weinheim

The device behavior could be modeled with respect to Equation (12) which gives the total photovoltage ΔV in dependence of the exponentially decaying temperature profile T_{max} away from the heating light spot position x_0 and the respective SWCNT band edges $L/2$. Basically, the PTE depends on the thermal length scale for optical heating φ. Because of the very low heat capacity in CNTs, φ is predominantly determined by the thermal conductivity of the device substrate. Accordingly, He et al. observed for a Teflon substrate, which has a lower thermal conductivity, the highest photovoltage responsivity of 1 V W^{-1}.[40] For a better thermal conducting substrate, like AlN, the heat dissipation away from the pn-junction was much faster, resulting in a lower photovoltage. On the other hand, the heat conduction scaled inversely with the time, thus the temporal response with an AlN substrate (t_{rise} = 90 µs, t_{fall} = 84 µs) was much quicker than on Teflon (t_{rise} = 600 ms).[40]

Shortly after, the same group improved the detector performance even further by growing the highly aligned SWCNTs perpendicular to the current direction between the two gold contacts (**Figure 12**a).[21] As mentioned above, half of the intrinsically p-doped SWCNTs were n-doped to establish the pn-junction. This time however, the differently doped SWCNT arrays were just touching each other at the very edge with minimal overlapping. Experimentally, significant Seebeck coefficients of the p-SWCNTs (S_p = 75.2 µV K^{-1}) and n-SWCNTs (S_n = −71 µV K^{-1}) could be derived and led to a thermovoltage of ΔV = 1.53 V W^{-1}. For the photoresponsivity under THz irradiation, similar values were found. Basically, the highly aligned SWCNTs led to an extended absorption spectrum (Figure 12b), covering the range from 0.1 THz up to >100 THz (or from 3 µm up to 3 mm in wavelength). For a polarization sensitive THz detector, the responsivity values are the highest reported yet with 2.5 V W^{-1} at 3.11 THz (96.5 µm), 2.4 V W^{-1} at 2.52 THz (119 µm) and 1.7 V W^{-1} at 1.39 THz (215 µm). The NEP of the detector was determined as 20 nW $Hz^{-1/2}$ which is promising, as compared to the existing room temperature-operated THz detectors with NEP of 1 nW $Hz^{-1/2}$.[132] The anisotropic optical absorption behavior in CNTs had an extra strong reinforcing effect on not only THz absorption but also the polarization sensitivity. Under irradiation with a linearly polarized THz laser, the absorption was increased up to 60%, and the generated thermovoltage was five times larger, when the plane of polarization was parallel to the SWCNTs. The magnitude of the effect can be understood from the absorbance spectrum in Figure 12b. Nevertheless, the figure of merit ZT for the thermoelectric detector was determined as 2.6×10^{-6}, leaving room for future improvement. Since a ZT value of ≈0.08 was already reported for doped-SWCNTs, further engineering of the thermo-electric properties in CNT films is considered crucial.[133]

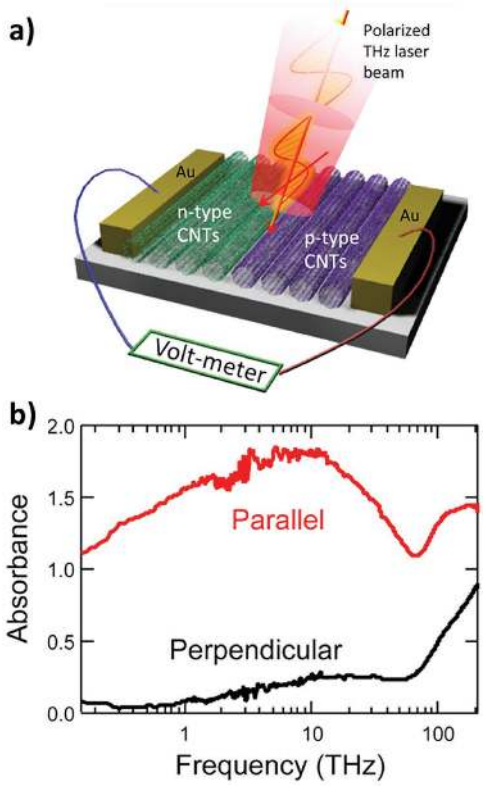

Figure 12. a) Device schematic of a THz detector based on highly aligned CNTs. b) Absorbance spectrum for highly aligned SWCNTs under differently polarized THz radiation. Reproduced with permission.[21] Copyright 2014, American Chemical Society.

4.2. CNT-Carbon Heterojunctions for Enhanced Photodetection

Implementation of heterojunctions pursues primarily the goal of facilitating a better charge carrier separation to increase the photocurrent generation in detector devices, especially for organic materials, where strong Coulomb attractions due to a low dielectric constant lead to high exciton binding energies. This concept has been already successfully applied in combination with 0D carbon allotropes and has been proven viable for CNTs as well. In the following we want to highlight a few photodetectors which establish a beneficial heterojunction from one carbon allotrope to another.

Bindl and co-workers demonstrated a photovoltaic detector device by utilizing a planar SWCNT/C_{60} heterojunction, sandwiched between a transparent ITO bottom and BCP/Ag top contact (**Figure 13**a).[112] They took special care of removing all metallic SWCNTs from the mixture, using poly(9,9-dioctylfluorene) as a wrapping agent for the SWCNTs. The remaining SWCNT chiralities were (7,5), (7,6), (8,6), (8,7) and (9,7). Each chirality expresses a distinct absorption peak in the NIR due to S_{11} band excitation. The peak intensity strongly increased upon removing the metallic SWCNTs as potential recombination centers. SWCNT purification also helped the diode performance of the device by decreasing the dark current to 0.2 mA cm^{-2} at 1 V reverse bias and increasing the rectification ratio to ≈10^3. The evaporation of C_{60} on the SWCNT layer led to an efficient PL quenching in the CNTs and resulted with >90% IQE for the (7,6) and (8,6)-SWCNTs (Figure 13b). The driving force for charge separation was calculated based on the energy offset between the $LUMO_{C60}$ at −4 eV and the expected SWCNT work function for each chirality. A positive driving energy was a sign of improved charge separation and was in agreement with the observed trend in the EQE. Hence, the C_{60} layer was proven to be an effective electron acceptor with sufficient

© 2016 WILEY-VCH Verlag GmbH & Co. KGaA, Weinheim

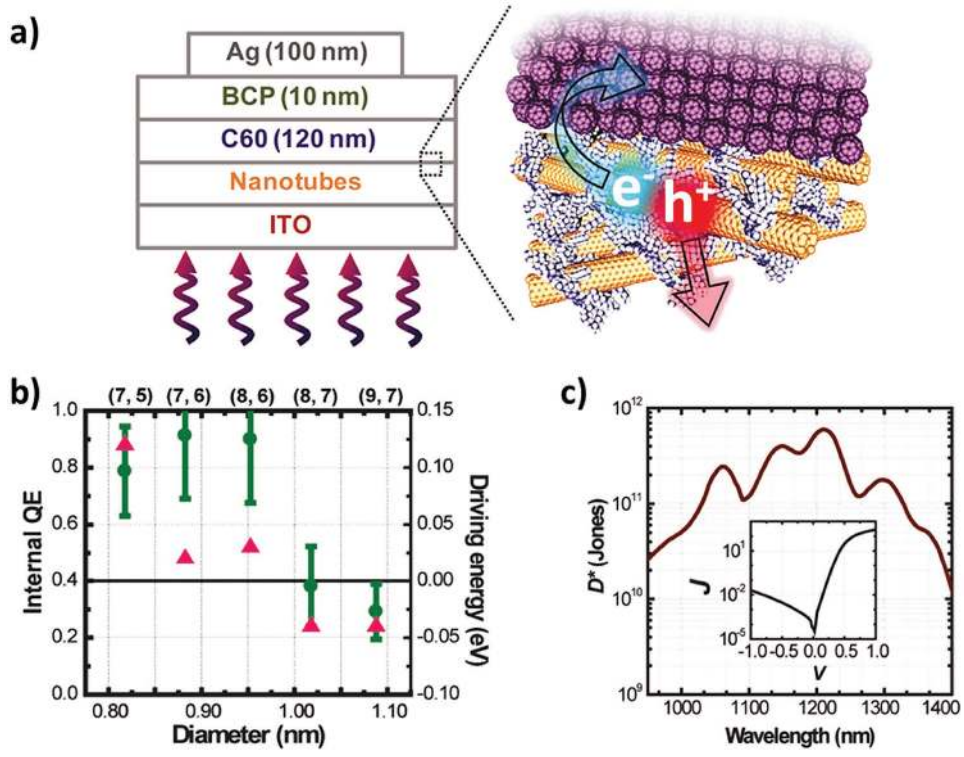

Figure 13. a) The layer stack of a CNT/C_{60} planar heterojunction photodiode and solar cell. The charge splitting at the interface is illustrated in the magnification. b) The *IQE* (circle) for CNTs with different chiralities and diameter and the excessive driving energy (triangles) for exciton dissociation. c) The spectral detectivity and the IV curve (inset) of the photodiode. Reproduced with permission.[112] Copyright 2011, American Chemical Society.

energy offset to spontaneously separate electron-hole pairs generated on semiconducting SWCNT.[134] The *EQE* of the devices had to be optimized by adopting an optimal layer thicknesses. This required the consideration of a trade-off between maximal absorption and efficient charge carrier extraction, a similar challenge known from many organic opto-electronic devices.[134]

Bindl et al. determined the effective diffusion length within the SWCNT/C_{60} heterojunction as $L_D = 0.13L_A \approx 3$ nm, where L_A is the estimated absorption depth (21 nm) at 1205 nm. The maximized *EQE* finally reached around 13% at 1205 nm (corresponding to the (8,6)-SWCNT absorption). Under broadband NIR irradiation (1000–1360 nm) with a power of 17 mW cm^{-2}, the presented device showed a solar cell performance with a power conversion efficiency of 0.6% (Jsc = 0.8 mA cm^{-2}, FF = 51%, V_{oc} = 0.25 V). Operated as a detector in the photovoltaic mode at 0 V bias, the specific detectivity peaked at 1205 nm with 6×10^{11} Jones and stayed in average over 10^{11} Jones within the wavelength range of 1000 nm–1300 µm (Figure 13c). Despite the improved CNT detector performance, the device was still limited by the effective exciton diffusion length across the SWCNT layer. Since the intratubular diffusion was determined as 100 nm,[123] the bottleneck is more likely the intertubular diffusion in isolated CNTs (exciton hopping from nanotube to nanotube mediated by thermally assisted scattering or Förster dipole-dipole coupling[135]). A possible reason suggested by the authors were the (8,7) and (9,7) SWCNTs incorporated in the CNT mixture. Both chiralities have diameters >1 nm and therefore smaller bandgaps, which could act as exciton traps. Additionally, due to the bandgap of <1 eV, the conduction band offset to C_{60} was not able to bring the necessary electronegativity for the exciton dissociation. This was evident by an up to 40%-reduced *EQE* at the absorption maxima, corresponding to the (8,7) and (9,7)-SWCNT contributions.[112] However, the overall success of the principle led to further explorations of CNT/C_{60} and CNT/PCBM heterojunctions for solar cells and photodiodes.[18,28,109,134,136]

Park et al. demonstrated a phototransistor by utilizing the CNT/C_{60} heterojunction concept.[58] The CNT absorption was in the same spectral range from 1000–1400 nm. A negative gate voltage was necessary to achieve good band alignment between the CNTs and C_{60}. After photoexcitation and charge dissociation, the holes were trapped on the CNTs, allowing a photoconductive gain in the order of 10^4. Hence, a maximum responsivity of 220 A W^{-1} could be achieved. The detectivity was based on noise current measurement up to 1 kHz and reached to 1.17×10^9 Jones. Furthermore, it is interesting to note that the presented CNT/C60 phototransistor did not suffer from performance losses even under a bending radius of 4 mm, when processed on a flexible substrate.[58]

Not only carbon allotropes from the 0D family showed the potential for improved charge carrier separation but also graphene from the 2D family was found to be a sufficient junction-forming material when combined with CNTs. Unlike C_{60}, which is absorbing partially into the VIS spectrum, graphene is not used for the expansion of the absorption spectrum, but rather a sufficient charge dissociation layer at the

© 2016 WILEY-VCH Verlag GmbH & Co. KGaA, Weinheim

CNT/graphene interface. In a proof-of-concept phototransitor Liu and co-workers coated a few monolayer thick layer of mixed SWCNT on a n-Si/SiO_2 substrate.[57] Subsequently, a CVD-grown graphene sheet was transferred on top of the SWCNTs. The SWCNTs had various diameters within the range of 1–1.6 nm with 1.4 nm in average, accounting for the absorption from 300 nm to 1600 nm. The positive Dirac point of the transistor's transfer curve indicated electrostatic p-doping of the graphene channel, suggesting a build-in field at the junction. Under illumination, the photogating effect led to a negative shift in the Dirac point, confirming an electron transfer from the SWCNTs to the graphene, while the holes remained trapped on the CNTs. The transfer is expected only for SWCNTs with a higher work function than that of graphene (–4.5 eV). Only a downward band bending towards graphene would lead to spontaneous exciton splitting and could be further supported by an applied negative back gate voltage. The device *EQE* for intensities <1 μW was 34% and decreased with increasing illumination power. Therefore, the highest device responsivity of 120 A W^{-1} was reached with an illumination power of 0.2 μW at 650 nm and ≈40 A W^{-1} at 1550 nm. These high values were supported by a photoconductive gain estimated in the order of 10^5. Consequently, the response time of 100 μs was attributed to the fast charge transfer and high carrier mobilities (>10^3 cm^2 V^{-1} s^{-1}).[57]

The device presented above incorporated a planar graphene/SWCNT heterojunction which remains challenging to prepare on a larger manufacturing scale. An alternative approach which can be applied to large scale production was demonstrated by Lu et al.[59] A mutual suspension of MWCNTs (40–60 nm in diameter) and 2 μm-sized graphene flakes, was coated on a Si/SiO_2 substrate with pre-deposited Au contacts. The formation of a type-II bulk-heterojunction was expected even for MWCNTs with a diameter of tenth of nanometers, as long as their work function is above –4.5 eV, creating enough driving force for exciton splitting. Moreover, having some metallic MWCNTs in the bulk-heterojunction is considered beneficial as they do not shunt the junction but rather improve the free carrier transport across the layer. The photoresponse of the photodetector to NIR illumination (1–1.3 μm with 0.3 mW mm^{-2}) increased by 400% compared to the reference device without graphene flakes. The responsivity was improved eightfold and saturated close to 10^4 V W^{-1} for a bias current of 3 mA. Since the device was determined to be 1/f noise limited, the detectivity increased with increasing frequency and saturated, despite the fast response time of 1.5 ms, at 100 Hz with 1.5×10^7 Jones, a fivefold improvement compared to the reference.[59]

4.3. CNT-Polymer Heterojunctions in Photodetectors

Pradhan et al. was one of the very first works, in which a strong increase of the infrared photoresponse by embedding SWCNTs in a thermally and electrically insulating matrix polymer was observed.[137] A concentration of only 5% SWCNT in a polycarbonate matrix showed a strong photoconductivity upon IR illumination, while in pristine SWCNT films the response was low and mainly due to thermal effects. For pristine films, the photoconductivity usually follows the substrate temperature closely, and the photoeffect is negligible. Numerous intertube junctions act as exciton traps that increase the probability of non-radiative recombination and decrease the free charge carrier collection.[122] On the other hand, in blend films, the nanotubes are insulated from each other by the matrix, and the photoeffect dominates the infrared photoresponse of the device, resulting in a photoconductivity that is largely independent of temperature.[137] Besides, a local enhancement of the electric field at the CNT-insulating polymer interface may increase exciton splitting efficiencies, leading to activated tunneling through the polymer.[137] This effect was additionally discussed as further mechanisms for photoconductivity in composites with an insulating matrix.[138] Furthermore, by comparison of carbon nanotubes grown with different techniques, a high purity of semiconducting SWCNTs with a low content of metallic nanotubes was found to significantly increase the photoeffect.[138]

A very effective approach to separate excitons in carbon nanotube devices and increase the detectivity is the implementation of type II heterojunctions with semiconducting polymers.[139–142] Using a semiconducting polymer with an appropriate LUMO can form a donor-acceptor system, where the SWCNTs act as acceptor due to its higher electron affinity.[139] The energetic offset then provides the driving force to split the bound excitons. The exciton binding energy is relatively high (0.5 eV) in CNTs due to enhanced Coulomb interaction in quasi-1D materials.[143] A photocapacitor measurement technique that is insensitive to thermal effects was utilized by Bindl et al. to investigate exciton dissociation in composites with a variety of polymers.[140] For poly(3-hexylthiophene-2,5-diyl) (P3HT) and poly(3-octylthiophene-2,5-diyl) (P3OT), the effective exciton dissociation at the interface with SWCNTs has been observed, while poly[2-methoxy-5-(3′,7′-dimethyloctyloxy)-1,4-phenylenevinylene] (MDMO-PPV), polycarbonate and poly(9,9-dialkylfluorene) (PFO) show band offsets insufficient for exciton dissociation by charge transfer to the SWCNT.[140,144]

Detailed studies on the SWCNT-P3HT system, performed by Lu et al., highlight the importance of using sorted semiconducting SWCNTs to avoid exciton quenching by charge transfer from metallic nanotubes into the highest occupied molecular orbital of P3HT.[139,145] Ultrafast spectroscopic studies on systems with a single molecular P3HT layer around SWCNTs shows an electron transfer to a nanotube within 400 femtoseconds, forming a charge transfer complex across the interface.[145] Free charge carriers are formed upon the introduction of excess P3HT that allows hole transport away from the interface.[146] In such experiments, an individual wrapping of the SWCNTs with P3HT before forming a bulk heterojunction is important to prevent bundling of the nanotubes that leads to unfavorable morphologies.[147] Applying those design principles, devices with a detectivity of 2.3×10^8 Jones are achieved in uncooled SWCNT/P3HT detectors, exceeding the performance of pristine nanotube films by two orders of magnitude.[139]

A novel approach to further improve the performance of CNT-polymer photodetectors was presented by Hou et al.[148] Well-defined chains of P3HT were successfully grown on the surface of MWCNTs via surface-initiated Kumada catalyst-transfer polycondensation. By controlling the chain length, the formation of highly ordered P3HT aggregates on large diameter

© 2016 WILEY-VCH Verlag GmbH & Co. KGaA, Weinheim

MWCNTs was achieved. While other approaches of CNT functionalization result in amorphous P3HT, polymer aggregation by surface-initiated polycondensation could be observed by a clear red shift (indicator for crystallinity) of the optical absorption. Furthermore, the polymer aggregation causes a shift of the highest occupied molecular orbital, leading to an energetic driving force away from the interface into the aggregates.[149] Theoretical calculations estimated an energetic offset of 0.5 V between the sheet-like P3HT at the nanowire interface and the aggregated P3HT in the bulk phase.[149] These considerations explain the findings of Stranks et al. who observed the free carrier formation only in the presence of pristine and aggregated P3HT domains next to the P3HT-wrapped SWCNTs.[146]

To avoid metallic carbon nanotubes that can severely limit the performance of SWCNT photodetectors, highly selective dispersion of carbon nanotubes using aromatic polymers like PFO were used to obtain nanotubes of a single chirality in high purity.[139,145,150] While this high purity is very desirable, the polymer PFO forms a type I heterojunction with the carbon nanotubes. Hence, no free charge carriers were formed. However, the energy transfer from the polymer to carbon nanotubes was observed by time-resolved photoluminescence spectroscopy.[151] In order to obtain charge separation but still benefit from the highly selective sorting process with PFO, a polymer exchange method was presented by Stranks et al.[152] After CNTs of one chirality were purified using PFO, P3HT that binds more strongly to the carbon nanotubes was added to start a polymer exchange process under ultrasonication. Interestingly, the weak bonding of PFO results in its high selectivity as it only binds sufficiently to the SWCNTs of one chirality. P3HT, on the other hand, binds strongly to all tubes with less selectivity. Using a second semiconducting polymer like poly(9,9-dioctylfluorene-alt-benzothiadiazole) (F8BT) further allows the formation of multilayer coaxial nanostructures that enable direct control of charge transfer processes.[152]

Despite recent progress for SWCNT-polymer photodetectors, the mobilities of such devices as well as the effective exciton diffusion length in CNT heterojunctions are still far below the limits of the carbon nanotubes themselves.[153,154] One hope is that with optimized device morphology or maybe highly ordered arrays of SWCNTs, it will be possible to exploit the exceptionally high exciton diffusion length and charge carrier mobility in individual nanotubes and improve future detector performance.[155]

5. Two-Dimensional Graphene for Photodetection

A single layer of sp^2 hybridized carbon atoms, connected and arranged in a honeycomb lattice structure, similar to multiple, attached benzene rings, was first identified as the building block for layered graphite crystals. The theoretic frame work for the electronic structure of a 2D single layer graphite crystal was pioneered by Wallace in 1947, even before the first TEM study and observation of graphene was reported by Boehm and Hofmann and in 1962.[156,157] The actual name graphene was given again by Boehm et al. in 1986.[158] Nevertheless the scientific breakthrough of graphene has been achieved by Novoselov and Geim who introduced the first mono-layer graphene preparation by mechanical exfoliation and thereby made it accessible for experimentation in 2004.[32] In combination with the observation of an ambipolar field effect in graphene, their work encouraged a new field of scientific explorations reaching from fundamental studies of 2D electron gas systems over potential opto-electronic applications. For these achievements, they were awarded in 2010 with the Nobel Prize in Physics.

The sublattice of graphene can be considered as a benzene ring, in which the p_z-electrons form π-bonds between the sp^2 carbon atoms and additionally experience a unique degeneration due to the lattice symmetry. In the Brillouin zone, this degeneration leads to a linear dispersion of the conduction and valence states at the K and K′ points. In other words, the conduction and valence band meet at the Dirac point, which is why graphene is a zero-bandgap semiconductor or semimetal.[159] The band diagram of graphene is often illustrated by a planar representation of the Dirac cone close to the Dirac point as shown in **Figure 14**a. Graphene is mostly found with an intrinsic p-type character due to atmospheric adsorbates, through which the Fermi level is shifted slightly under the Dirac point at −4.5 eV below the vacuum level, as illustrated in Figure 14a.[160] With respect to the application of graphene in photodetectors, the electrical and optical properties are crucial and will be shortly addressed in the following.

The gapless electronic structure of 2D graphene crystal also determines the optical absorption. Two mechanisms must be differentiated. At first, interband transitions, that is when an electron is excited from the valence band into the conduction

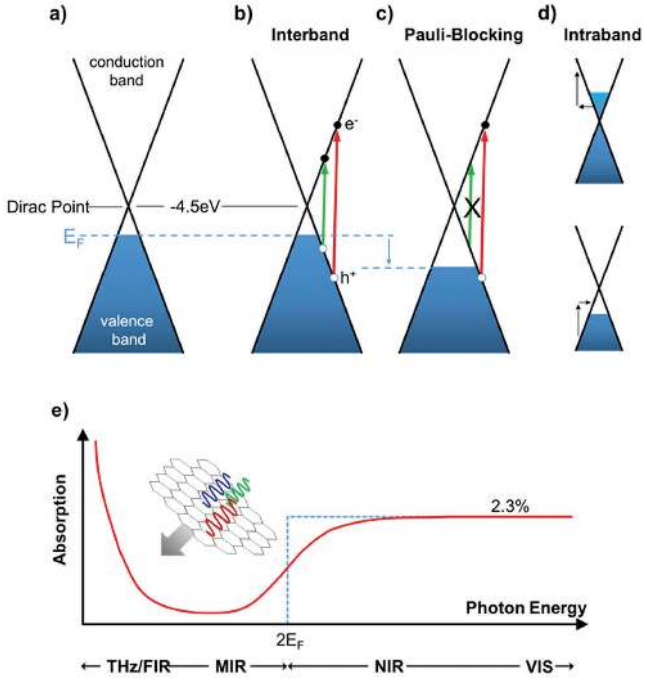

Figure 14. a–d) Show the energy diagram of graphene with its characteristic linear band dispersion around the Dirac point. Depending on the Fermi level interband transitions upon light absorption are allowed or Pauli-blocked. Intraband transitions are only facilitated over scattering processes of hot carriers. e) Shows an absorption scheme for a single-layer graphene across the relevant electromagnetic spectrum. Adapted with permission.[161] Copyright 2014, American Chemical Society.

© 2016 WILEY-VCH Verlag GmbH & Co. KGaA, Weinheim

band (as depicted in Figure 14b), determine the absorption of graphene within the range of 0.5 eV–3 eV (corresponding to wavelengths of 2.5 µm–400 nm). Attributed to the linear dispersion relation, the absorption behaves nearly constant across the mentioned spectral range and could be described in terms of the fine structure constant α, which describes the coupling between light and relativistic electrons. The correlation is established according to Equation (13) over the universal dynamic conductivity Φ for Dirac fermions which is equal to $\alpha c/4$, where α can be expressed as $q^2/\hbar c$, and q stands for the elementary charge, $\hbar$ for the reduced Planck constant and c for the speed of light.[162]

$$T \equiv \left(1+\frac{2\pi\Phi}{c}\right)^{-2} = \left(1+\frac{\pi}{2}\alpha\right)^{-2} \tag{13}$$

Thereby the absorption of an atomic thin layer of graphene is defined over the transmission T according to $1\text{-}T^2 \approx \pi\alpha$, which correlates with the experimentally determined, wavelength independent, constant light absorption of 2.3%.[162] This number is very impressive for a single layer of atoms and renders graphene an exceptional broadband absorber. Nevertheless, for longer wavelengths, the absorption decreases and deviates from the universal value. The deviation is caused by the unintentional doping effects which shift the Fermi level. Thereby optical transitions with photon energies smaller than $2|E_F|$ are not allowed anymore, due to the so-called Pauli-blocking.[163] The band diagram at Figure 14c illustrates this effect representative for a p-doped graphene. Since graphene is susceptible to electrostatic doping, an external gate field can be used to shift the Fermi level up to several hundred meV. Using an electrolyte with high breakdown voltage like ionic liquids, the carrier density can reach 10^{14} cm^{-2} which allows the modulation of the graphene absorption in the VIS range.[163] The mechanism behind the FIR absorption ($E_{Photon} < 2|E_F|$) in graphene is mediated by intraband optical transitions of free electrons. Since the Fermi velocity of free charge carriers in graphene is only a fraction of the speed of light, direct absorption of photons is not allowed due to the required momentum conservation. Additional scattering with phonons or defects is necessary for an intraband excited optical response, as depicted in Figure 14d. Intraband absorption is affected by the charge carrier density (i.e., the number of occupied states). Therefore, low energy photon absorption scales with the Fermi level very closely. The simplest description of an intraband absorption is found in the Drude model for frequency-dependent sheet conductivity.[163,164] Similarly, the excitation of plasmons in graphene, which are collective oscillating free electrons, cannot be facilitated directly due to the momentum mismatch. Nevertheless, plasmon excitation in the THz regime becomes accessible when the graphene is patterned into features approaching the size of the wavelength.[41,161]

For a better comprehension, the complete broadband absorption of a single graphene layer is schematically illustrated in Figure 14e. In VIS and NIR region of the spectrum, the optical conductivity limits the absorption, thus leads to interband optical transitions. Depending on the doping level this absorption behavior is dominant for photon energies larger than $2|E_F|$. At $2|E_F|$, a thermal smearing mediates the transition from interband to intraband optical transitions. The absorption then undergoes a minimum in the MIR region where disorder takes influence on the momentum for optical transitions and increases again for intraband absorption of small energy photons in the FIR/THz regime.[161,165,166]

The charge carrier lifetime after photoexcitation in a single layer graphene is governed by electron-electron and electron-phonon scatter processes. Loss mechanisms like thermalization and Auger recombination take place on a ps time scale.[167–171] As a matter of the linear dispersion relation of the band structure in graphene, electrons can be considered Dirac fermions with a vanishing effective mass. Hence, the Fermi velocity is as high as 10^6 m s^{-1}, and even under ambient conditions, very high charge carrier mobilities $\mu_{e/h}$ of up to 20×10^3 cm^2 V^{-1} s^{-1} for electrons and holes can be achieved with a theoretical limit at $\approx 10^5$ cm^2 V^{-1} s^{-1}.[32,159,172–174] Therefore a moderate electric field is mostly sufficient for a photocurrent extraction and allows the operation of graphene photodetectors up to an intrinsic bandwidth of 262 GHz with almost 40 % internal quantum efficiency.[51]

The aforementioned set of properties of graphene makes it uniquely interesting for complementary use in opto-electronic applications. The high transmission and electrical conductivity make atomically thin graphene layers extremely promising as future transparent electrode material, replacing the industry standard ITO and competing with polymeric (e.g., PEDOT:PSS[175]) and silver nanowire based electrodes[176] for ridged and flexible device designs. Organic and inorganic LEDs, solar cells and detectors incorporating a graphene electrode have already been demonstrated.[177] Remaining challenges lie within large area fabrication of defect-free graphene layers. On the other hand, when incorporating graphene as absorber medium in photodetectors, its unique 2D nature enables the use of various physical effects in order to gain a photoresponse. Detection mechanisms based on photonic electro-hole generation, thermal effects or plasmonic resonances can be exploited. Each of those mechanisms offers individual advantages during the tuning and adapting the photoresponse of the detector. In this chapter, we introduce and elaborate reported graphene detectors with different device architectures and working principles, which includes high performance photodetectors for room-temperature applications in broadband detection, digital communication and FIR/THz technologies.[161,178–180]

5.1. Graphene Single-Layer Based Photodetectors

Graphene has a broad but very low absolute absorption in monolayers. Ultimately this limits the responsivity of single-layer graphene devices. Hence, it is a straight forward approach to increase the absorption in graphene by using few-layer graphene stacks as absorber medium. Due to the additive absorption per layer, less light for detection would be lost to transmission.[162] Despite the benefit of increased absorption, to the best of our knowledge, there is not any multilayer photodetector which could outperform single-layer (SLG) or bi-layer (BLG) graphene devices.[181,182] Therefore, we focus on various SLG/BLG photodetectors, emphasizing the detector principles as a whole.

© 2016 WILEY-VCH Verlag GmbH & Co. KGaA, Weinheim

Yet, Kang and co-worker showed another possibility to increase the absorption in a single-layer graphene.[183] The layer itself was grown via CVD process and subsequently, transferred on a stretchable acrylic substrate which was 350% prestrained along the x-axis and 250% along the y-axis. Relaxing the substrate led to crumpling of the graphene layer with a texture of various feature heights (100 nm–500 nm) and operation over a wavelength range from 100 nm to 800 nm. The effective surface area increased by over 200%, and compared to a flat graphene, the light extinction of the crumpled graphene layer increased by a factor of 12 (measured in the range of 350 nm–700 nm). However, since the light scattering by the crumpled graphene increased concurrently by a factor of ≈3.2, the effective improvement of absorption per unit area due to the texturing remained around 3.7 fold. The latter also coincides with the enhanced photocurrent in the prototype-photodetector, with simply two gold contacts on the crumpled graphene layer. The photoresponse remained stable for simple bending of the substrate and lost about 50% in signal strength upon a 200% stretch. When a small voltage bias was applied to the graphene photodetector, the responsivity was estimated at 405 nm (20 mW) to be ≈0.11 mA W^{-1} and the response time with ≈270 ms. Eventually, the concept demonstrates one way to enhance the photoabsorption and responsivity in SLG based detectors, whether rigid or stretchable.[183]

More commonly though, graphene photodetectors are prepared from flat graphene flakes of several μm in size, spread on a Si/SiO_2 substrate. The Si substrate is often heavily doped and used as back-gate in a field-effect transistor (FET) configuration. The graphene itself is contacted by metal contacts, applied via e-beam lithography. In the area below metal contacts, the Fermi level of graphene is pinned. However, due to the metal work function being below or above −4.5 eV, graphene becomes p- or n-type, respectively. The doped regions extends by around 100–200 nm into the metal-free graphene channel and thus, the Fermi level is gradually restored to its original value. The "intrinsic" Fermi level in graphene can be additionally controlled by a back-gate voltage. Therefore, it is possible to influence the doping nature under the metal contact, thus create pn-, nn^+- or pp^+-junctions.[184–187] By inducing a pn-junction in the graphene, the internal electrical field can be used to separate charge carriers in absence of an external bias. This greatly improves the photoresponse, since virtually no dark current is present.

In order to benefit from this effect, Mueller et al. placed a BLG on a Si/SiO_2 substrate and applied two narrow interdigitated finger electrodes on top to increase the nearby electrode area.[20] They chose the electrode distance to be as small as 1 μm to allow the internal field at the contacts to bridge most of the distance and to harvest a photocurrent throughout the channels. A schematic of the device architecture is illustrated in **Figure 15**a. Both metal electrodes were chosen asymmetric in order to break the mirror symmetry of the junction profile and ensure a net photocurrent. Pd and Ti were used, where former causes stronger p-type doping than the latter. The corresponding zero bias band diagram is depicted in Figure 15b. It was found that at a gate voltage of −15 V, the photocurrent polarity across the graphene/metal junctions would flip and thereby allowing the current flow in the same direction. Without

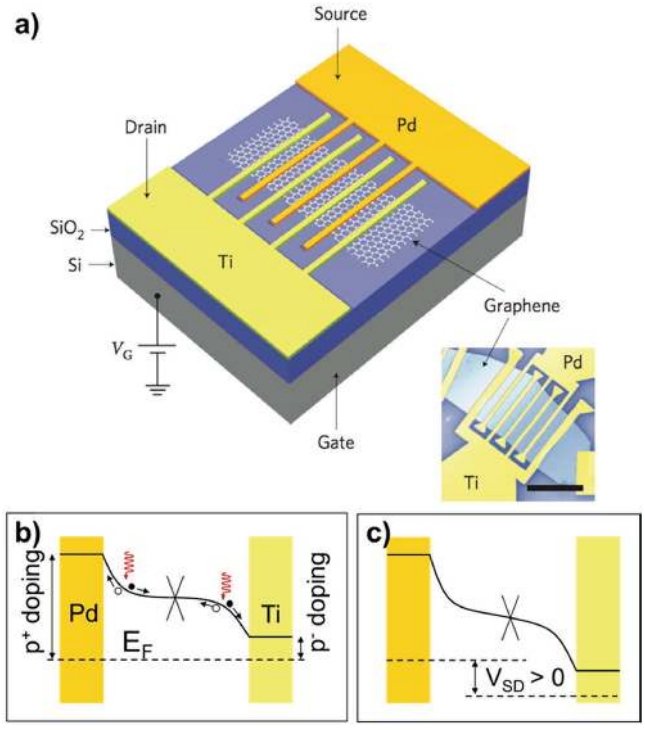

Figure 15. a) Shows a metal–graphene–metal photodetector. The SLG is contacted with asymmetric, interdigitating metal contacts. The inset shows an colored SEM micrograph of the actual device (scale: 5 mm). The band diagram of the detector is depicted at b) and c), without and with external bias, respectively (adapted from ref. [20,179]). Reproduced with permission.[20,179] Copyright 2010 and 2014, Macmillan Publishers Ltd.

any source-drain bias (V_{SD}), the detectors showed a linear photoresponse for 1.55 μm MIR irradiation up to an illumination power of 10 mW. The responsivity reached 1.5 mA W^{-1}. In theory, VIS light should have led to a comparable response, however it was not presented by the authors. In terms of the response speed, the detector was able to follow a 16 GHz signal at its −3 dB limit and was used for an error-free data transmission at a rate of 10 Gbit s^{-1}. Compared to previous reports of a 40 GHz bandwidth[188] in a similar detector, the bandwidth was sacrificed by the large device area, which on the other hand brought the improved responsivity. By applying a positive source drain voltage to improve the carrier extraction (see band diagram in Figure 15c), the responsivity was increased even further to 6.1 mA W^{-1}, though it was limited by the increasing ohmic dark current.[20] An increasing photocurrent with applied bias is a common indicator for a photovoltaic current being generated and extracted from the photodetector. Later, however, the intrinsic photogeneration of hot carriers in graphene has been proven.[186] This greatly supported the assumption of a photocurrent being generated by a PTE effect as well.[189] Basically the PTE effect establishes a photovoltage V_{PTE} across a pn-junction by light-induced heating, which also leads to a charge carrier drift and separation, respectively, similar to the PV current. Both current types have the same polarity which is why they cannot be explicitly distinguished in many device configurations.[160] Experimentally, the PTE current can be isolated in pp+ or nn+ junctions where it changes the polarity due to a

© 2016 WILEY-VCH Verlag GmbH & Co. KGaA, Weinheim

change in the transconductance.[186] However, to the best of our knowledge, there is not any device reported so far, which exclusively utilized the PV current for photodetection.

Within this concept, Cai et al. presented later a THz graphene photodetector using a very similar device architecture like Mueller et al., and demonstrated the PTE effect as the driving force, by comparing the photoresponse of light induced heating with joule heating.[42] They prepared metal stripes of Cr and Au as contacts on an exfoliated SLG which was placed on a Si/SiO_2 substrate. The channel width was set to 3 μm in order to remain below the electron diffusion length.[190] Due to the different metal work functions, the graphene close to the contacts was p- and n-doped differently with an associated asymmetric shift in the Fermi level. Concurrently, the Seebeck coefficients of each half of the graphene channel were altered and of opposite sign. The Seebeck coefficient S can be related to the conductivity σ and charge carrier density according to Mott's formula:

$$S = -\frac{\pi^2 k_B^2 T}{3q}\frac{1}{\sigma}\frac{d\sigma}{d\mu_C} \tag{14}$$

where k_B stands for the Boltzmann constant, T for the absolute temperature, q for the elementary charge and μ_C for the chemical potential of the majority carrier. When the pn-junction is heated in the middle of the graphene channel a decaying temperature profile ΔT towards the contacts builds up a photovoltage response V_{PTE} according to:

$$V_{PTE} = (S_n - S_p)\Delta T \tag{15}$$

In the aforementioned device, the highest photoresponse was recorded close to the charge neutrality point for a minor, gate voltage-induced, p-type doping. Considering the impinging light power (17 mW) of the 2.52 THz (119 μm) beam, the responsivity was as high as 10 V W^{-1}. Despite being one of the highest reported responsivities for room-temperature operated graphene THz detectors so far, the absolute THz absorption in the SLG channel was low. It was suggested to improve the absolute THz absorption by means of multilayer graphene, antennae or structure-wise tailored plasmonic resonances. Anyhow, in order to estimate the potential of a SLG, the responsivity was also determined with respect to the absorbed illumination power which makes it more representative for the intrinsic material properties. Thus, an impressive peak value of 715 V W^{-1} was obtained. The theoretical maximum for a SLG on SiO_2 was derived to be in the order of 10^5 V W^{-1}. Additionally, the NEP was determined as low as 16 pW $Hz^{-1/2}$, which is comparable with other room-temperature-operated THz detectors.[191] The electrical response time was recorded with 110 ps.[42] Especially for thermal detectors such a detection speed is outstanding, and in case of graphene, it originates from intrinsic ultrafast hot carrier generation upon light excitation. The generation of hot electrons takes place within several fs. In the hot state, electron-electron scattering dominates photocarrier equilibration at an elevated electron temperature T_e.[190] Eventually, in steady state conditions, the photo-induced hot carrier density (of carriers which can be extracted by an internal or external field) depends on T_e. Total relaxation of hot electrons is facilitated over scattering processes with acoustic phonons, increasing the phonon temperature and ultimately the lattice temperature of graphene. The interaction with phonons is an inefficient decay route. Therefore, it is possible for the electron temperature to remain high for a few ps, enabling a fast photoresponse before complete thermalization.[169,189]

In order to increase the active area of a pn-junction to maximize the photoresponse, an application of a vertical pn-junction was demonstrated by Kim et al. via chemically doped, overlapping SLG, contacted by two silver electrodes.[43,192] However, the applied dopants benzyl viologen and $AuCl_3$ remained at the surface of each graphene layer establishing a thin tunnel barrier between the graphene layers. Hence, the device was best modeled by a metal-insulator-metal diode instead of by a thermocouple. The dark current under forward bias was suppressed due to a reduced number of joint states between both graphene layers. Under illumination, hot holes, rather than electrons, could tunnel the barrier and contribute to a photocurrent. In **Figure 16**, the bias dependent responsivity and specific detectivity are plotted for the visible spectrum. The responsivity was highest at 900 nm with 0.7 A W^{-1} at 6 V. The detectivity on the other hand peaked at 1.0×10^{12} Jones at 900 nm under a bias of 2 V, which coincides with the highest on/off ratio of the device. Under various illumination power, the detector showed a linear dynamic range of 90 dB from 10 nW cm^{-2} to 100 μW cm^{-2} with a roll-off at higher intensities due to increased charge carrier recombination. The −3 dB cut-off frequency was determined at 30 kHz and considered to be limited by the tunneling time through the barrier and residual trap states at p- and n-graphene interlayer.[43]

A similar detector principle was applied by Liu and co-workers by introducing a graphene double-layered heterostructure for broadband photodetection. The absorption properties of one graphene layer was additionally utilized to act as a photo-gate on the graphene FET channel.[44] For that, they built a graphene transistor on a Si/SiO_2 substrate, where the exposed graphene channel was subsequently covered by a 5-nm thin Ta_2O_5 tunnel barrier and then covered by a second CVD grown graphene layer. In this layer configuration, it was found that the top graphene layer was slightly more p-doped and had a 0.12 eV lower Fermi energy than the bottom graphene. In order to equilibrate the Fermi level, the energy band of the tunnel barrier was slightly tilted, leading to a thinning of the tunnel barrier for photo excited hot electrons in the top graphene layer. Under operation the top graphene was used as an electrical floating absorber which injects hot electrons through the tunnel barrier into the bottom graphene channel, where the change in conductance was monitored. Photo excited holes remained in the top graphene layer, accumulated, and in combination with the high interlayer dielectric capacitance led to a strong photo-gating effect on the bottom graphene channel. A strong negative shift of the Dirac point, increasing with illumination power, supports the suggested mechanism. The device responsivity was determined for a wavelength of 532 nm and found to increase from 8 to >1000 A W^{-1} with decreasing excitation power from 0.1 μW to 1 nW and a NEP of 1×10^{-11} W $Hz^{-1/2}$. The device electrical bandwidth seemed to have an upper limit of 1 kHz and ought to improve with

© 2016 WILEY-VCH Verlag GmbH & Co. KGaA, Weinheim

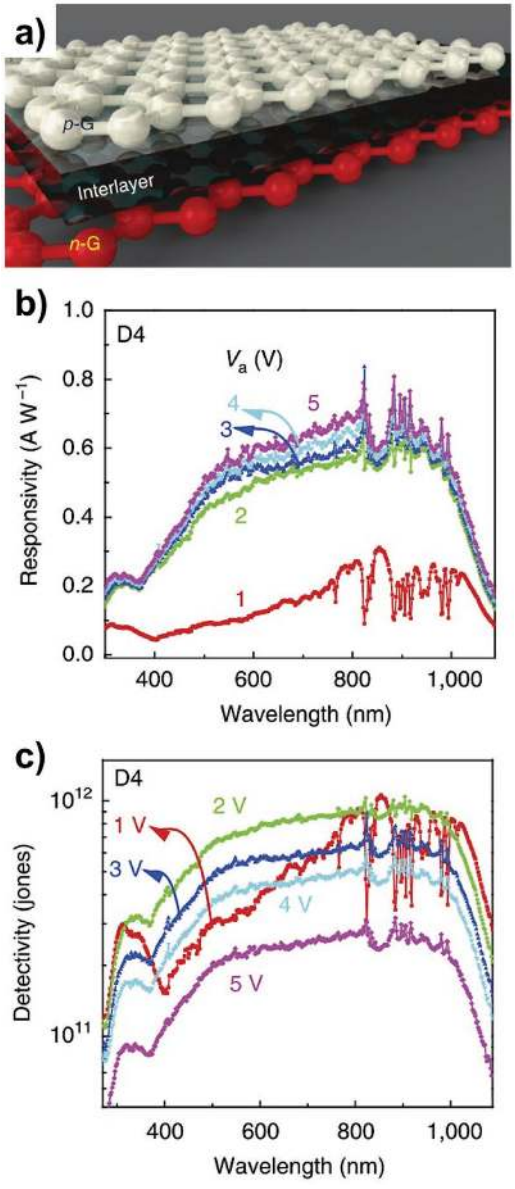

Figure 16. a) An illustration of a vertical pn-junction of two chemically-doped graphene layers. The residual dopants act as interlayer. Latter was found to act as tunneling barrier in the photodiode detector build by Kim et al. The spectrally resolved responsivity and specific detectivity are plotted in b) and c), respectively. Reproduced with permission.[43] Copyright 2014, Macmillan Publishers Ltd.

the quality of the dielectric and the tunneling rate of the hot carriers. The authors also demonstrated a detector device with Si as tunnel barrier instead which reached responsivities of 4 AW^{-1} at 1.3 μm, 1.9 AW^{-1} at 2.1 μm and 1.1 AW^{-1} at 3.2 μm.[44] Utilizing other two-dimensional semiconductors such as transition metal chalcogenides as tunneling barrier layer may lead to even better broadband, room temperature operated, photo-gated graphene-based detectors.

So far, graphene detectors were presented with responsivities in the VIS, NIR and FIR/THz parts of the electromagnetic spectrum. As mentioned earlier, the intrinsic absorption of graphene in the MIR part, without any metallic or semiconducting sensitization, is weak and observed up to 6 μm.[20] A strategy on how this gap can be bridged with graphene only, was demonstrated by Freitag et al.[41] They showed how periodically patterned graphene can be used to couple MIR and THz radiation with intrinsic plasmons in graphene at room temperature (not to be mistaken with the plasmonic resonances in antennae-coupled graphene detectors). Graphene was structured into nanoribbons with a sub-wavelength feature size. A representative TEM image of 100 nm wide graphene nanoribbons prepared by e-beam lithography is shown in the inset of **Figure 17**a. In order to excite the graphene plasmon, the wave vector and energy of the plasmon and the incoming radiation needed to match. Theoretically, this means a collective electron density oscillation (plasmon) excitation can be effectively accomplished, only when the electric field vector of incident light is oriented perpendicular to the graphene nanoribbons, and the Fermi level of graphene is gate modulated to coincide with the energy of the impinging light. Since an excited graphene plasmon strongly interacts with the surface polar phonons of the underlying substrate (in this case SiO_2 of the Si/SiO_2 substrate), this forms long lived hybrid plasmon-phonon modes with narrow spectral width of resonance. The spectral resonance frequency can be tuned by the applied gate voltage at the Si back contact. Subsequently, such hybrid plasmon-phonon quasi-particles decay by inelastic scattering at the graphene edges into a hot electron-hole pairs and SiO_2 surface polar phonons. The latter thermalizes with other phonons while increasing the overall phonon (graphene lattice) temperature, which promotes further electron-phonon scattering and reduces the electric conductivity. On the other hand, the hot electrons thermalize among themselves increasing the electron temperature which is equivalent to an increased carrier density and, subsequently, conductivity. Hot electron-hole pairs are predominantly excited for a light being polarized in parallel (p-pol) to the graphene nanoribbons, whereas plasmon excitation is higher for perpendicular polarized (s-pol) light.

For graphene nanoribbons with 140 nm in width, the parallel polarized illumination led to a 15-fold enhanced plasmon induced photocurrent response (Figure 17). A peak responsivity of −7.5 μA W^{-1} could be determined under polarized MIR irradiation of 10.6 μm wavelength and a power density of 20 kW cm^{-2}. It slightly exceeded the photoresponse of a non-patterned graphene reference device as shown in Figure 17b. The photocurrent, (Figure 17c), increased for negative gate voltages due to the reduction of strong intrinsic p-type doping (V_{Dirac} = 52 V). The current response showed a linear behavior with respect to the applied drain voltage, however, it saturated due to joule heating, limiting the maximum responsivity. By reducing the feature size of graphene nanoribbons even further, a gate voltage-dependent switch of the photocurrent polarity upon parallel or perpendicular illumination could be observed. Eventually Freitag et al. presented the possibility of tuning the intrinsic photoresponse of graphene into the MIR absorption gap by harvesting, polarization sensitive, photons via coupling to plasmon-phonon resonances.[41] For the optimization of the device architecture, the grating structure of graphene and low-temperature operation

© 2016 WILEY-VCH Verlag GmbH & Co. KGaA, Weinheim

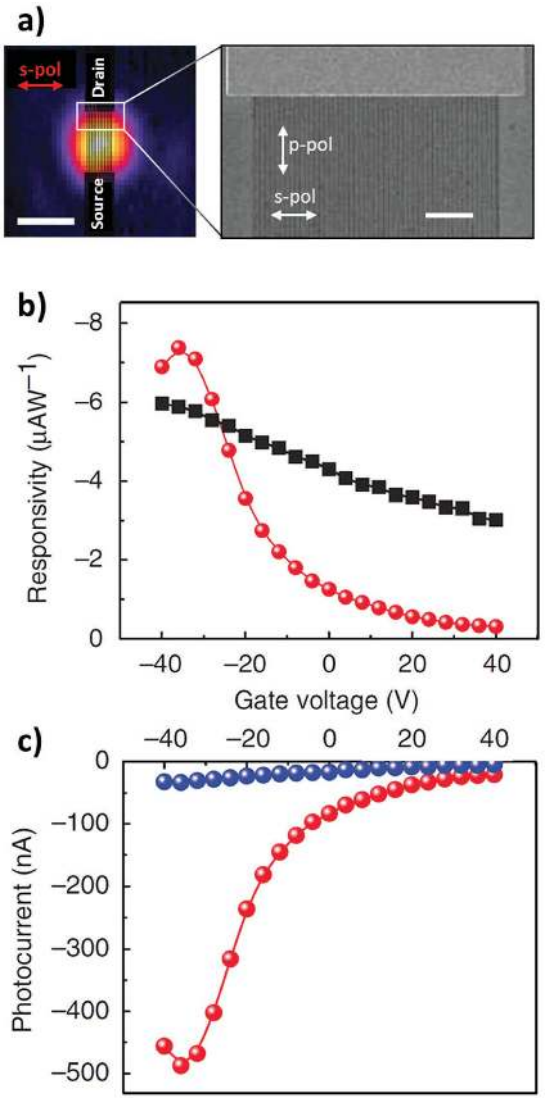

Figure 17. a) The photocurrent scan of the graphene nanoribbon two terminal detector which showed a plasmonic photoresponse to perpendicular polarized (s-pol) MIR radiation (scale bar: 30μm). The inset in a) shows a SEM micrograph of the as prepared graphene microribbons with a width of 100 nm. b) Under s-pol light and at a high, negative gate bias the detector responsivity (red spheres) exceeded the responsivity of an unstructured graphene detector (black squares). c) The photocurrent induced by plasmon-phonon excitation in the nanoribbons under s-pol light (red-spheres) is much larger for higher electrostatic doping then for parallel polarized light (p-pol, blue spheres). Reproduced with permission.[41] Copyright 2013, Macmillan Publishers Ltd.

are promising approaches to further tailored and improve MIR to THz absorption in pure graphene photodetectors.

The presented photodetectors above are all incorporating a SLG or BLG as opto-electric active medium. Independent on the mechanism behind the photocurrent generation, all detectors relied solely on the intrinsic absorption properties of graphene. It was demonstrated how graphene can be effectively utilized in various detector types for a spectral detection stretching from VIS to FIR/THz.

5.2. Graphene Bandgap Engineering for a Larger Photoresponse

Another possibility to increase the inherent absorption in graphene is to introduce a bandgap in graphene and thereby to improve the internal quantum efficiency for direct electron-hole pair generation under illumination. Yin et al. have adopted this concept in an interesting approach of twisted bi-layer graphene (tBLG) stacks.[193] Theoretical studies show that the Dirac band dispersion changes dramatically when two graphene layers are stacked, and one of them is rotated by an angle with respect to the other.[194–197] Unlike for AB stacked graphene, the band structure in tBLG opens a bandgap while remaining linear near the Dirac point. Hence, some properties unique to SLG remain preserved. **Figure 18**a shows two stacked graphene 2D crystals twisted by an angle θ. Right next to it the schematic illustration shows two intersecting Dirac cones of the individual monolayers. They form a saddle point in the reciprocal space which in turn leads to the formation of van Hove singularities in the density of states with energies of E_{VHS}. Photons with an energy of $2E_{VHS}$ will be able to excite electron across this sub-band, similar to CNTs, and generate a photocurrent. Plotted in Figure 18b is the almost linear dependence of E_{VHS} on an increasing twisting angle from 5° to 30° which is equivalent to bandgap absorption in a wavelength range from ≈2.5 μm to ≈280 nm. For the demonstration of an enhanced photocurrent, Yin and co-workers grew tBLG on copper foil via a CVD process. The twisting angle was determined by TEM and Raman spectroscopy. Two tBLGs with θ = 7° (Device A) and 13° (Device B) were selected and embedded into a two-terminal device as illustrated at Figure 18c. Under illumination by a 532 nm (2.33 eV) laser, the 13° tBLG showed a 6.6 times higher photocurrent in the IV curve (Figure 18d). This very well agrees with the energy interval of the van Hove singularities of $2E_{VHS}$ = 2.34 eV and proves a selectively enhanced light interaction with the bi-layer graphene. Figure 18e shows additionally how the photocurrent exhibits a distinct maximum for photon energies matching the van Hove interval for a device with an angular twist of 10.5° and 13°, respectively. For Device B under 532 nm excitation, a linear photocurrent response could be observed, and the responsivity reached up to 1 mA W^{-1} for power densities reaching from 1 μW to 100 mW. In combination with the large area fabrication methods for structured graphene, tBLG structures might find future application in graphene based e.g., multicolor detection.[198]

5.3. Graphene Heterojunction and Plasmon Enhanced Photodetection

In the literature, many hybrid detector designs can be found at which graphene is used in combination with inorganic semiconductors, waveguides or metallic antennae to exploit the intrinsic properties even more. Introducing all devices and concepts in detail exceeds the scope of our review. Nevertheless, hereafter we provide an overview about very promising graphene hybrid photodetector concepts. For a more comprehensive insight on the interaction and formation of graphene-inorganic hybrid junction we direct the interested reader to the review by Gao and Fang.[199]

© 2016 WILEY-VCH Verlag GmbH & Co. KGaA, Weinheim

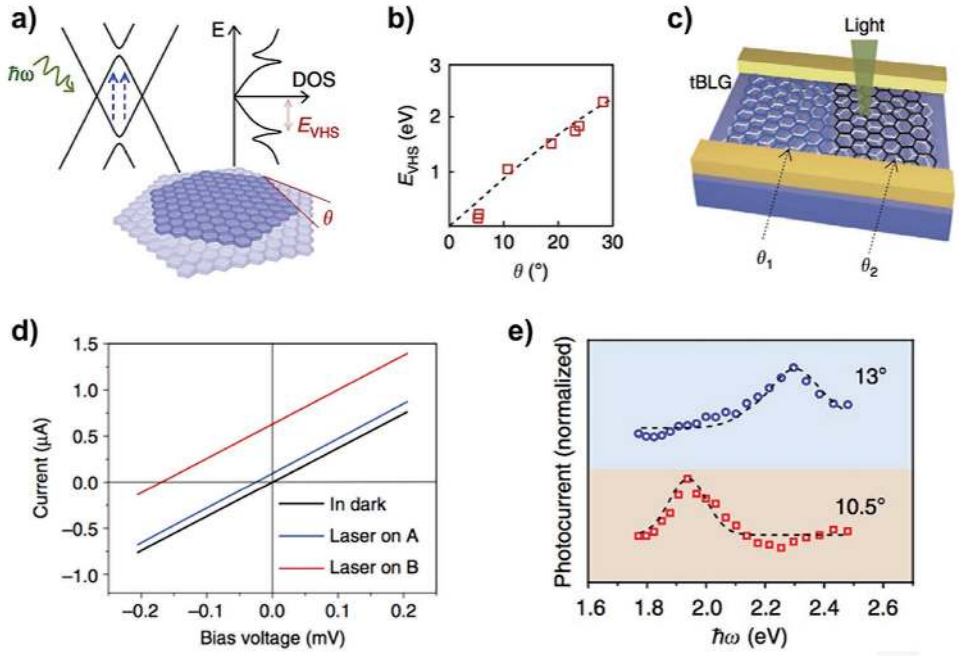

Figure 18. a) An illustration of two stack graphene crystals twisted by an angle θ. The angular offset lets the Dirac cones of carbon atoms of each graphene layer overlap, leading to the formation of a bandgap in the reciprocal space as indicated by dashed arrows. As a result, van Hove singularities are a formed in the density of states. b) The energy of the van Hove singularities scales almost linear with the twist angle. c) An illustration of a simple two terminal device with two graphene stacks with different twist angles embedded. In case the opened sub-bandgap matches the energy of the incident light (Device B), the photocurrent increases significantly as seen in the IV curve at d) and in form of peaks in the normalized current during a spectral scan at e). Adapted with permission.[193], published under the CC-BY license.

Nonetheless, since the absorption of graphene was used complementary to an inorganic semiconductor, the graphene hybrid detector, demonstrated by Long and co-workers, shall be highlighted in the following. The photodetector was designed as highly sensitive photovoltaic detector with a p-g-n heterojunction.[200] In the photo active layer, a single graphene layer was sandwiched in between two atomically thin layers of WSe_2 and MoS_2 (**Figure 19**a), both of which belonging to the family of transition metal dichalcogenide semiconductors. Two low work function Pd/Au electrodes were applied and led to a p-doping inside the WSe_2, whereas the MoS_2 remained n-type due to Fermi level pinning. Thereby, an atomically thin van der Waals pn-junction was created across the graphene. The IV characteristic of the device revealed a short circuit current, scaling linearly with the illumination power and a constant open circuit voltage of 0.23 V. Considering the atomically thin junction, such photovoltage implies an internal electrical field in the order of 10^6 V cm^{-1}, supporting efficient charge separation. The device responsivity and specific detectivity peaked with 10^4 AW^{-1} and almost 10^{15} Jones at a wavelength of 488 nm, respectively. Behind the large responsivity an electrical gain mechanism was expected, originating from the fast transit times across the junction and the inelastic tunneling process at the stacked interfaces which increased the carrier lifetime due to reduced recombination. Hence, the measured *EQE* approached 10^6%. The high specific detectivity, on the other hand, was encouraged by a very low noise current density in the order of 10^{-14} A $Hz^{-1/2}$, characteristic for detectors in the photovoltaic mode. Towards longer wavelengths, however, the responsivity and detectivity dropped around three orders of magnitude across the VIS spectrum. Beyond 800 nm, the responsivity (detectivity) decreased further from a few AW^{-1} (10^{11} Jones) to only 0.1 AW^{-1} (10^9 Jones), as shown at Figure 19b, until 2400 nm. This behavior is explained by two different charge carrier photo-generation sites. Both semiconducting dichalcogenides WSe2 and MoS2 have each their own bandgap of E_{g1} = 1.88 eV and E_{g2} = 1.65 eV absorbing at 660 nm and 750 nm, respectively. Hence, the responsivity in the VIS spectrum is attributed to the absorption of all three components within the p-g-n junction, and for wavelengths larger than 800 nm, the photon energy is only sufficient to excite interband transitions in the graphene alone. The charge excitation and transport are indicated in the corresponding band diagrams shown at Figure 19c and d. Despite the large photogain in the device, the temporal response showed a rise (fall) time of 54 μs (30 μs) and could follow a 1 kHz modulated signal without signal deterioration. Hence, Long et al. have successfully demonstrated the concept of van der Waals heterojunctions as viable route for broadband graphene based detectors with significant sensitivity.[200]

Within the framework of graphene hybrid photodetectors, another strategy to enhance the intrinsic photoresponse in graphene is to integrate waveguide structures into the detector design. The evanescent wave along the waveguide surface will couple to a graphene layer and excite inter- and intraband optical transitions. This technique is especially interesting for systems on a chip when optical inter- or intrachip communication links need to be established with a very small footprint. With respect

© 2016 WILEY-VCH Verlag GmbH & Co. KGaA, Weinheim

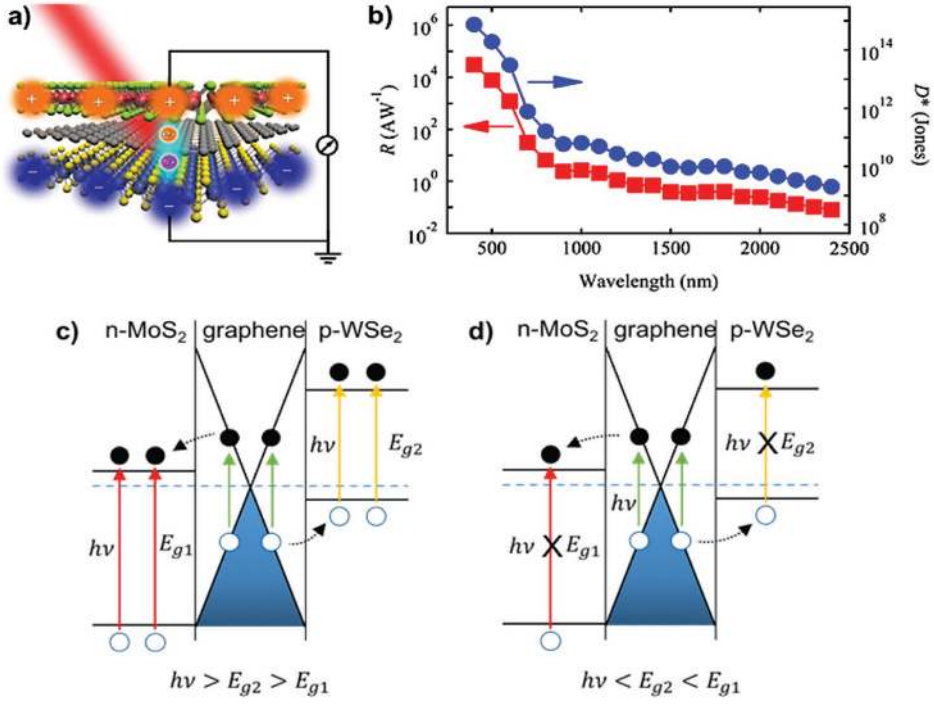

Figure 19. a) An illustration of a van der Waals heterojunction of a single graphene layer stacked in between WSe_2 (top) and MoS_2 (bottom), forming a pn-junction across a single graphene layer. The responsivity and specific detectivity of a device comprising such p-g-n junction is plotted at b). For high energy photons, the electron (full circle) hole (open circle) excitation takes place across the bandgaps of WSe_2, MoS_2 and graphene, as depicted in c). Low energy photons only excite interband transitions inside the graphene layer, as depicted in d). Reproduced with permission.[200] Copyright 2016, American Chemical Society.

to the silicon-based complementary metal-oxide semiconductor (CMOS) technology, the integration of broadband detectors is important, and graphene could help to replace Ge or Si implemented detectors. The possible integration of a Si-waveguide and a graphene photodetector in a CMOS compatible process was demonstrated by the group of Mueller.[45] A lithographically prepared Si-waveguide was covered by graphene and contacted by three metallic terminals. Light coupled into the waveguide was successful detected across all optical communication bands in a wavelength range from 1.3 to 1.65 µm. The photocurrent extraction from the graphene relied on the internal field adjacent to the metal contacts. Hence, the device could be operated without any bias, beneficial for low power consumption. The maximal achieved responsivity was 0.05 A W^{-1}, constant across the optical bandwidth, and the detector could be operated at up to 18 GHz.[45]

Around the same time, Wang et al. demonstrated a slightly different, equally CMOS compatible, detector design comprising a suspended graphene/Si membrane waveguide.[201] The suspension helped to reduce the damping of MIR light by a buried oxide. Hence, in combination with an in-plane absorption geometry of the graphene/Si heterojunction, the detection could be facilitated even at a wavelength of 2.75 µm. Greatly benefiting from the low dark current across the graphene/Si heterojunction, a responsivity at this wavelength of 0.13 A W^{-1} was achieved.[201] For a successful chip integration, an optical modulation is needed as well, and has been already demonstrated in a gate voltage tunable waveguide integrated modulator and photodetector by Youngblood and co-workers.[202]

The responsivity of graphene photodetectors can be also influenced and designed to meet very narrow absorption bandwidths by combining the graphene with plasmonic antennae. Small metallic features or gratings can be used to assist and enhance the photoresponse up to 400% for a designated wavelength.[203] By adapting the plasmonic antenna design, the resonance wavelength can be adjusted from multicolor detection in the VIS spectrum to strongly enhanced MIR detection with a responsivity of 0.4 V W^{-1} at 4.45 µm.[204–206]

Focusing on even longer wavelength from the FIR region, a more selective room-temperature THz detection with graphene can be achieved by utilizing e.g., log-periodic circular-toothed or bowtie metallic antennae, to resonantly couple THz radiation to graphene.[207,208] A responsivity of ≈1 V W^{-1} was already reported for a wavelength of 1 mm (0.292 THz).[208] The underlying detection mechanism is attributed to the collective excitation of the 2D electron gas in graphene, which can act as a cavity for plasma waves, eventually establishing a photovoltage. Inside the resonant regime of the antenna, the photodetection can be achieved much stronger than the photoresponse of the non-resonant graphene broadband signal. A more detailed elaboration of the detection principles and a summary of various THz detectors can be found elsewhere.[161,179,209]

Graphene is additionally utilized in planar semiconductor/graphene heterojunctions, partially to surpass the photoresponse limitation in metal-graphene-metal and graphene-based

© 2016 WILEY-VCH Verlag GmbH & Co. KGaA, Weinheim

FET photodetectors, due to a small photoactive area. Moreover, they rely on the stronger absorption of the inorganic semiconductor part and the electric properties of graphene. In a recent review by Bartolomeo, graphene/semiconductor heterojunction detectors are explained in detail.[210]

6. Three-Dimensional Bulk Carbon for UV and Radiation Detection

Three-dimensional allotropes of carbon include graphite, in which the honeycomb-structured layers of graphene are stacked on each other with a distance between the planes of 0.335 nm,[211] and diamond with either a face centered cubic or a hexagonal lattice structure. Tetragonal arranged covalent bonds with a length of 0.155 nm via sp^3 orbitals cause the cubic diamond to be the hardest naturally occurring material, which shows excellent thermal conductivity and a high dispersion of light. Diamonds are classified by the concentration and type of impurities they contain,[212] and the purest diamonds are of type IIa, which are basically insulators with a band-gap energy of 5.47 eV, and a room temperature mobility of 1800 $cm^2\ V^{-1}\ s^{-1}$. In graphite, in contrast, there is an overlap between the valence and conduction bands, causing a free carrier concentration of $\approx 10^{19}\ cm^{-3}$[213] and due to the layered structure of graphite its mobility is highly anisotropic. As a result, graphite is applicable in photodetecting devices as electrode material only. By drawing electrodes with a soft pencil on flexible paper, extremely low cost photodetectors were presented by Jungang He et al., with colloidal PbS nanocrystals as photoactive layer.[214] These detectors showed an excellent bending robustness and a photoresponse up to the near infrared spectral region.

The large bandgap of diamond together with its concomitantly small intrinsic carrier concentration makes it to an ideal material for applications in UV photodetectors. The basic features of these detectors are seen in photoconductivity spectra, measured in a lateral device geometry, which makes use of interdigitate electrodes with a gap distance between the electrodes of typically 50 to 100 μm. Bias-fields in the order of several tenths of Volts per micrometer are applied to obtain the spectral response, as shown in **Figure 20**a on an energy scale between 5.2 and 6.5 eV.[215] The indirect nature of the diamonds band gap causes three different thresholds in the photoconductivity spectrum of a type IIa diamond[215]: (1) the photoconductivity starts at an energy which is by the transversal optical phonon energy lower than the band gap energy (at 5.257 eV); (2) at the transverse acoustic phonon energy above the band gap a kink is observed (at 5.483 eV); and (3), at the transversal optical phonon energy above the band gap the steepest increase of the spectrum starts. Interestingly, a completely different spectral shape is observed, when the photoconductivity is measured in vertical direction, in between a top contact and a bottom contact on the specimen, revealing the response of the "bulk" material.[215] In the vertical geometry, the weak signals due to the phonon assisted band gap transitions (1) and (2) become substantially increased, whereas above the energy of the maximum of the lateral photoconductivity spectrum the signal decreases much more rapidly as in the lateral case. As a result, a rather narrow peak is observed in the photoconductivity

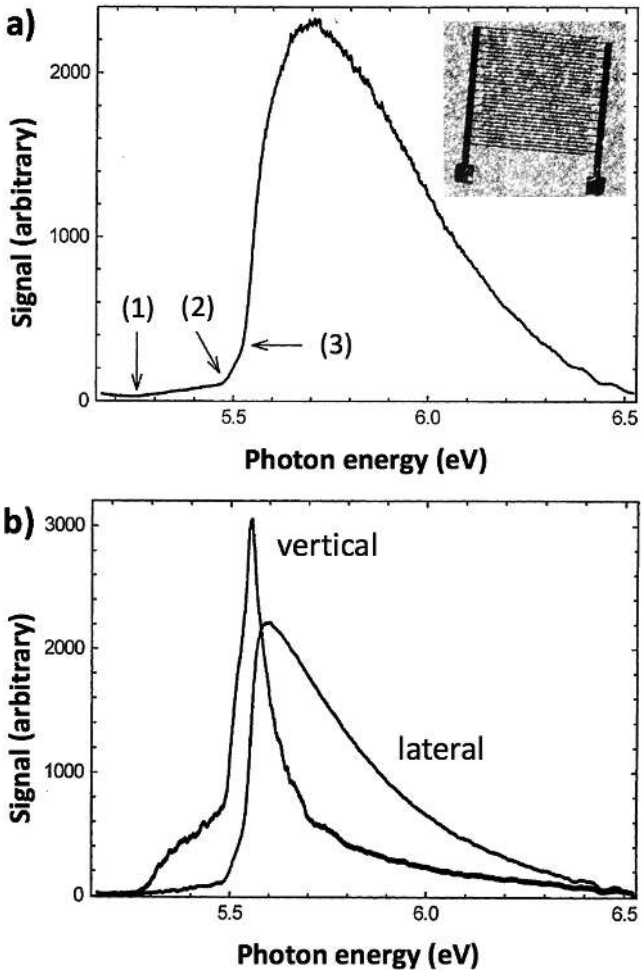

Figure 20. Diamond based photodetectors. a) Photocounductivity spectrum of a polycrystalline chemical vapor deposition diamond, measured in lateral direction by making use of interdigitate electrodes, as those shown on an optical microscopy image in the inset of figure (a). For description of the points marked by arrows see main text. b) Comparison of photoconductivity spectra obtained in lateral and vertical direction of the current through the sample. Reproduced with permission.[46,215] Copyright 1999 and 2001 respectively, Elsevier.

spectrum of vertical devices Figure 20b. While the relevance of this observation was perhaps not fully explained in the original paper of Hiscock and Collins,[215] the appearance of the narrow photoconductivity peak is reminiscent of the recently developed highly narrowband single-crystal photodetectors based on perovskites.[216] In the perovskites, the narrowband photodetection is observed below the band gap energy. It is explained by weak below-bandgap absorption, causing excitation of carriers located away from the surfaces from where they can be much more efficiently collected by the electrodes, assisted by the applied electric field, than near surface carriers, which are generated by strongly absorbed short wavelength photons, causing above band gap transitions.[216]

The insensitivity of diamond photodetectors to visible light is usually seen as an advantage in comparison to commercial silicon ultraviolet detectors.[60,217] This solar-blindness characteristics is quantified by a discrimination-ratio, for instance between

© 2016 WILEY-VCH Verlag GmbH & Co. KGaA, Weinheim

the responsivity at 200 nm wavelength and at >230 nm, for which values $>10^6$ were reported.[60,218] While the achieved signal to noise ratio is smaller than those of silicon based UV detectors, especially for polycrystalline diamond remarkable properties have been reported: One outstanding parameter from the literature is the mobility lifetime product, for which values up to 2.7×10^{-2} cm^2 V^{-1} were observed in polycrystalline films.[60] Although this value dates back by almost 20 years, it is as high as novel record values, achieved in single crystals of methylammonium lead bromides, which are applied in sensitive X-ray detectors.[219] Furthermore, the photoconductive gain observed in the diamond films reached values up to 10^6.[60] This high gain is a result of the imbalance between carrier transit time and carrier lifetime. If the lifetime is longer than the transit time, photoexcited carriers can contribute multiple times to the photocurrent. This phenomenon is observed frequently in systems containing numerous defect states, in which one type of photoexcited carrier (either electrons or holes) are trapped, whereas the other type is circulating multiply between the contacts of the detector, before recombination occurs. Such trap states are especially dense in poly-crystalline or nanocrystalline materials[220,221] and besides providing a photoconductive gain they also reduce the band-width of the detector, so that the product of gain times band width is approximately constant for a given material system. To overcome the limitations of a fixed gain times band-width product, phototransistors were developed, in which two-dimensional high mobility transport layers such as graphene or MoS_2 were photo-gated by an appropriate photosensitizer.[179] In these transistors, ultrahigh gain values, which are up to 100 times higher than those reported for polycrystalline diamond were demonstrated with colloidal nanocrystals or solution processed perovskite layers as photosensitizers.[222] Probably inspired by the success of these phototransistors, recently also diamond based photodetectors were tested with the geometry of a bilayer structure.[61] In particular the combination of TiO_2 on diamond were reported to be advantageous in comparison to a purely diamond reference. The bilayer structure showed reduced dark current combined with an increased photocurrent, resulting in higher responsivity.

While diamond based UV detectors are rather sparsely studied, more promising developments are reported for diamond detectors for high energy photon or particle detection.[223–227] Probably most importantly, CVD single crystal Shottky diodes are available as radiation dose meters, to be used in clinical radiation therapy with high energy photons (hard gamma range with photon energies in the MeV range) or with electrons. Such radiation detectors recently became commercially available, from the manufacturer PTW-Freiburg (Germany).[228–231] The commercial detectors exhibit a response of 1 nC Gy^{-1} and a very low dose rate dependence, combined with a high spatial resolution. The dosimeter response is stable within +—0.5%, but for stabilization a pre-irradiation step is required. Besides the overall promising detector parameters, the dosimeters used in radiation therapy should absorb the equivalent amount of radiation as human tissue. This is closely the case for diamond, since the order number of Carbon (Z = 6) almost matches the effective atomic number of human tissue (Z_{eff} ≈7.42). Comparisons of the performance of the CVD diamond diodes with ionization chambers, or with Si based radiation detecting diodes resulted in clear advantages for the diamond device, in respect to radiation hardness, temperature stability, insensitivity to radiation direction or energy, and response stability, and dose rate stability. Thus, the obtained results suggest the investigated synthetic diamond-based detectors as a prime candidate for small field clinical radiation dosimetry in advanced radiation therapy techniques, or in combination with some innovative technologies in medicine such as the CyberKnife, Gamma Knife, or Tomotherapy, being important high-end tools for cancer treatment.[230]

7. Conclusions and Outlook

Carbon is an abundantly available element with potentially low environmental impact. In form of its allotropes, semiconducting materials can be isolated with rather individual optoelectric properties, strongly depending on their molecular dimensionality. Photodetector devices presented within this review (summarized in part within Table 1 and Table 2) demonstrate that the intrinsic properties of carbon allotropes are sufficient to build devices with technological relevant performance within a spectral range from gamma to THz radiation (see Figure 1). Astonishingly, the detector performances are comparable to commercial and novel nanostructured inorganic detectors, which require several different material systems to cover the same spectral range.[232] Going from high energy to low energy radiation distinct regimes can be identified where different carbon allotropes are more beneficial for serving as photoactive layer in a corresponding photodetector.

For very high radiation energies of some MeV, diamonds can be utilized for ionizing gamma quant detection. Commercial diamond-based dose meters are already available and show superior performance over ionization chambers and Si-based technologies. Another field in which diamond could be part of the next generation technology is extreme- and deep- UV detection for wavelengths <220 nm. In combination with its durability and radiation hardness diamond detectors could become viable for the chip-industry where the feature-size reduction in lithographic processes requires already extreme UV light monitoring. Advances in CVD grown single crystalline diamond devices and surface passivation methods are promising and encouraging to the field.

Zero dimensional C60, fullerene derivatives and GQDs are predominantly used for UV and visible light detection. Photodetectors with C60 have been demonstrated to achieve responsivities exceeding unity and detectivites of more than 10^{11} Jones in a range from 300 to 500 nm with the potential of up to 1 MHz response speed. Nevertheless, C60 and derivatives thereof are investigated more prominently for their strong electron accepting nature in photoactive blends of organic photodetectors. They enable nearly 100% efficient charge carrier separation which increases the responsivity. In order to gain also high detectivities the remaining challenge on the device fabrication is a successful suppression of the dark current. Latter can be mostly achieved by interface engineering and reports of detectivites in the order of 10^{13} Jones are very promising to the field.[233] Driven by the development of new absorber polymers

© 2016 WILEY-VCH Verlag GmbH & Co. KGaA, Weinheim

for organic solar cells the spectral responsivity can be theoretically tailored to any need, putting even color imaging within reach.[19,25,26,52,234]

GQD are a rather young species of the zero dimensional carbon allotropes with a strong UV sensitivity. Unlike in C60, the conjugated electron system in GQDs can be influenced by quantum confinement, doping and chemical modifications, thus allowing the opening and tuning of the particle bandgap. Thereby parts of the visible and NIR spectrum become accessible. In spite of the great potential GQDs offer, current synthesis methods are very challenging and difficult to control. However, new synthesis methods and chemical modifications are already promising for the upcoming GQD generations. Currently more opto-electronic characterization studies are needed to gain understanding of all structure-property relations of GQDs which will then rapidly evolve the GQD development for photodetectors. First GQD-based photoconducting devices are showing already a promising responsivity in the order of 10^7 A W^{-1} and a detectivity in the order of 10^{13} Jones for UV detection and 10^{11} Jones for VIS detection.[49,56,98]

Improvements in purification of semiconducting SWCNTs has contributed significantly to the advances of recent photonic detectors comprising a CNT/C60 heterojunction. Devices were demonstrated operating in the PV mode with a detectivity approaching 10^{12} Jones in the NIR spectrum, only more one order of magnitude below the best existing InGaAs detectors with 10^{13} Jones. Since the bandgap of individual semiconducting SWCNTs is determined by van Hove singularities in the density of states, the tube diameter and chirality can be used to selectively determine the device's peak responsivity. With future improvements in purification and selection methods for semiconducting and metallic CNTs, not just broadband but also multicolor detection is plausible, and the overall CNT photodetector performance is expected to increase even further. Differently, in photodetectors with mixed CNTs, the thermo-electric properties seem to outweigh the photonic charge carrier generation. For instance, in CVD grown SWCNTs pn-junctions, a strong PTE effect has been demonstrated, significantly expanding the spectral sensitivity to (polarized) THz radiation and up to mm wavelengths. Additionally, CNTs exhibit exceptional bolometric sensitivities for non-cooled devices. By increasing the active area in future CNT photodetectors, they are most likely to outperform existing room-temperature operated bolometers. Nevertheless, there are a number of challenges that need to be addressed, especially on the topic of understanding charge transport mechanisms in SWCNTs films, which is essential for developing detector systems with higher responsivities. While highly prisitine SWCNTs with more stable doping and/or better uniformity can be a direction of improvement, deeper research on the charge transport phenomenon in CNT networks with different bandgaps and percolation densities will be fundamental to improve such systems in the future. Studies with the availability of well-defined materials and against the background of first reported very promising CNT-based photodetectors, can put commercial application in the near future.

As a result of its zero-bandgap, graphene photodetectors have an exceptional broad absorption and cover a spectral range from UV to NIR. Graphene photodetectors further benefit from the high charge carrier mobility in single layer graphene enabling an electric bandwidth of intrinsic 262 GHz.[51] For high speed communication purposes the integration of graphene with Si-waveguide structures, in compliance with CMOS technologies, has been already successfully demonstrated.[45] Nevertheless, the low absolute absorption of graphene is limiting the responsivity in stand-alone photodetectors. Thus, device concepts are anticipated where the charge carrier generation in graphene is amplified by photoconductive gain, as demonstrated in photo-gated transistors and layered van der Waals heterojunctions. Detectivites in the visible spectrum exceeding 10^{14} Jones are reported. Long wavelength THz and FIR radiation however, requires integration of metallic antennae, to efficiently couple photons to the plasmonic modes of graphene. Detecting MIR photons, which can be relevant to biosensing and thermal imaging, remains challenging with graphen since it exhibits an inherent absorption minimum. Bandgap engineering via structuring and stacking of multiple graphene layers is applicable, however a competitive photodetector utilizing either of these concepts has yet to be demonstrated. An additional future challenge for graphene-based photodetectors lies within the preparation of defect free, large area graphene sheets which can be readily integrated into large-scale device fabrication processes. Latter would also decide about the commercialization of graphene photodetectors, as device performances on par with existing technologies were presented already.

Fundamental studies on the underlying detection mechanisms, the progress in purification and preparation routes for certain carbon allotropes and elaborate device fabrication techniques have led to major advances in the development of carbon allotrope based photodetectors. Detector performances were reported approaching, and in part exceeding, state-of-the-art inorganic photodetectors, which is very promising for the future of organic photodetectors and carbon based electronics in general. By further improving synthesis methods and quality of the materials and investigating the opto- and thermoelectric properties in both the pristine carbon allotropes and in hybrid structures, the roadmap points towards possible high performance all carbon-based, room-temperature operated photodetectors highly integrated into existing technologies.

Acknowledgements

This work was supported by the research training group GRK 1896 of the German Research Foundation DFG, which is gratefully acknowledged by M.R. The DFG is further acknowledged by T.H. and C.J.B. for their support within the framework of the SFB 953 (Synthetic Carbon Allotropes). A part of the work was performed at the Energie Campus Nürnberg and supported by funding through the "Aufbruch Bayern" initiative of the state of Bavaria. W.H. thanks the "Österreichische Forschungsförderungsgesellschaft" FFG for financial support via the project Real Nano (Pr. Nr.843598) and acknowledges support by the European Commission via the Marie-Sklodowska Curie action Phonsi (H2020-MSCA-ITN-642656). Nusret S. Güldal is acknowledged for proof reading and valuable input on the manuscript.

Received: July 19, 2016
Revised: August 30, 2016
Published online: November 9, 2016

© 2016 WILEY-VCH Verlag GmbH & Co. KGaA, Weinheim

[1] P. Würfel, *Physics of Solar Cells*, Wiley-VCH Verlag GmbH, Weinheim, Germany, **2005**.
[2] S. Del Sordo, L. Abbene, E. Caroli, A. M. Mancini, A. Zappettini, P. Ubertini, *Sensors* **2009**, *9*, 3491.
[3] S. O. Kasap, M. Zahangir Kabir, J. a. Rowlands, *Curr. Appl. Phys.* **2006**, *6*, 288.
[4] E. Monroy, F. Omnès, F. Calle, *Semicond. Sci. Technol.* **2003**, *18*, R33.
[5] H. Chen, K. Liu, L. Hu, A. A. Al-Ghamdi, X. Fang, *Mater. Today* **2015**, *18*, 493.
[6] J. Zhou, L. Chen, Y. Wang, Y. He, X. Pan, E. Xie, *Nanoscale* **2016**, *8*, 50.
[7] L. Colace, G. Masini, G. Assanto, H.-C. Luan, K. Wada, L. C. Kimerling, *Appl. Phys. Lett.* **2000**, *76*, 1231.
[8] A. Rogalski, *Prog. Quantum Electron.* **2003**, *27*, 59.
[9] L. X. Zhang, W. G. Sun, X. F. Zhang, X. B. Zhu, X. C. Cao, J. J. Si, *Appl. Phys. A* **2014**, *117*, 853.
[10] S. C. Jain, M. Willander, J. Narayan, R. Van Overstraeten, *J. Appl. Phys.* **2000**, *87*, 965.
[11] P. Capper, S. Irvine, T. Joyce, in *Springer Handb. Electron. Photonic Mater.*, Springer US, Boston, MA, **2006**, pp. 271–301.
[12] L. Vivien, J. Osmond, J.-M. Fédéli, D. Marris-Morini, P. Crozat, J.-F. Damlencourt, E. Cassan, Y. Lecunff, S. Laval, *Opt. Express* **2009**, *17*, 6252.
[13] M. J. R. Heck, H.-W. Chen, A. W. Fang, B. R. Koch, D. Liang, H. Park, M. N. Sysak, J. E. Bowers, *IEEE J. Sel. Top. Quantum Electron.* **2011**, *17*, 333.
[14] R. Soref, *IEEE J. Sel. Top. Quantum Electron.* **2006**, *12*, 1678.
[15] S. Pang, Y. Hernandez, X. Feng, K. Müllen, *Adv. Mater.* **2011**, *23*, 2779.
[16] J. Zaumseil, *Semicond. Sci. Technol.* **2015**, *30*, 74001.
[17] H. Kang, G. Kim, J. Kim, S. Kwon, H. Kim, K. Lee, *Adv. Mater.* **2016**, DOI: 10.1002/adma.201601197.
[18] M. Bernardi, J. Lohrman, P. V. Kumar, A. Kirkeminde, N. Ferralis, J. C. Grossman, S. Ren, *ACS Nano* **2012**, *6*, 8896.
[19] K. J. Baeg, M. Binda, D. Natali, M. Caironi, Y. Y. Noh, *Adv. Mater.* **2013**, *25*, 4267.
[20] T. Mueller, F. Xia, P. Avouris, *Nat. Photonics* **2010**, *4*, 297.
[21] X. He, N. Fujimura, J. M. Lloyd, K. J. Erickson, A. A. Talin, Q. Zhang, W. Gao, Q. Jiang, Y. Kawano, R. H. Hauge, F. Léonard, J. Kono, *Nano Lett.* **2014**, *14*, 3953.
[22] S. Kirner, M. Sekita, D. M. Guldi, *Adv. Mater.* **2014**, *26*, 1482.
[23] B. W. D'Andrade, S. R. Forrest, *Adv. Mater.* **2004**, *16*, 1585.
[24] B. Geffroy, P. le Roy, C. Prat, *Polym. Int.* **2006**, *55*, 572.
[25] Y. S. Rim, S. H. Bae, H. Chen, N. De Marco, Y. Yang, *Adv. Mater.* **2016**, *28*, 4415.
[26] H. Dong, H. Zhu, Q. Meng, X. Gong, W. Hu, *Chem. Soc. Rev.* **2012**, *41*, 1754.
[27] H. W. Kroto, J. R. Heath, S. C. O'Brien, R. F. Curl, R. E. Smalley, *Nature* **1985**, *318*, 162.
[28] M. Gong, T. A. Shastry, Y. Xie, M. Bernardi, D. Jasion, K. A. Luck, T. J. Marks, J. C. Grossman, S. Ren, M. C. Hersam, *Nano Lett.* **2014**, *14*, 5308.
[29] Y. Nakai, K. Honda, K. Yanagi, H. Kataura, T. Kato, T. Yamamoto, Y. Maniwa, *Appl. Phys. Express* **2014**, *7*, 25103.
[30] X. Li, S. P. Lau, L. Tang, R. Ji, P. Yang, *J. Mater. Chem. C* **2013**, *1*, 7308.
[31] R. Sekiya, Y. Uemura, H. Murakami, T. Haino, *Angew. Chemie Int. Ed.* **2014**, *53*, 5619.
[32] K. S. Novoselov, A. K. Geim, S. V. Morozov, D. Jiang, Y. Zhang, S. V. Dubonos, I. V. Grigorieva, A. A. Firsov, *Science* **2004**, *306*, 666.
[33] P. H. Wöbkenberg, D. D. C. Bradley, D. Kronholm, J. C. Hummelen, D. M. de Leeuw, M. Cölle, T. D. Anthopoulos, *Synth. Met.* **2008**, *158*, 468.
[34] S. Ji, S. J. Kim, W. Song, S. Myung, J. Heo, J. Lim, K.-S. An, S. S. Lee, *RSC Adv.* **2016**, *6*, 19372.
[35] L. Ma, J. Ouyang, Y. Yang, *Appl. Phys. Lett.* **2004**, *84*, 4786.
[36] F. Guo, Z. Xiao, J. Huang, *Adv. Opt. Mater.* **2013**, *1*, 289.
[37] L. Tang, R. Ji, X. Li, G. Bai, C. P. Liu, J. Hao, J. Lin, H. Jiang, K. S. Teng, Z. Yang, S. P. Lau, *ACS Nano* **2014**, *8*, 6312.
[38] Q. Zhang, J. Jie, S. Diao, Z. Shao, Q. Zhang, L. Wang, W. Deng, W. Hu, H. Xia, X. Yuan, S. T. Lee, *ACS Nano* **2015**, *9*, 1561.
[39] Y. Liu, N. Wei, Q. Zeng, J. Han, H. Huang, D. Zhong, F. Wang, L. Ding, J. Xia, H. Xu, Z. Ma, S. Qiu, Q. Li, X. Liang, Z. Zhang, S. Wang, L. M. Peng, *Adv. Opt. Mater.* **2016**, *4*, 238.
[40] X. He, X. Wang, S. Nanot, K. Cong, Q. Jiang, A. A. Kane, J. E. M. Goldsmith, R. H. Hauge, F. Léonard, J. Kono, *ACS Nano* **2013**, *7*, 7271.
[41] M. Freitag, T. Low, W. Zhu, H. Yan, F. Xia, P. Avouris, *Nat. Commun.* **2013**, *4*, DOI: 10.1038/ncomms2951.
[42] X. Cai, A. B. Sushkov, R. J. Suess, M. M. Jadidi, G. S. Jenkins, L. O. Nyakiti, R. L. Myers-Ward, S. Li, J. Yan, D. K. Gaskill, T. E. Murphy, H. D. Drew, M. S. Fuhrer, *Nat. Nanotechnol.* **2014**, *9*, 814.
[43] C. O. Kim, S. Kim, D. H. Shin, S. S. Kang, J. M. Kim, C. W. Jang, S. S. Joo, J. S. Lee, J. H. Kim, S.-H. Choi, E. Hwang, *Nat. Commun.* **2014**, *5*, 3249.
[44] C.-H. Liu, Y.-C. Chang, T. B. Norris, Z. Zhong, *Nat. Nanotechnol.* **2014**, *9*, 273.
[45] A. Pospischil, M. Humer, M. M. Furchi, D. Bachmann, R. Guider, T. Fromherz, T. Mueller, *Nat. Photonics* **2013**, *7*, 892.
[46] M. D. Whitfield, S. P. Lansley, O. Gaudin, R. D. McKeag, N. Rizvi, R. B. Jackman, *Diam. Relat. Mater.* **2001**, *10*, 693.
[47] S. M. Sze, K. K. Ng, *Physics of Semiconductor Devices*, John Wiley & Sons, Inc., Hoboken, NJ, USA, **2007**.
[48] K. Szendrei, F. Cordella, M. V. Kovalenko, M. Böberl, G. Hesser, M. Yarema, D. Jarzab, O. V. Mikhnenko, A. Gocalinska, M. Saba, F. Quochi, A. Mura, G. Bongiovanni, P. W. M. Blom, W. Heiss, M. A. Loi, *Adv. Mater.* **2009**, *21*, 683.
[49] S.-H. Cheng, T.-M. Weng, M.-L. Lu, W.-C. Tan, J.-Y. Chen, Y.-F. Chen, *Sci. Rep.* **2013**, *3*, 2694.
[50] G. Pace, A. Grimoldi, M. Sampietro, D. Natali, M. Caironi, *Semicond. Sci. Technol.* **2015**, *30*, 104006.
[51] A. Urich, K. Unterrainer, T. Mueller, *Nano Lett.* **2011**, *11*, 2804.
[52] R. D. Jansen-van Vuuren, A. Armin, A. K. Pandey, P. L. Burn, P. Meredith, *Adv. Mater.* **2016**, *28*, 4766.
[53] K. J. Erikson, X. He, A. A. Talin, B. Mills, R. H. Hauge, T. Iguchi, N. Fujimura, Y. Kawano, J. Kono, F. Léonard, *ACS Nano* **2015**, *9*, 11618.
[54] R. Ahmed, A. Kadashchuk, C. Simbrunner, G. Schwabegger, M. Havlicek, E. Głowacki, N. S. Sariciftci, M. A. Baig, H. Sitter, *Org. Electron. Physics, Mater. Appl.* **2014**, *15*, 175.
[55] L. Wei, J. Yao, H. Fu, *ACS Nano* **2013**, *7*, 7573.
[56] C. O. Kim, S. W. Hwang, S. Kim, D. H. Shin, S. S. Kang, J. M. Kim, C. W. Jang, J. H. Kim, K. W. Lee, S.-H. Choi, E. Hwang, *Sci. Rep.* **2014**, *4*, 4.
[57] Y. Liu, F. Wang, X. Wang, X. Wang, E. Flahaut, X. Liu, Y. Li, X. Wang, Y. Xu, Y. Shi, R. Zhang, *Nat. Commun.* **2015**, *6*, 8589.
[58] S. Park, S. J. Kim, J. H. Nam, G. Pitner, T. H. Lee, A. L. Ayzner, H. Wang, S. W. Fong, M. Vosgueritchian, Y. J. Park, M. L. Brongersma, Z. Bao, *Adv. Mater.* **2015**, *27*, 759.
[59] R. Lu, C. Christianson, B. Weintrub, J. Z. Wu, *ACS Appl. Mater. Interfaces* **2013**, *5*, 11703.
[60] R. D. McKeag, R. B. Jackman, *Diam. Relat. Mater.* **1998**, *7*, 513.
[61] Z. Liu, F. Li, S. Li, C. Hu, W. Wang, F. Wang, F. Lin, H. Wang, *Sci. Rep.* **2015**, *5*, 14420.
[62] G. E. Fernandes, J. H. Kim, A. K. Sood, J. Xu, *Adv. Funct. Mater.* **2013**, *23*, 4678.

 © 2016 WILEY-VCH Verlag GmbH & Co. KGaA, Weinheim

[63] M. Mahjouri-Samani, Y. S. Zhou, X. N. He, W. Xiong, P. Hilger, Y. F. Lu, *Nanotechnology* **2013**, *24*, 35502.
[64] K. Narita, R. Kuribayashi, E. Altintas, H. Someya, K. Tsuda, K. Ohashi, T. Tabuchi, S. Okubo, M. Imazato, S. Komatsubara, *Sensors Actuators A Phys.* **2013**, *195*, 142.
[65] H. W. Kroto, J. R. Heath, S. C. O'Brien, R. F. Curl, R. E. Smalley, *Nature* **1985**, *318*, 162.
[66] M. S. Dresselhaus, G. Dresselhaus, P. C. Eklund, *Science of Fullerenes and Carbon Nanotubes*, Elsevier Science, **1996**.
[67] C. J. Brabec, V. Dyakonov, U. Scherf, *Organic Photovoltaics: Materials, Device Physics, and Manufacturing Technologies*, WILEY-VCH Verlag, Weinheim, **2009**.
[68] T. B. Singh, N. Marjanović, G. J. Matt, S. Günes, N. S. Sariciftci, A. Montaigne Ramil, A. Andreev, H. Sitter, R. Schwödiauer, S. Bauer, *Org. Electron.* **2005**, *6*, 105.
[69] G. J. Matt, T. B. Singh, N. S. Sariciftci, A. Montaigne Ramil, H. Sitter, *Appl. Phys. Lett.* **2006**, *88*, 263516.
[70] W. A. S. X. Xu, R. Ray, Y. Gu, H. J. Ploehn, L. Gearheart, K. Raker, *J. Am. Chem. Soc.* **2004**, *126*, 12736.
[71] S. K. Lai, C. M. Luk, L. Tang, K. S. Teng, S. P. Lau, *Nanoscale* **2015**, *7*, 5338.
[72] A. D. Güçlü, P. Potasz, M. Korkusinski, P. Hawrylak, *Graphene Quantum Dots* **2013**.
[73] X. Luo, L. Du, W. Lv, L. Sun, Y. Li, Y. Peng, F. Zhao, J. Zhang, Y. Tang, Y. Wang, *Synth. Met.* **2015**, *210*, 230.
[74] G. Yu, J. Gao, J. C. Hummelen, F. Wudl, A. J. Heeger, *Science* **1995**, *270*, 1789.
[75] C. J. Brabec, V. Dyakonov, U. Scherf, *Organic Photovoltaics: Materials, Device Physics, and Manufacturing Technologies*, **2009**.
[76] J. Zhao, Y. Li, G. Yang, K. Jiang, H. Lin, H. Ade, W. Ma, H. Yan, *Nat. Energy* **2016**, *1*, 15027.
[77] J. W. Rumer, I. McCulloch, *Mater. Today* **2015**, *18*, 425.
[78] Y. Liu, C.-C. Chen, Z. Hong, J. Gao, Y. M. Yang, H. Zhou, L. Dou, G. Li, Y. Yang, *Sci. Rep.* **2013**, *3*, 3356.
[79] G. Pace, A. Grimoldi, M. Sampietro, D. Natali, M. Caironi, *Semicond. Sci. Technol.* **2015**, *30*, 104006.
[80] K. J. Baeg, M. Binda, D. Natali, M. Caironi, Y. Y. Noh, *Adv. Mater.* **2013**, *25*, 4267.
[81] G. Itskos, P. Papagiorgis, D. Tsokkou, A. Othonos, F. Hermerschmidt, S. P. Economopoulos, M. Yarema, W. Heiss, S. Choulis, *Adv. Energy Mater.* **2013**, *3*, 1490.
[82] T. Mentzel, V. Porter, S. Geyer, K. MacLean, M. Bawendi, M. Kastner, *Phys. Rev. B* **2008**, *77*, 75316.
[83] G. Konstantatos, E. H. Sargent, *Nat. Nanotechnol.* **2010**, *5*, 391.
[84] Y. Gao, M. Aerts, C. S. S. Sandeep, E. Talgorn, T. J. Savenije, S. Kinge, L. D. a. Siebbeles, A. J. Houtepen, *ACS Nano* **2012**, *6*, 9606.
[85] T. Rauch, M. Böberl, S. F. Tedde, J. Fürst, M. V. Kovalenko, G. Hesser, U. Lemmer, W. Heiss, O. Hayden, *Nat. Photonics* **2009**, *3*, 332.
[86] S. Kahmann, A. Mura, L. Protesescu, M. V. Kovalenko, C. J. Brabec, M. A. Loi, *J. Mater. Chem. C* **2015**, *3*, 5499.
[87] A. Gocalińska, M. Saba, F. Quochi, M. Marceddu, K. Szendrei, J. Gao, M. a. Loi, M. Yarema, R. Seyrkammer, W. Heiss, A. Mura, G. Bongiovanni, *J. Phys. Chem. Lett.* **2010**, *1*, 1149.
[88] P. Büchele, M. Richter, S. F. Tedde, G. J. Matt, G. N. Ankah, R. Fischer, M. Biele, W. Metzger, S. Lilliu, O. Bikondoa, J. E. Macdonald, C. J. Brabec, T. Kraus, U. Lemmer, O. Schmidt, *Nat. Photonics* **2015**, *9*, 843.
[89] S. O. Kasap, *J. Phys. D. Appl. Phys.* **2000**, *33*, 2853.
[90] A. D. Güclü, P. Potasz, M. Korkusinski, P. Hawrylak, *Graphene Quantum Dots*, Springer Berlin Heidelberg, **2014**.
[91] Z. Jin, P. Owour, S. Lei, L. Ge, *Curr. Opin. Colloid Interface Sci.* **2015**, *20*, 439.
[92] Z. Gan, S. Xiong, X. Wu, T. Xu, X. Zhu, X. Gan, J. Guo, J. Shen, L. Sun, P. K. Chu, *Adv. Opt. Mater.* **2013**, *1*, 926.
[93] H. Kalita, V. Harikrishnan, M. Aslam, *Int. J. Nanotechnol.* **2014**, *11*, 75.
[94] Y. Yang, R. Murali, *Appl. Phys. Lett.* **2011**, *98*, 93116.
[95] S. Malik, A. K. Ray, S. Bruce, *Semicond. Sci. Technol.* **2005**, *20*, 453.
[96] J. M. Dawlaty, S. Shivaraman, M. Chandrashekhar, F. Rana, M. G. Spencer, *Appl. Phys. Lett.* **2008**, *92*, 42116.
[97] F. Wang, G. Dukovic, L. E. Brus, T. F. Heinz, *Phys. Rev. Lett.* **2004**, *92*, 177401.
[98] T. Van Tam, S. H. Hur, J. S. Chung, W. M. Choi, *Sensors Actuators A Phys.* **2015**, *233*, 368.
[99] R. Bacon, *J. Appl. Phys.* **1960**, *31*, 283.
[100] S. Iijima, *Nature* **1991**, *354*, 56.
[101] M. F. L. De Volder, S. H. Tawfick, R. H. Baughmann, A. J. Hart, *Science* **2013**, *339*, 535.
[102] M. S. Dresselhaus, G. Dresselhaus, P. Avouris, *Carbon Nanotubes Synthesis, Structure, Properties, and Applications*, Springer Berlin Heidelberg, Heidelberg, **2001**.
[103] N. Komatsu, F. Wang, *Materials (Basel)*. **2010**, *3*, 3818.
[104] M. J. O'Connell, S. M. Bachilo, C. B. Huffman, V. C. Moore, M. S. Strano, E. H. Haroz, K. L. Rialon, P. J. Boul, W. H. Noon, C. Kittrell, J. Ma, R. H. Hauge, R. B. Weisman, R. E. Smalley, *Science* **2002**, *297*, 593.
[105] H. Kataura, Y. Kumazawa, Y. Maniwa, I. Umezu, S. Suzuki, Y. Ohtsuka, Y. Achiba, *Synth. Met.* **1999**, *103*, 2555.
[106] R. B. Weisman, S. M. Bachilo, *Nano Lett.* **2003**, *3*, 1235.
[107] H. Ye, X. J. Wang, W. Lin, C. P. Wong, Z. M. Zhang, *Appl. Phys. Lett.* **2012**, *101*, 141909.
[108] S. Motavas, A. Ivanov, A. Nojeh, *Phys. E Low-Dimensional Syst. Nanostructures* **2014**, *56*, 79.
[109] M. P. Ramuz, M. Vosgueritchian, P. Wei, C. Wang, Y. Gao, Y. Wu, Y. Chen, Z. Bao, *ACS Nano* **2012**, *6*, 10384.
[110] F. Wang, G. Dukovic, L. E. Brus, T. F. Heinz, *Science* **2005**, *308*, 838.
[111] J. Maultzsch, R. Pomraenke, S. Reich, E. Chang, D. Prezzi, A. Ruini, E. Molinari, M. S. Strano, C. Thomsen, C. Lienau, *Phys. Rev. B* **2005**, *72*, 241402.
[112] D. J. Bindl, M. Y. Wu, F. C. Prehn, M. S. Arnold, *Nano Lett.* **2011**, *11*, 455.
[113] V. Barone, J. E. Peralta, J. Uddin, G. E. Scuseria, *J. Chem. Phys.* **2006**, *124*, 24709.
[114] Y. Hirana, G. Juhasz, Y. Miyauchi, S. Mouri, K. Matsuda, N. Nakashima, *Sci. Rep.* **2013**, *3*, 2959.
[115] F. Wang, G. Dukovic, L. E. Brus, T. F. Heinz, *Science* **2005**, *308*, 838.
[116] M. Freitag, Y. Martin, J. A. Misewich, R. Martel, P. Avouris, *Nano Lett.* **2003**, *3*, 1067.
[117] K. Balasubramanian, Y. Fan, M. Burghard, K. Kern, M. Friedrich, U. Wannek, A. Mews, *Appl. Phys. Lett.* **2004**, *84*, 2400.
[118] Y. H. Ahn, A. W. Tsen, B. Kim, Y. W. Park, J. Park, *Nano Lett.* **2007**, *7*, 3320.
[119] T. Dürkop, S. A. Getty, E. Cobas, M. S. Fuhrer, *Nano Lett.* **2004**, *4*, 35.
[120] S. J. Kang, C. Kocabas, T. Ozel, M. Shim, N. Pimparkar, M. a. Alam, S. V Rotkin, J. a. Rogers, *Nat. Nanotechnol.* **2007**, *2*, 230.
[121] S. J. Choi, P. Bennett, K. Takei, C. Wang, C. C. Lo, A. Javey, J. Bokor, *ACS Nano* **2013**, *7*, 798.
[122] X. He, F. Léonard, J. Kono, *Adv. Opt. Mater.* **2015**, *3*, 989.
[123] A. J. Siitonen, D. A. Tsyboulski, S. M. Bachilo, R. B. Weisman, *J. Phys. Chem. Lett.* **2010**, *1*, 2189.
[124] J.-S. Lauret, C. Voisin, G. Cassabois, C. Delalande, P. Roussignol, O. Jost, L. Capes, *Phys. Rev. Lett.* **2003**, *90*, 57404.
[125] J. P. Small, K. M. Perez, P. Kim, *Phys. Rev. Lett.* **2003**, *91*, 256801.
[126] S. Fujita, J. McNabb III, A. Suzuki, *J. Mod. Phys.* **2013**, *4*, 628.
[127] M. Barkelid, V. Zwiller, *Nat. Photonics* **2013**, *8*, 47.

© 2016 WILEY-VCH Verlag GmbH & Co. KGaA, Weinheim

[128] F. Rao, X. Liu, T. Li, Y. Zhou, Y. Wang, *Nanotechnology* **2009**, *20*, 55501.
[129] Y. Liu, S. Wang, L.-M. Peng, *Adv. Energy Mater.* **2016**, *6*, 1600522.
[130] G. Vera-Reveles, T. J. Simmons, M. Bravo-Sánchez, M. A. Vidal, H. Navarro-Contreras, F. J. González, *ACS Appl. Mater. Interfaces* **2011**, *3*, 3200.
[131] S. Nanot, A. W. Cummings, C. L. Pint, A. Ikeuchi, T. Akiho, K. Sueoka, R. H. Hauge, F. Léonard, J. Kono, *Sci. Rep.* **2013**, *3*, 1335.
[132] A. Rogalski, F. Sizov, *Opto-Electronics Rev.* **2011**, *19*, 121.
[133] Y. Nonoguchi, K. Ohashi, R. Kanazawa, K. Ashiba, K. Hata, T. Nakagawa, C. Adachi, T. Tanase, T. Kawai, *Sci. Rep.* **2013**, *3*, 3344.
[134] D. J. Bindl, M. S. Arnold, *J. Phys. Chem. C* **2013**, *117*, 2390.
[135] J. Lefebvre, P. Finnie, *J. Phys. Chem. C* **2009**, *113*, 7536.
[136] Y. Xie, M. Gong, T. A. Shastry, J. Lohrman, M. C. Hersam, S. Ren, *Adv. Mater.* **2013**, *25*, 3433.
[137] B. Pradhan, K. Setyowati, H. Liu, D. H. Waldeck, J. Chen, *Nano Lett.* **2008**, *8*, 1142.
[138] B. Pradhan, R. R. Kohlmeyer, K. Setyowati, H. A. Owen, J. Chen, *Carbon N. Y.* **2009**, *47*, 1686.
[139] R. Lu, C. Christianson, A. Kirkeminde, S. Ren, J. Wu, *Nano Lett.* **2012**, *12*, 6244.
[140] E. Kymakis, G. A. J. Amaratunga, *Appl. Phys. Lett.* **2002**, *80*, 112.
[141] Z. Xu, Y. Wu, B. Hu, I. N. Ivanov, D. B. Geohegan, *Appl. Phys. Lett.* **2005**, *87*, 1.
[142] T. Schuettfort, A. Nish, R. J. Nicholas, *Nano Lett.* **2009**, *9*, 3871.
[143] Z. Wang, H. Pedrosa, T. Krauss, L. Rothberg, *Phys. Rev. Lett.* **2006**, *96*, 3.
[144] D. J. Bindl, N. S. Safron, M. S. Arnold, *ACS Nano* **2010**, *4*, 5657.
[145] J. M. Holt, A. J. Ferguson, N. Kopidakis, B. A. Larsen, J. Bult, G. Rumbles, J. L. Blackburn, *Nano Lett.* **2010**, *10*, 4627.
[146] S. D. Stranks, C. Weisspfennig, P. Parkinson, M. B. Johnston, L. M. Herz, R. J. Nicholas, *Nano Lett.* **2011**, *11*, 66.
[147] S. Ren, M. Bernardi, R. R. Lunt, V. Bulovic, J. C. Grossman, S. Gradecak, *Nano Lett.* **2011**, *11*, 5316.
[148] W. Hou, N.-J. Zhao, D. Meng, J. Tang, Y. Zeng, Y. Wu, Y. Weng, C. Cheng, X. Xu, Y. Li, J.-P. Zhang, Y. Huang, C. W. Bielawski, J. Geng, *ACS Nano* **2016**, *10*, 5189.
[149] K. Nishimra, M. Fujii, R. Jono, K. Yamashita, *J. Phys. Chem. C* **2015**, *119*, 26258.
[150] A. Nish, J.-Y. Hwang, J. Doig, R. J. Nicholas, *Nat. Nanotechnol.* **2007**, *2*, 640.
[151] A. Nakamura, T. Koyama, Y. Miyata, H. Shinohara, *J. Phys. Chem. C* **2016**, *120*, 4647.
[152] S. D. Stranks, S. N. Habisreutinger, B. Dirks, R. J. Nicholas, *Adv. Mater.* **2013**, *25*, 4365.
[153] A. J. Ferguson, J. L. Blackburn, J. M. Holt, N. Kopidakis, R. C. Tenent, T. M. Barnes, M. J. Heben, G. Rumbles, *J. Phys. Chem. Lett.* **2010**, *1*, 2406.
[154] D. J. Bindl, M. J. Shea, M. S. Arnold, *Chem. Phys.* **2013**, *413*, 29.
[155] M. S. Arnold, J. L. Blackburn, J. J. Crochet, S. K. Doorn, J. G. Duque, A. Mohite, H. Telg, *Phys. Chem. Chem. Phys.* **2013**, *15*, 14896.
[156] P. R. Wallace, *Phys. Rev.* **1947**, *71*, 622.
[157] H. P. Boehm, A. Clauss, G. O. Fischer, U. Hofmann, *Zeitschrift für Anorg. und Allg. Chemie* **1962**, *316*, 119.
[158] A. K. Geim, *Phys. Scr.* **2012**, *T146*, 14003.
[159] S. Das Sarma, S. Adam, E. H. Hwang, E. Rossi, *Rev. Mod. Phys.* **2011**, *83*, 407.
[160] M. Freitag, T. Low, F. N. Xia, P. Avouris, *Nat. Photonics* **2013**, *7*, 53.
[161] T. Low, P. Avouris, *ACS Nano* **2014**, *8*, 1086.
[162] R. R. Nair, P. Blake, a. N. Grigorenko, K. S. Novoselov, T. J. Booth, T. Stauber, N. M. R. Peres, A. K. Geim, *Science* **2008**, *320*, 1308.
[163] K. F. Mak, L. Ju, F. Wang, T. F. Heinz, *Solid State Commun.* **2012**, *152*, 1341.
[164] N. M. R. Peres, *Rev. Mod. Phys.* **2010**, *82*, 2673.
[165] Z. Q. Li, E. a. Henriksen, Z. Jiang, Z. Hao, M. C. Martin, P. Kim, H. L. Stormer, D. N. Basov, *Nat. Phys.* **2008**, *4*, 532.
[166] H. M. Dong, J. Zhang, F. M. Peeters, W. Xu, *J. Appl. Phys.* **2009**, *106*, 43103.
[167] L. Huang, G. V. Hartland, L.-Q. C. Luxmi, R. M. Feenstra, C. Lian, K. Tahy, H. Xing, *Nano Lett.* **2010**, *10*, 1308.
[168] P. A. Obraztsov, M. G. Rybin, A. V. Tyurnina, S. V. Garnov, E. D. Obraztsova, A. N. Obraztsov, Y. P. Svirko, *Nano Lett.* **2011**, *11*, 1540.
[169] S. Winnerl, M. Orlita, P. Plochocka, P. Kossacki, M. Potemski, T. Winzer, E. Malic, A. Knorr, M. Sprinkle, C. Berger, W. A. De Heer, H. Schneider, M. Helm, *Phys. Rev. Lett.* **2011**, *107*, 237401.
[170] F. Rana, *Phys. Rev. B – Condens. Matter Mater. Phys.* **2007**, *76*, 1.
[171] D. Brida, A. Tomadin, C. Manzoni, Y. J. Kim, A. Lombardo, S. Milana, R. R. Nair, K. S. Novoselov, a. C. Ferrari, G. Cerullo, M. Polini, *Nat. Commun.* **2013**, *4*, 1987.
[172] A. K. Geim, K. S. Novoselov, *Nat. Mater.* **2007**, *6*, 183.
[173] A. H. Castro Neto, F. Guinea, N. M. R. Peres, K. S. Novoselov, A. K. Geim, *Rev. Mod. Phys.* **2009**, *81*, 109.
[174] J.-H. Chen, C. Jang, S. Xiao, M. Ishigami, M. S. Fuhrer, *Nat. Nanotechnol.* **2008**, *3*, 206.
[175] A. Elschner, S. Kirchmeyer, W. Lovenich, U. Merker, K. Reuter, *PEDOT: Principles and Applications of an Intrinsically Conductive Polymer*, CRC Press, **2010**.
[176] J. Krantz, M. Richter, S. Spallek, E. Spiecker, C. J. Brabec, *Adv. Funct. Mater.* **2011**, *21*, 4784.
[177] Y. Song, W. Fang, R. Brenes, J. Kong, *Nano Today* **2015**, *10*, 681.
[178] J. Li, L. Niu, Z. Zheng, F. Yan, *Adv. Mater.* **2014**, *26*, 5239.
[179] F. H. L. Koppens, T. Mueller, P. Avouris, A. C. Ferrari, M. S. Vitiello, M. Polini, *Nat. Nanotechnol.* **2014**, *9*, 780.
[180] B. H. Nguyen, V. H. Nguyen, *Adv. Nat. Sci. Nanosci. Nanotechnol.* **2016**, *7*, 13002.
[181] P. Gowda, T. Sakorikar, S. K. Reddy, D. B. Ferry, A. Misra, *ACS Appl. Mater. Interfaces* **2014**, *6*, 7485.
[182] P. Gowda, D. R. Mohapatra, A. Misra, *Nanoscale* **2015**, *7*, 15806.
[183] P. Kang, M. C. Wang, P. M. Knapp, S. Nam, *Adv. Mater.* **2016**, *28*, 4639.
[184] T. Mueller, F. Xia, M. Freitag, J. Tsang, P. Avouris, *Phys. Rev. B* **2009**, *79*, 245430.
[185] E. J. H. Lee, K. Balasubramanian, R. T. Weitz, M. Burghard, K. Kern, *Nat. Nanotechnol.* **2008**, *3*, 486.
[186] N. M. Gabor, J. C. W. Song, Q. Ma, N. L. Nair, T. Taychatanapat, K. Watanabe, T. Taniguchi, L. S. Levitov, P. Jarillo-Herrero, *Science* **2011**, *334*, 648.
[187] M. C. Lemme, F. H. L. Koppens, A. L. Falk, M. S. Rudner, H. Park, L. S. Levitov, C. M. Marcus, *Nano Lett.* **2011**, *11*, 4134.
[188] F. Xia, T. Mueller, Y. Lin, A. Valdes-Garcia, P. Avouris, *Nat. Nanotechnol.* **2009**, *4*, 839.
[189] D. Sun, G. Aivazian, A. M. Jones, J. S. Ross, W. Yao, D. Cobden, X. Xu, *Nat. Nanotechnol.* **2012**, *7*, 114.
[190] J. C. W. Song, M. S. Rudner, C. M. Marcus, L. S. Levitov, *Nano Lett.* **2011**, *11*, 4688.
[191] F. Sizov, A. Rogalski, *Prog. Quantum Electron.* **2010**, *34*, 278.
[192] S. Kim, D. H. Shin, C. O. Kim, S. S. Kang, J. M. Kim, C. W. Jang, S. S. Joo, J. S. Lee, J. H. Kim, S. H. Choi, E. Hwang, *ACS Nano* **2013**, *7*, 5168.
[193] J. Yin, H. Wang, H. Peng, Z. Tan, L. Liao, L. Lin, X. Sun, A. L. Koh, Y. Chen, H. Peng, Z. Liu, *Nat. Commun.* **2016**, *7*, 10699.
[194] R. Bistritzer, A. H. MacDonald, *Phys. Rev. B* **2010**, *81*, 245412.
[195] R. de Gail, M. O. Goerbig, F. Guinea, G. Montambaux, A. H. Castro Neto, *Phys. Rev. B* **2011**, *84*, 45436.

© 2016 WILEY-VCH Verlag GmbH & Co. KGaA, Weinheim

[196] K. Kim, S. Coh, L. Z. Tan, W. Regan, J. M. Yuk, E. Chatterjee, M. F. Crommie, M. L. Cohen, S. G. Louie, A. Zettl, *Phys. Rev. Lett.* **2012**, *108*, 246103.
[197] M. Kindermann, E. J. Mele, *Phys. Rev. B* **2011**, *84*, 161406.
[198] T. Kim, H. Kim, S. W. Kwon, Y. Kim, W. K. Park, D. H. Yoon, A.-R. Jang, H. S. Shin, K. S. Suh, W. S. Yang, *Nano Lett.* **2012**, *12*, 743.
[199] N. Gao, X. Fang, *Chem. Rev.* **2015**, *115*, 8294.
[200] M. Long, E. Liu, P. Wang, A. Gao, H. Xia, W. Luo, B. Wang, J. Zeng, Y. Fu, K. Xu, W. Zhou, Y. Lv, S. Yao, M. Lu, Y. Chen, Z. Ni, Y. You, X. Zhang, S. Qin, Y. Shi, W. Hu, D. Xing, F. Miao, *Nano Lett.* **2016**, *16*, 2254.
[201] X. Wang, Z. Cheng, K. Xu, H. K. Tsang, J.-B. Xu, *Nat. Photonics* **2013**, *7*, 1.
[202] N. Youngblood, Y. Anugrah, R. Ma, S. J. Koester, M. Li, *Nano Lett.* **2014**, *14*, 2741.
[203] T. J. Echtermeyer, S. Milana, U. Sassi, A. Eiden, M. Wu, E. Lidorikis, A. C. Ferrari, *Nano Lett.* **2016**, *16*, 8.
[204] Y. Yao, R. Shankar, P. Rauter, Y. Song, J. Kong, M. Loncar, F. Capasso, *Nano Lett.* **2014**, *14*, 3749.
[205] Y. Yao, M. A. Kats, R. Shankar, Y. Song, J. Kong, M. Loncar, F. Capasso, *Nano Lett.* **2014**, *14*, 214.
[206] Y. Liu, R. Cheng, L. Liao, H. Zhou, J. Bai, G. Liu, L. Liu, Y. Huang, X. Duan, *Nat. Commun.* **2011**, *2*, 579.
[207] L. Vicarelli, M. S. Vitiello, D. Coquillat, A. Lombardo, a. C. Ferrari, W. Knap, M. Polini, V. Pellegrini, A. Tredicucci, *Nat. Mater.* **2012**, *11*, 865.
[208] D. Spirito, D. Coquillat, S. L. De Bonis, A. Lombardo, M. Bruna, A. C. Ferrari, V. Pellegrini, A. Tredicucci, W. Knap, M. S. Vitiello, *Appl. Phys. Lett.* **2014**, *104*, 61111.
[209] R. R. Hartmann, J. Kono, M. E. Portnoi, *Nanotechnology* **2014**, *25*, 322001.
[210] A. Di Bartolomeo, *Phys. Rep.* **2016**, *606*, 1.
[211] D. D. L. Chung, *J. Mater. Sci.* **2002**, *37*, 1475.
[212] A. M. Zaitsev, *Optical Properties of Diamond*, Springer Berlin Heidelberg, Berlin, Heidelberg, **2001**.
[213] C. A. Klein, W. D. Straub, *Phys. Rev.* **1961**, *123*, 1581.
[214] J. He, M. Luo, L. Hu, Y. Zhou, S. Jiang, H. Song, R. Ye, J. Chen, L. Gao, J. Tang, *J. Alloys Compd.* **2014**, *596*, 73.
[215] J. Hiscock, A. T. Collins, *Diam. Relat. Mater.* **1999**, *8*, 1753.
[216] Y. Fang, Q. Dong, Y. Shao, Y. Yuan, J. Huang, *Nat. Photonics* **2015**, *9*, 679.
[217] F. Mendoza, V. Makarov, B. R. Weiner, G. Morell, *Appl. Phys. Lett.* **2015**, *107*, 201605.
[218] A. Balducci, M. Marinelli, E. Milani, M. E. Morgada, A. Tucciarone, G. Verona-Rinati, M. Angelone, M. Pillon, *Appl. Phys. Lett.* **2005**, *86*, 193509.
[219] H. Wei, Y. Fang, P. Mulligan, W. Chuirazzi, H.-H. Fang, C. Wang, B. R. Ecker, Y. Gao, M. A. Loi, L. Cao, J. Huang, *Nat. Photonics* **2016**, *10*, 333.
[220] G. Konstantatos, J. Clifford, L. Levina, E. H. Sargent, *Nat. Photonics* **2007**, *1*, 531.
[221] S. Yakunin, D. N. Dirin, L. Protesescu, M. Sytnyk, S. Tollabimazraehno, M. Humer, F. Hackl, T. Fromherz, M. I. Bodnarchuk, M. V. Kovalenko, W. Heiss, *ACS Nano* **2014**, *8*, 12883.
[222] Y. Lee, J. Kwon, E. Hwang, C.-H. Ra, W. J. Yoo, J.-H. Ahn, J. H. Park, J. H. Cho, *Adv. Mater.* **2015**, *27*, 41.
[223] F. Schirru, C. Nociforo, M. Kiš, M. Ciobanu, J. Frühauf, A. Kratz, N. Kurz, B. Szczepanczyk, M. Träger, R. Visinka, *J. Phys. D. Appl. Phys.* **2016**, *49*, 215105.
[224] M. Pillon, M. Angelone, P. Batistoni, S. Loreti, A. Milocco, *Fusion Eng. Des.* **2016**, *106*, 93.
[225] M. Osipenko, M. Ripani, G. Ricco, B. Caiffi, F. Pompili, M. Pillon, G. Verona-Rinati, R. Cardarelli, *Nucl. Instruments Methods Phys. Res. Sect. A Accel. Spectrometers, Detect. Assoc. Equip.* **2016**, *817*, 19.
[226] T. Shimaoka, J. H. Kaneko, M. Tsubota, H. Shimmyo, H. Watanabe, A. Chayahara, H. Umezawa, S. Shikata, *EPL (Europhysics Lett.)* **2016**, *113*, 62001.
[227] C. Gomà, M. Marinelli, S. Safai, G. Verona-Rinati, J. Würfel, *Z. Med. Phys.* **2016**, *26*, 88.
[228] J. M. Lárraga-Gutiérrez, P. Ballesteros-Zebadúa, M. Rodríguez-Ponce, O. A. García-Garduño, O. O. G. de la Cruz, *Phys. Med. Biol.* **2015**, *60*, 905.
[229] L. Brualla-González, F. Gómez, M. Pombar, J. Pardo-Montero, *Phys. Med. Biol.* **2016**, *61*, N11.
[230] A. Chalkley, G. Heyes, *Br. J. Radiol.* **2014**, *87*, 20130768.
[231] Y. Akino, A. Gautam, L. Coutinho, J. Würfel, I. J. Das, *J. Radiat. Res.* **2015**, *56*, 912.
[232] H. Chen, H. Liu, Z. Zhang, K. Hu, X. Fang, *Adv. Mater.* **2016**, *28*, 403.
[233] X. Gong, M. Tong, Y. Xia, W. Cai, J. S. Moon, Y. Cao, G. Yu, C.-L. Shieh, B. Nilsson, A. J. Heeger, *Science* **2009**, *325*, 1665.
[234] X. Li, M. Rui, J. Song, Z. Shen, H. Zeng, *Adv. Funct. Mater.* **2015**, *25*, 4929.

© 2016 WILEY-VCH Verlag GmbH & Co. KGaA, Weinheim